# Bio-Inspired Homometallic and Heterometallic Clusters Relevant to the Oxygen-Evolving Complex of Photosystem II

Thesis by
Kurtis Mickel Carsch

In Partial Fulfillment of the Requirements
for the Degree of Master of Science


Division of Chemistry and Chemical Engineering

CALIFORNIA INSTITUTE OF TECHNOLOGY

Pasadena, California

2016

(Defended on 3 June 2016)

*“We make molecules here, and lots of them.”*

## ACKNOWLEDGEMENTS

I have had an incredible experience pursuing inorganic chemistry during my past six years I have spent at the University of North Texas (UNT) and at the California Institute of Technology (Caltech). Although the list of people to thank is too extensive to cover exhaustively, I would like to thank several people explicitly. First, I am indebted to Prof. Thomas Cundari (UNT) for allowing me to pursue computational chemistry directly under his tutelage. His scientific insight, mentorship, and general guidance have provided me with invaluable skills that have helped me design my early scientific career. I am similarly thankful for working within the Center for Catalytic Hydrocarbon Functionalization (CCHF) in which I have had the opportunity to provide computational insight into experiments conducted by Prof. T. Brent Gunnoe (U. Virginia) and Dr. Jiajun Mei. Furthermore, I would like to thank several of my professors at UNT who helped me with my decision to attend Caltech, including Prof. Duncan Weather, Prof. James Duban, and Prof. Martin Schwartz.

I would next like to acknowledge Prof. William (Bill) Goddard who has allowed me to conduct research in the catalysis subdivision since my stay at Caltech through the Summer Undergraduate Research Fellowship (SURF) program. Through working with Bill, I have valued his excellent mentorship and his willingness to allow me to pursue joint synthetic-computational projects, to propose and pursue my own research ideas, to present my research findings at several conferences, and to co-teach his annual quantum mechanics course (Ch120a). In addition, I would like to thank other members of the Goddard group: Dr. Robert (Smith) Nielsen, Dr. Ross Fu, Dr. Yanchoi Lam, Dr. Mujeng Cheng, and Prof. Jose Mendoza-Cortes.

During my research with Prof. Goddard, I was able to pursue my research interests in experimental inorganic and organometallic chemistry with Prof. Theodor (Theo) Agapie. Theo

provided excellent scientific discussion in the context of one-on-one research meetings, group meetings, and our weekly literature discussions for Ch81. I also would like to thank Dr. Graham de Ruiter for mentoring me and providing a rigorous training. I similarly extend my gratitude to all other members of the cluster subgroup during my experience: Charlie Arnett, Chris Reed, Heui Beom (HB) Lee, Dr. Zhiji Han, Dr. Kyle Horak and Dr. Davide Lionetti. I would similarly like to thank Mona Shahgholi, Dave VanderVelde, Mike Takase, and Larry Henling.

Lastly, I would like to acknowledge several people outside of lab who have helped me maintain my sanity over the previous few years, especially when my attitude was less-than-pleasant. My parents and family have been incredibly supportive, especially with my decision to attend Caltech, my decision to pursue chemistry, and with my decision to attend graduate school. I would like to thank the Chemistry Club executive board for their patience with me over this previous year, especially during consecutive weeks of my absence for graduate school visitations. I would further like to thank Saaket Agrawal, Raj Mirpuri, Albert Yang, David Lichko, Jerry Feng, Erik Haastrup, and Eva Scheller, either for helpful discussions or for allowing me to vent when necessary.

## PREFACE

The objectives of this thesis are manifold: (i) to fulfill the institute requirement for my joint BS/MS appointment in chemistry, (ii) to summarize my research progress at Caltech, (iii) to provide an outline for any chemist who wishes to further these endeavors, and (iv) to reflect over several different projects prior to the start of my Ph.D. studies. As several of my research endeavors have been previously published or are currently being written up for submission, I will abstain from discussions of these projects and will instead use this opportunity to present unpublished results. The research presented in this thesis will cover partial research results from my junior and senior years in the Agapie group at Caltech.

## RESPECTIVE CONTRIBUTIONS

This thesis is the result of several collaborative efforts. To the best of my knowledge, all non-referenced results are from my own endeavors. In **Chapter 2**, the synthesis and characterization of the tetra-nuclear heterometallic clusters was performed in collaboration with Dr. Graham de Ruiter.

## ABSTRACT

The following two chapters delineate several endeavors to isolate and characterize functional models of the oxygen-evolving complex (OEC) of photosystem II. Understanding the electronic structure and the precise mechanism of the O–O bond coupling step in the Kok cycle affords insight into this fundamental process and will guide the design of new earth-abundant catalysts to perform water oxidation under environmentally benign conditions. Nature performs this transformation by a heterometallic $CaMn_4O_5$ cluster arranged a tetra-metallic cubane bridged to a dangling manganese ion. Although a myriad of synthetic inorganic complexes are capable of water oxidation, these structures significantly underperform the OEC in terms of turnover number and turnover frequency. The objectives of this thesis are (i) to construct multimetallic clusters using the OEC as inspiration, (ii) to explore the reactivity of these clusters with oxygen-atom transfer reagents, and (iii) to identify intermediates responsible for oxygen-based chemistry.

In **Chapter 1**, a series of pseudo-$C_3$ symmetric tetra-manganese clusters with an interstitial $\mu_4$-oxygen was synthesized and characterized in several oxidation states. These clusters (of the general formula $[LMn_3(PhPz)_3OMn][OTf]_x$; x = 1, 2) are supported by pyridine and alkoxide donors connected by a 1,3,5-triarylbenzene spacer. A $\mu_4$-oxygen coordinates all four metal centers that are also bridged by phenyl pyrazolate (PhPz) ligands. This arrangement furnishes a vacant coordination site at a site-differentiated (apical) metal center. Exposure of these clusters to oxygen-atom transfer reagents (OAT's) results in the intramolecular oxygenation of a $C(sp^2)$–H bond of the bridging phenyl pyrazolate. Similarly, using 2,6-difluorophenyl pyrazolate ($F_2ArPz$) as the bridging ligand results in the oxygenation of the C–F bond with concurrent F-atom transfer. This reactivity represents an unprecedented C–F activation for molecular

manganese complexes. All hydroxylated and fluorinated clusters were independently prepared to confirm the observed reactivity upon exposure to OAT's. The pathways responsible for arene activation – postulated to proceed through an iodosobenzene adduct and subsequent formation of a transient high-valent manganese-oxo motif – are discussed.

In **Chapter 2**, a series of pseudo-$C_3$ symmetric heterometallic $Fe_3Mn$ clusters of the general formula $[LMn_3(PhPz)_3OMn][OTf]_x$ (x = 1–3) was synthesized and characterized. Similar to their homometallic tetra-manganese and tetra-iron analogs (**Chapter 1**), these clusters contain four metal centers with a central bridging interstitial $\mu_4$-oxygen atom and bridging phenyl pyrazolate ligands. These clusters are further supported by pyridine and alkoxide donors, linked through a 1,3,5-triarylbenzene spacer. All complexes were characterized by zero-field $^{57}$Fe Mössbauer spectroscopy to confirm the presence of a manganese metal center in the apical position, illustrating that these clusters are stable with respect to metal scrambling and/or decomposition. Treatment of these clusters with 1-(*tert*-butylsulfonyl)-2-iodosylbenzene (sPhIO) resulted in the oxygenation of the $C(sp^2)$–H bond of the proximal phenyl pyrazolate motif to afford $[LMn_3(PhPz)_2(OArPz)OMn][OTf]_x$ (x = 2, 3). During these studies, an unusual iodosobenzene adduct of $[Fe^{III}_3Mn^{II}]^{3+}$ was isolated prior to C–H activation. This adduct has been characterized both by single-crystal XRD and $^1$H-NMR spectroscopy. In order to gain insight into the C–H bond oxygenation by this iodosobenzene adduct, preliminary computational studies are presented to discuss the viability of a transient manganese-oxo species responsible for arene hydroxylation.

## TABLE OF CONTENTS

## LIST OF FIGURES

## LIST OF SCHEMES

## LIST OF TABLES

## LIST OF ABBREVIATIONS

| | |
|---|---|
| AcOH | Acetic Acid |
| $CoCp_2$ | Cobaltocene |
| $CoCp_2$* | Decamethylcobaltocene |
| CV | Cyclic Voltammetry *or* Cyclic Voltammogram |
| DFT | Density Functional Theory |
| DMF | N,N-Dimethylformamide |
| $F_2$ArPzH | 3-(2,6-difluorophenyl)-1H-pyrazole |
| $Mn(HMDS)_2$ | Manganese bis(bis(trimethylsilyl))amide |
| NaHMDS | Sodium bis(trimethylsilyl)amide |
| NaPhPz | Sodium 3-Phenylpyrazolate |
| $NaF_2$PhPz | Sodium 3-(2,6-difluorophenyl)pyrazolate |
| NaOArPzH | 2-(1H-pyrazol-3-yl)phenolate |
| NaOFArPzH | 2-(1H-pyrazol-3-yl)-3-fluorophenolate |
| NMR | Nuclear Magnetic Resonance |
| OAc | Acetate |
| OAT's | Oxygen-atom Transfer Reagents |
| OEC | Oxygen-Evolving Complex |
| OTf | Trifluoromethylsulfonate |
| PhIO | Iodosobenzene |
| PhPzH | 3-Phenyl-1*H*-Pyrazole |
| PSII | Photosystem II |
| sPhIO | 1-(*tert*-butylsulfonyl)-2-iodosylbenzene |
| TBA | Tetrabutylammonium |
| $^t$BuLi | Tert-butyl lithium |
| THF | Tetrahydrofuran |
| UV-vis | Ultraviolet-visible |
| VT | Variable Temperature |
| XRD | X-Ray Diffraction |

## Chapter 1. Intramolecular C–H and C–F Activation by Homometallic Tetra-Manganese Clusters in Pursuit of Multimetallic Mn(IV)=O Motifs

**Abstract**. Homometallic site-differentiated tetra-manganese clusters of the general formula $[LMn_3(PhPz)_3OMn][OTf]_x$ (x = 2 (**1.2**), 1 (**1.3**); PhPz = 3-phenylpyrazolate) were synthesized and characterized. These clusters consist of a tri-manganese core supported by a tri-nucleating ligand consisting of weak-field alkoxide and pyridine donors. The site-differentiated (apical) manganese ion is appended to the tri-manganese core by three phenyl pyrazolate bridging ligands and an interstitial $\mu_4$-oxygen atom. The presence of a site-differentiated apical manganese metal center provides an excellent entry to investigate the formation of $Mn^{IV}$-oxo motifs on a multimetallic scaffold, relevant for the O–O bond coupling mechanism in the oxygen-evolving complex of photosystem II. Interestingly, exposure of **1.2** and **1.3** to iodosobenzene results in the intramolecular arene hydroxylation to afford $[LMn_3(PhPz)_2(OArPz)OMn][OTf]_x$ (x = 2 (**1.5**), 1 (**1.6**)). This regioselective hydroxylation is consistent with and postulated to proceed through a putative $Mn^{IV}$-oxo motif. To mitigate the observed arene hydroxylation, the fluorinated analogs $[LMn_3(F_2ArPz)_3OMn][OTf]_x$ (x = 2 (**1.7**), 1 (**1.8**); $F_2ArPz$ = 3-(2,6-difluorophenyl)pyrazolate) were synthesized and characterized. Exposure of **1.7** and **1.8** to oxygen-atom transfer reagents resulted in unprecedented intramolecular arene C–F oxygenation to yield $[LMn_3(F_2ArPz)_2(OFArPz)OMn][OTf]_x$ (x = 2 (**1.12**), 1 (**1.10**)). This C–F activation is coupled with the transfer of a fluorine anion to provide terminal fluoride clusters, $[LMn_3(F_2ArPz)_3OMn(F)][OTf]_x$ (x = 2 (**1.13**), 1 (**1.11**)). This type of reactivity engendered by a putative manganese-oxo species is unprecedented. The identities of the products of C–H and C–F activations were confirmed by independent synthesis. With the propensity of the metal clusters to undergo intramolecular electron transfer, the various

mechanistic pathways (including $Mn^{IV}$-oxo vs. $Mn^{III}$-oxo vs. $Mn^{II}$-oxygenate adduct) are discussed.

**1.1 Introduction**. The four-electron, four-proton oxidation of water to dioxygen, catalyzed by the oxygen-evolving complex (OEC) of photosystem II (PSII), presents an attractive alternative energy source to traditional petrochemical fuels.[1,2] A variety of economic and environmental benefits include the elimination of carbon-based emissions, lower consumption of petrochemical resources, and introduction of a renewable energy source.[3,4] Nonetheless, current efforts to evolve oxygen from a synthetic scaffold are not nearly as efficient as the OEC in PSII.[5] This lack of understanding originates from difficulties in predicting and controlling how multiple metals in close proximity cooperate to perform multi-electron chemistry with substrates.[6] To improve our understanding of the OEC and increase catalytic performance of synthetic water-oxidation catalysts, detailed studies of the O–O bond-coupling mechanism, the process of catalytic turnover, and the dynamic electronic structure of the OEC are mandatory.

Recently, high-resolution (1.90 Å and 1.95 Å 'radiation-damage-free') crystal structures of the PSII dimer have revealed the structure of the OEC as a $CaMn_4O_5$ cluster in a "dangler-plus-cubane" motif, in which a Mn ion is bridged to the $CaMn_3O_4$ cubane core (Figure 1.1).[7,8]

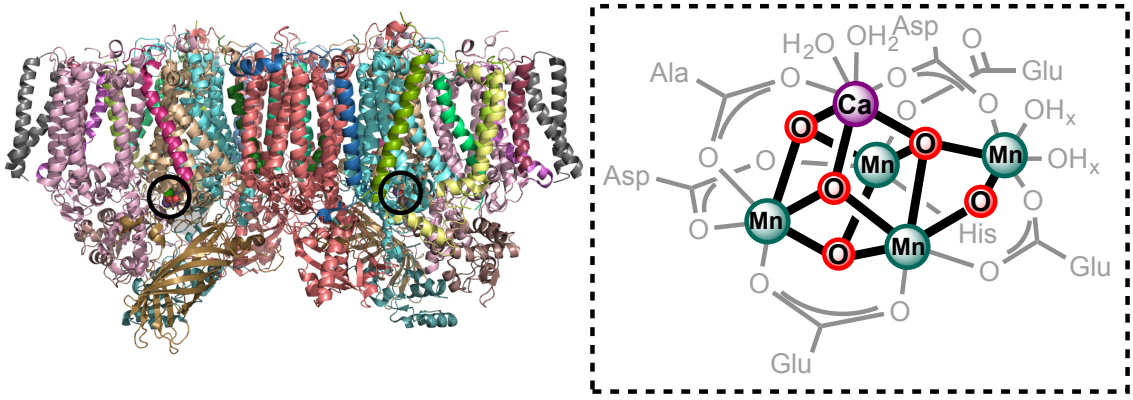


**Figure 1.1**. Photosystem II protein matrix with heterometallic cofactor responsible for water oxidation. The metallic cofactors are circled in the protein structure (left) with the structure of the oxygen-evolving complex displayed (right).

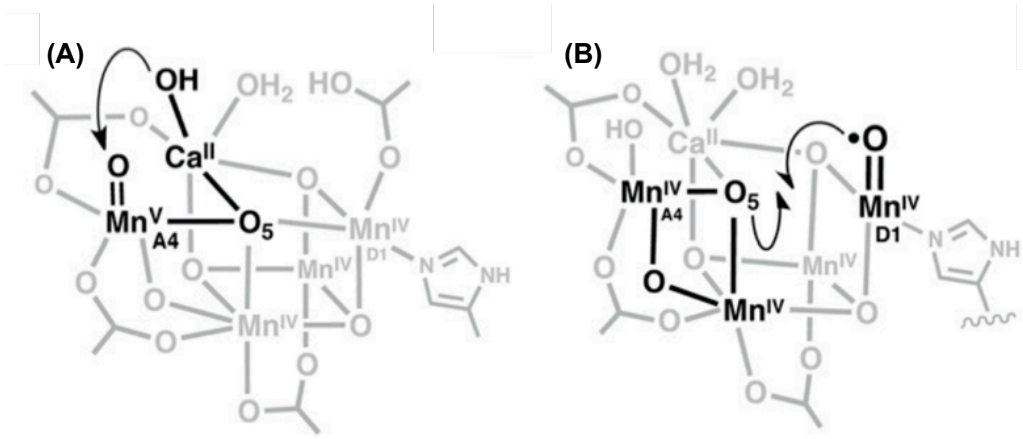


**Figure 1.2.** Proposed mechanisms for O–O bond coupling by the oxygen-evolving complex, proceeding by nucleophilic attack (A) or radical coupling (B).[9]

Density functional theory (DFT) and a variety of spectroscopy techniques suggest two distinct classes of O–O bond coupling mechanisms:[10] (i) nucleophilic attack from a Ca(II)-$OH_2$/Ca(II)-OH motif onto the terminal oxygen of the electrophilic Mn(IV)-O• or Mn(V)=O moiety,[11,12,9] or (ii) a radical coupling between the dangler-bridging μ-oxo radical and an oxyl radical.[13,14,15] The former route for oxygen evolution has been observed for a variety of Ru(III),[16] Mn(III),[17] and Fe(IV)[18] mono- and bi-metallic complexes whereas the latter has been proposed by DFT calculations for a tetranuclear Mn(III) system.[19]

To better understand the mechanism behind the formation of dioxygen and the proposed intermediates, the study of synthetic models incorporating Mn(IV)-oxo motifs is beneficial. For instance, Borovik and coworkers have reported a series of Mn(III)-, Mn(IV)-, and Mn(V)-oxo complexes in three-fold symmetry which activate weak external C–H bonds (Figure 1.3A).[9,20,21] The hydrogen-bonding feature of the secondary coordination sphere allows for stabilization of complexes containing both terminal oxo or hydroxo motifs.[22] Further studies have elucidated the electronic description of the Mn(V)-oxo motif as 0.45 α spins localized on the oxido unit, supporting a Mn(V)-oxo assignment in lieu of an alternative Mn(IV)-oxyl radical assignment.[23] Fout and coworkers have similarly modified the secondary coordination sphere of a three-folded

symmetric ligand to access a monometallic Mn(III)=O motif (Figure 1.3B).[24] The presence of the hydrogen-bonding network attenuates both the basicity and reactivity of the oxo unit.

Although precedence exists for monometallic Mn(IV)-oxo species, no synthetic terminal Mn(IV)-oxo species supported by a multimetallic scaffold has been reported. Notwithstanding, the synthesis and characterization of a polynuclear cluster containing a Mn(IV)-oxo moiety would provide valuable information with regard to the influence of distal metal centers on the reactivity of the terminal Mn(IV)-oxo; however, the synthetic challenges associated with constructing finite, multimetallic clusters have long obfuscated this endeavor. Toward this synthetic target, the initial synthesis of a multimetallic manganese cluster with a vacant coordination site for subsequent addition of an oxygen-atom transfer reagent has been envisioned (Scheme 1.1).

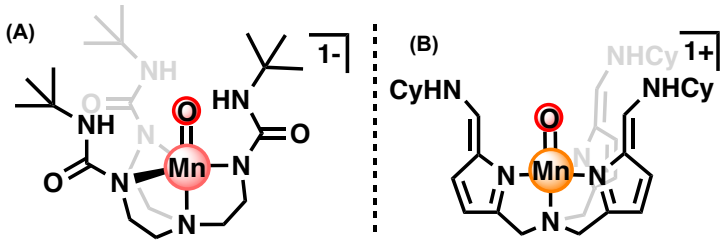


**Figure 1.3**. Examples of non-heme paramagnetic Mn=O motifs in a hydrogen-bonding network characterized by single-crystal XRD, by Borovik (A, $Mn^{IV}$)[21] and by Fout (B, $Mn^{III}$).[24]

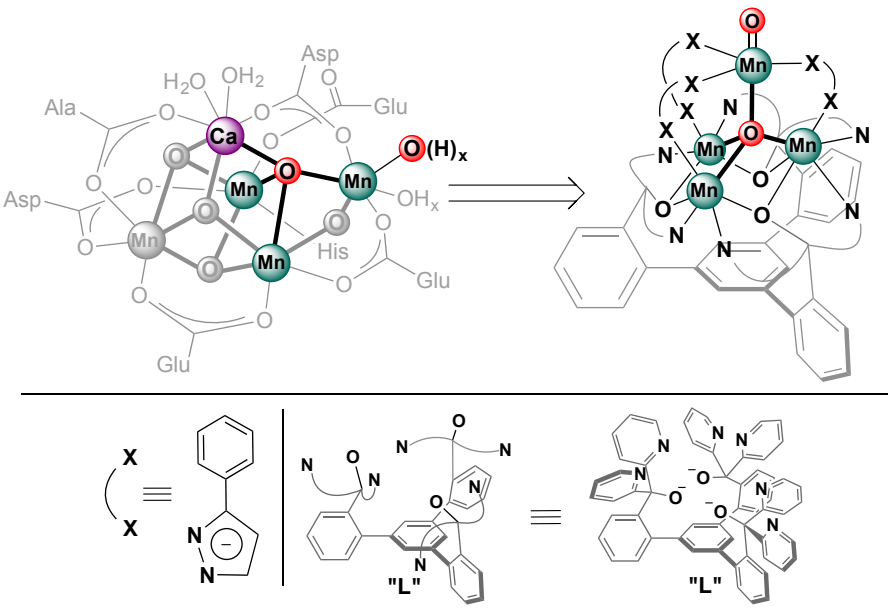


**Scheme 1.1**. Retrosynthetic analysis of the oxygen-evolving complex of photosystem II to allow for the design of homometallic tetramanganese clusters. Bridging pyrazolate motifs (lower left) motifs connect the apical metal to the trimetallic core in which the basal metals are supported by a trinucleating ligand ($\mathbf{L}^{3-}$; lower right).

Herein, we present the isolation and characterization of homometallic site-differentiated tetra-manganese clusters and their reactivity upon exposure to oxygen-atom transfer reagents (OAT's). These tetrametallic clusters encompass a trimetallic core consisting of three manganese ions bridged by weak field alkoxide and nitrogen donors. The site-differentiated (apical) manganese is appended to tri-manganese core through a $\mu_4$-oxygen atom and three phenyl pyrazolate ligands. These clusters are characterized by a variety of techniques including $^{1}H/^{19}F$-NMR, cyclic voltammetry (CV), electrospray ionization mass spectrometry (ESI-MS), and single-crystal X-ray diffraction (XRD). Electrochemical experiments demonstrated three oxidation/reduction waves (-1.67 V, -0.64 V, 0.15 V) in which the $[Mn^{III}Mn^{II}_3]^{1+}$ (-1.67 V vs. $Fc/Fc^{1+}$) and $[Mn^{III}_2Mn^{II}_2]^{2+}$ (-0.64 V vs. $Fc/Fc^{1+}$) clusters were successfully characterized by single-crystal XRD. Attempted formation of an apical Mn(IV)-oxo motif by treatment of these clusters with iodosobenzene (PhIO) resulted in an intramolecular $C(sp^2)$–H oxygenation of the

bridging phenyl pyrazole ligand. The observed reactivity is consistent with the formation of a putative $Mn^{IV}$-oxo and is independent of the oxidation state of the metal cluster. Although this reactivity has been observed for analogous multimetallic iron complexes, the oxygenation of a $C(sp^2)$–H bond by a multimetallic manganese complex is unprecedented. Furthermore, upon treatment of the fluorinated analogs with PhIO, intramolecular $C(sp^2)$–F oxygenation was observed. The activation of $C(sp^2)$–F bonds by manganese complexes is unprecedented and suggests the transient formation of a putative terminal manganese-oxo. Mechanistic pathways pertinent for both C–H and C–F oxygenation are discussed.

**1.2 Results and Discussion.** The targeted tetrametallic cluster $[LMn_3(PhPz)_3OMn][OTf]_2$ was synthesized using a similar strategy as outlined for the iron analog $[LFe_3(PhPz)_3OFe][OTf]_2$ (Figure 1.4).[25] Addition of excess methyl triflate (MeOTf; 3.0 equiv.) to the previously reported $LMn_3(OAc)_3$ afforded an off-white species consistent with the formation of $LMn_3(OAc)(OTf)_2$ (**1.1**) as judged by $^1H/^{19}F$-NMR spectroscopy, elemental analysis, and electrospray ionization mass spectrometry (ESI-MS; m/z = 539.5 ($[LMn_3(OAc)]^{2+}$) and m/z = 1228.0 ($[LMn_3(OAc)(OTf)]^{1+}$)). Subsequent ligand exchange with sodium 3-phenylpyrazolate (NaPhPz; 3.2 equiv.) and oxidation with iodosobenzene (PhIO; 1.1 equiv.) yielded a purple-brown powder with a $^1H$-NMR spectrum distinct from **1.1** (Figure S3). ESI-MS analysis shows a single peak at m/z = 1465.0, corresponding to the formation of $[LMn_3(PhPz)_3ONa][OTf]$. Salt metathesis with $Mn(OTf)_2(MeCN)_2$ (2.0 equiv.) yielded the homometallic tetra-manganese complex $[LMn_3(PhPz)_3OMn][OTf]_2$ (**1.2**) as a brown-purple powder in moderate yield (65 %). The $^1H$-NMR shows paramagnetic peaks shifted over 100 ppm (Figure S5), while the ESI-MS spectrum shows a peak at m/z = 760.3 $[LMn_3(PhPz)_3OMn]^{2+}$, consistent with the formation of **1.2**.

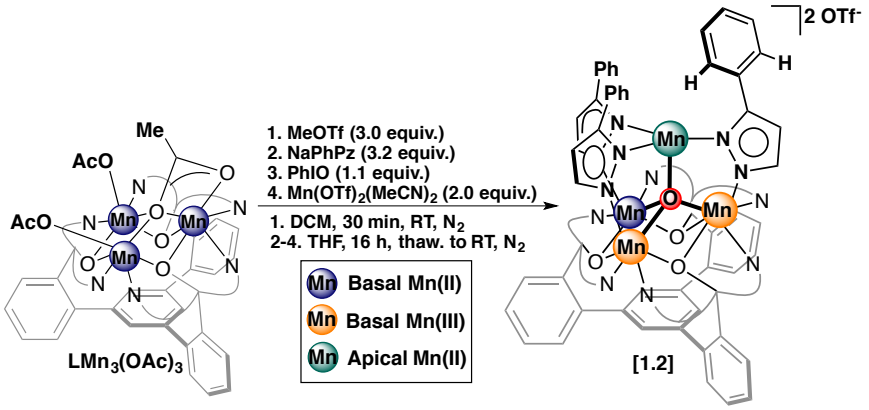


**Figure 1.4**. Step-wise synthesis of **1.2** from precursor $LMn_3(OAc)_3$.

Single crystals of **1.2**, suitable for X-ray diffraction (XRD), were grown by vapor diffusion of diethyl ether into a concentrated solution of **1.2** in acetonitrile. The solid-state structure of **1.2** contains three six-coordinate pseudo-octahedral manganese (Mn1-Mn3) centers in the basal position and an apical four-coordinate trigonal pyramidal Mn ion (Mn4), (Figure 1.5 and Figure 1.6A). The basal manganese ions are connected to the apical metal through a $\mu_4$-oxo bridge (O1). Based on the Mn1–O1 (1.945(7) Å), Mn2–O1 (2.009(7) Å), and Mn3–O1 (2.109(7) Å) bond distances, the oxidation state of the tri-manganese core is assigned as $Mn^{II}Mn^{III}_2$. The relatively long Mn3–N5 bond distance of 2.164(7) Å – compared to the Mn1–N1 (2.073(8) Å) and Mn2–N3 (2.039(9) Å) bond distances – corroborates this assignment (Table 1.1). The pyrazolate–manganese (Mn4) bond distances are all similar to each other, ranging from 2.099(9) Å to 2.128(9) Å. Similarly, Mn4 resides in a trigonal pyramid coordination environment. The apical manganese ion is assigned as Mn(II) based on charge balance, thus illustrating an overall $[Mn^{II}_2Mn^{III}_2]^{2+}$ motif.

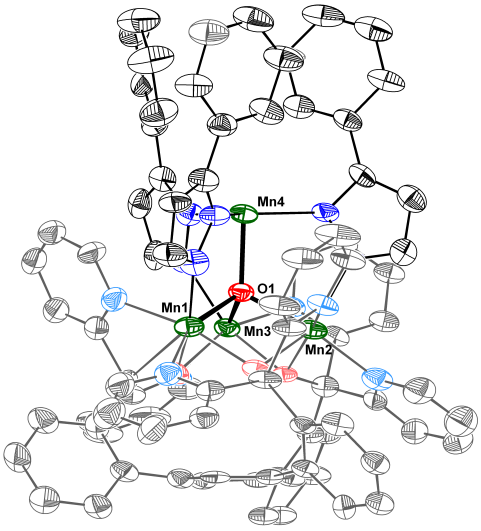


**Figure 1.5**. Complete molecular structures of complex **1.2**. Thermal ellipsoids are shown at the 50% probability level. Triflate counter anions, solvents, and hydrogen atoms are omitted for clarity.

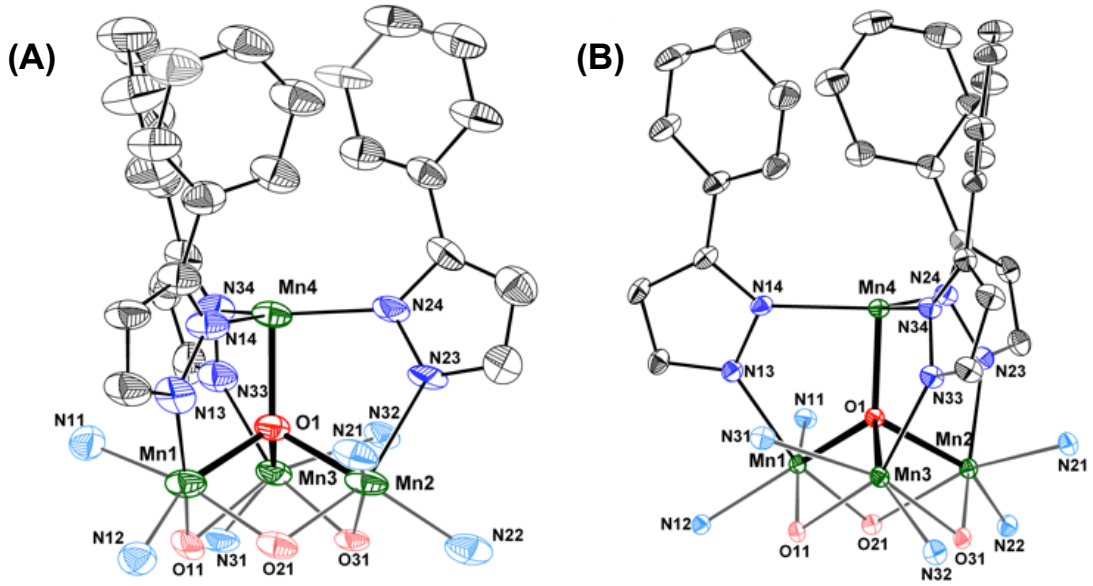


**Figure 1.6**. Truncated molecular structures of complexes **1.2** (A) and **1.3** (B) with partial labeling scheme. Thermal ellipsoids are shown at the 50% probability level. Triflate counter anions, solvents, and hydrogen atoms are omitted for clarity.

The electrochemical properties of **1.2** were investigated by cyclic voltammetry (CV). The CV for **1.2** is shown in Figure 1.7 (blue trace) and demonstrates two distinct quasi-reversible redox events at -1.67 V ($[Mn^{II}_4]^0/[Mn^{II}_3Mn^{III}]^{1+}$) and -0.64 V ($[Mn^{II}_3Mn^{III}]^{1+}/[Mn^{II}_2Mn^{III}_2]^{2+}$)

versus $Fc/Fc^{1+}$. An additional irreversible redox event corresponding to the $[Mn^{II}_2Mn^{III}_2]^{2+}/[Mn^{II}Mn^{III}_3]^{3+}$ couple was found at a more positive potential (0.15 V). The deviation from ideality may be consequent of large structural distortions upon changing the electron count between different oxidation states. This result is due to a Jahn Teller-like distortion upon oxidation of Mn(II) to Mn(III) in a pseudo-octahedral coordination environment. The population of the $d_{z2}$ σ* orbital results in bond elongation along the z-axis. The range of accessible oxidation states is similar to the analogous and iso-structural complex $[LFe(PhPz)_3OFe][OTf]_2$, in which three reversible redox events at -1.73 V ($[Fe^{II}_4]^0/[Fe^{II}_3Fe^{III}]^{1+}$), -0.73 V ($[Fe^{II}_3Fe^{III}]^{1+}/[Fe^{II}_2Fe^{III}_2]^{2+}$), and 0.02 V ($[Fe^{II}_2Fe^{III}_2]^{2+}/[Fe^{II}Fe^{III}_3]^{3+}$) were observed, Figure 1.7 (orange trace).

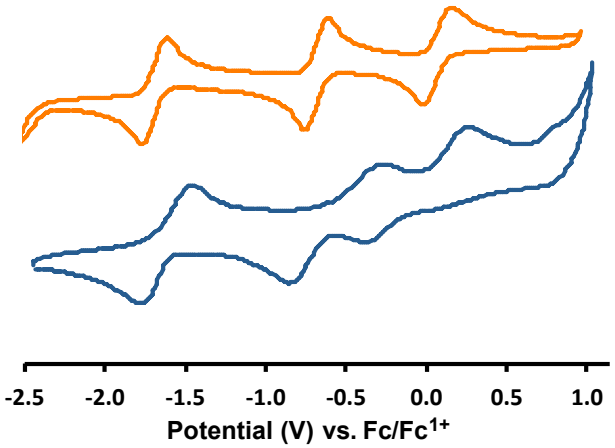


**Figure 1.7**. CVs of $[LMn_3(PhPz)_3OMn][OTf]_2$ (**1.2**, blue) and $[LFe_3(PhPz)_3OFe][OTf]_2$ (orange).[25] CV's were recorded at 100 mV $s^{-1}$ in dichloromethane at a 2 mM concentration. Glassy carbon, Pt-wire, and Ag-wire were used as the working, counter, and reference electrodes respectively. $TBAPF_6$ (0.1 M) was used as the supporting electrolyte.

**Table 1.1.** Selected bond parameters for complexes **1.2**, **1.3**, **1.7**, and **1.8**.

| | Complex | | | |
|---|---|---|---|---|
| **Bond Distances (Å)** | **1.2** | **1.3** | **1.7** | **1.8** |
| Mn1–O1 | 2.007(6) | 2.116(1) | 1.902(4) | 2.128(3) |
| Mn2–O1 | 2.113(6) | 2.189(1) | 2.222(4) | 2.193(3) |
| Mn3–O1 | 1.939(8) | 1.817(1) | 1.904(4) | 1.802(3) |
| Mn4–O1 | 1.993(6) | 1.986(1) | 2.104(4) | 2.012(3) |
| Mn1–N11 | 2.183(8) | 2.346(1) | 2.029(4) | 2.350(4) |
| Mn1–N12 | 2.149(9) | 2.209(1) | 2.101(5) | 2.231(4) |
| Mn1–N13 | 2.04(1) | 2.255(1) | 2.218(5) | 2.251(4) |
| Mn2–N21 | 2.167(8) | 2.374(2) | 2.089(5) | 2.223(4) |
| Mn2–N22 | 2.279(8) | 2.234(2) | 2.318(5) | 2.393(4) |
| Mn2–N23 | 2.169(9) | 2.197(1) | 2.039(5) | 2.189(4) |
| Mn3–N31 | 2.128(9) | 2.073(1) | 2.187(5) | 2.072(3) |
| Mn3–N32 | 2.230(9) | 2.377(1) | 2.332(5) | 2.328(4) |
| Mn3–N33 | 2.072(8) | 2.100(2) | 2.173(5) | 2.097(3) |
| Mn4–N14 | 2.100(8) | 2.120(1) | 2.203(5) | 2.142(4) |
| Mn4–N24 | 2.101(9) | 2.109(1) | 2.192(5) | 2.132(4) |
| Mn4–N34 | 2.128(9) | 2.132(2) | 2.152(5) | 2.150(3) |
| N13–N14 | 1.38(1) | 1.379(2) | 1.369(7) | 1.368(5) |
| N23–N24 | 1.38(1) | 1.378(2) | 1.358(7) | 1.372(6) |
| N33–N34 | 1.37(1) | 1.378(2) | 1.361(7) | 1.378(5) |
| **Bond Angles (°)** | | | | |
| N14–Mn4–N24 | 120.0(3) | 118.18(6) | 116.0(2) | 111.9(1) |
| N24–Mn4–N34 | 120.9(3) | 120.49(6) | 115.3(2) | 123.3(1) |
| N34–Mn4–N14 | 119.1(3) | 120.64(6) | 125.9(2) | 124.7(1) |
| **Torsion Angles (°)** | | | | |
| Mn1–N13–N14–Mn4 | -1.9(9) | 3.5(2) | -3.8(6) | -1.8(4) |
| Mn2–N23–N24–Mn4 | -3.1(9) | -5.2(2) | -10.7(6) | -20.8(4) |
| Mn3–N33–N34–Mn4 | 0(1) | 2.7(2) | -23.7(5) | 0.7(4) |
| **Centroid Distances (Å)** | | | | |
| Mn1\|Mn2\|Mn3–N14\|N24\|N34 | 2.900 | 2.925 | 2.799 | 2.946 |
| Mn1\|Mn2\|Mn3–O11\|O21\|O31 | 1.123 | 1.127 | 1.161 | 1.113 |
| Mn1\|Mn2\|Mn3–O1 | 0.910 | 0.963 | 0.922 | 0.958 |
| N14\|N24\|N34–O1 | 4.021 | 4.148 | 3.956 | 4.056 |

With the electrochemical properties of **1.2** established, the chemical oxidation and reduction of **1.2** were explored, (Figure 1.8). Addition of cobaltocene ($CoCp_2$; 1.1 equiv.) to a solution of **1.2** in $CH_2Cl_2$ resulted in a color change from brown-purple to brown-red. The $^1$H-NMR spectrum indicated a marked change, indicative of the formation of a new paramagnetic species **1.3**, (Figure S6). XRD of single crystals grown from vapor diffusion of diethyl ether into the

crude mixture in $CH_2Cl_2$ reveals **1.3** as $[LMn_3(PhPz)_3OMn][OTf]$. The unit cell consists of one outer-sphere triflate and a $\mu_4$-oxo bridged to three six-coordinate manganese centers (Mn1-Mn3) and one four-coordinate manganese (Mn4) metal center (Figure 1.6B). Compared to **1.2**, two of the $Mn_{core}$–O1 ($Mn_{core}$ is the centroid defined by Mn1–Mn3) bond distances are relatively long (2.007(6) Å, Mn1–O1; 2.116(1) Å, Mn2–O1; 1.817(1) Å, Mn3–O1), supporting a $Mn^{III}Mn^{II}_2$ tri-manganese core.

Interestingly, the Mn4–O1 bond length is identical between **1.2** (1.990(6) Å) and **1.3** (1.991(4) Å); however, the distance between O1 and the centroid defined by Mn1–Mn3 plane is significantly shorter for **1.3** (0.913 Å) compared to **1.2** (0.958 Å). The shortening of the $Mn_{core}$–O1 bond distance is attributed to O1 stabilizing the increased Lewis acidity in $Mn_{core}$ for **1.2** ($Mn^{II}Mn^{III}_2$) compared to the more electron-rich core in **1.3** ($Mn^{II}_2Mn^{III}$). Although further reduction of **1.3** is electrochemically feasible, addition of two equivalents of decamethylcobaltocene ($CoCp_2$*; 2.1 equiv.) to **1.2** affords a yellow-orange powder, insoluble in hydrocarbon solvents, aromatic solvents, ethereal solvents, and highly polar solvents. Nonetheless, addition of two equivalents of silver triflate (AgOTf) re-furnishes **1.2**, suggesting the formation of $LMn_3(PhPz)_3OMn$ (**1.4**) as the insoluble species, albeit in mediocre yield (41%). Attempts to isolate $[LMn_3(PhPz)_3OMn][OTf]_3$ by chemical oxidation of **1.2** have resulted in intractable mixtures (Appendix A.1).

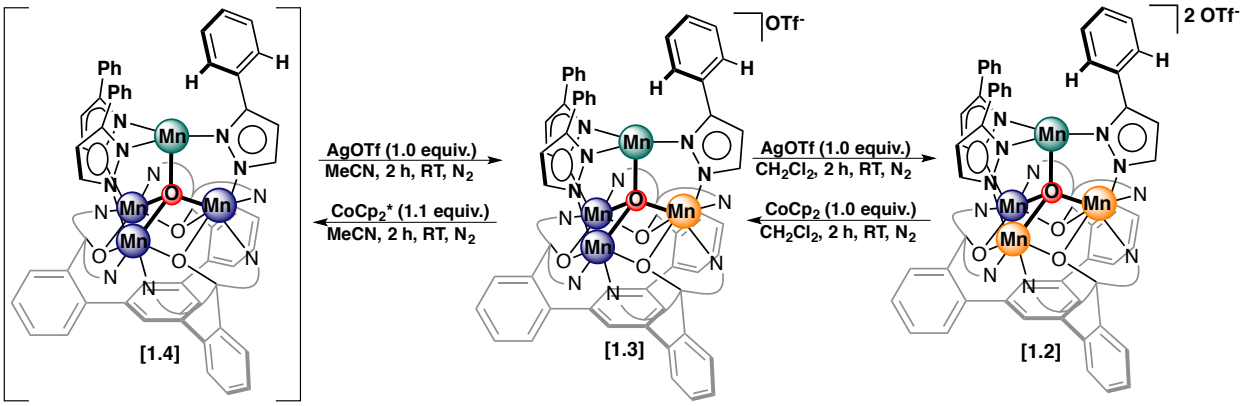


**Figure 1.8.** Synthesis of complexes **1.3** and **1.4**.

High-valent terminal manganese-oxo complexes of **1.2** and **1.3** were targeted to study the electronic structure and underlying reactivity of such species. Addition of iodosobenzene (PhIO; 1.1 equiv.) to **1.2** in $CH_2Cl_2$ affords an off-black species with a highly complicated $^1$H-NMR spectrum, consistent with the formation of a cluster of lower molecular symmetry. ESI-MS analysis of the crude reaction mixture shows a single peak corresponding $[LMn_3(PhPz)_2(OArPz)OMn]^{2+}$ (m/z = 768.5). Analogous studies on iron-based systems resulted in the C–H oxygenation of the surrounding ligand scaffold.[26,27,28,29] By analogy, we envision a similar mechanism operating akin to that reported for iron-based system, resulting in the formation of the complex $[LMn_3(PhPz)_2(OArPz)OMn][OTf]_2$ (**1.5**). Unfortunately, despite repeated crystallization attempts, X-ray quality crystals of **1.5** could not be isolated. To verify arene hydroxylation, **1.5** was synthesized independently. Addition of sodium 2-(pyrazol-3-yl)phenolate (NaOArPzH; 1.1 equiv.) to **1.2**, followed by oxidation with AgOTf (1.0 equiv.) resulted in the formation of a new species with $^1$H-NMR and ESI-MS spectra identical to that of **1.5** (Figure 1.9 and Figure S7).

Addition of PhIO (1.1 equiv.) to **1.3** in $CH_2Cl_2$ similarly afforded a brown-black powder. ESI-MS analysis of an aliquot from the reaction shows a single peak assignable to (m/z =

1535.0), corresponding to $[LMn_3(PhPz)_2(OArPz)OMn][OTf]$ (**1.6**). Similar to **1.5**, complex **1.6** was independently synthesized from addition of NaOArPzH (1.1 equiv.) to **1.2** (Figure S8).

To mitigate the observed arene $C(sp^2)$–H oxygenation, 2,6-difluorophenyl pyrazolate ($NaF_2Pz$) was selected due to the higher $C(sp^2)$–F bond dissociation free energy ($BDE_{C(sp2)–F}$ = 116 kcal $mol^{-1}$, $BDE_{C(sp2)–H}$ = 103 kcal $mol^{-1}$), potentially enabling the characterization of a transient terminal Mn(IV)-oxo intermediate. Subsequently, clusters of the general formula $[LMn_3(F_2ArPz)OMn][OTf]_x$ were targeted using an analogous synthetic strategy to **1.2** (Figure 1.10). Addition of $NaF_2PhPz$ (3.2 equiv.) and PhIO (1.1 equiv) to **1.1**. afforded a violet-brown species with a single ESI-MS feature (m/z = 1596.1), consistent the formation of $[LMn_3(F_2ArPz)_3ONa][OTf]$ (Figure S9). Salt metathesis with excess $Mn(OTf)_2(MeCN)_2$ (2.0 equiv.) yielded a $^1$H-NMR spectrum resembling that of **1.2**, suggesting the formation of $[LMn_3(F_2ArPz)_3OMn][OTf]_2$ (**1.7**), (Figure S11).

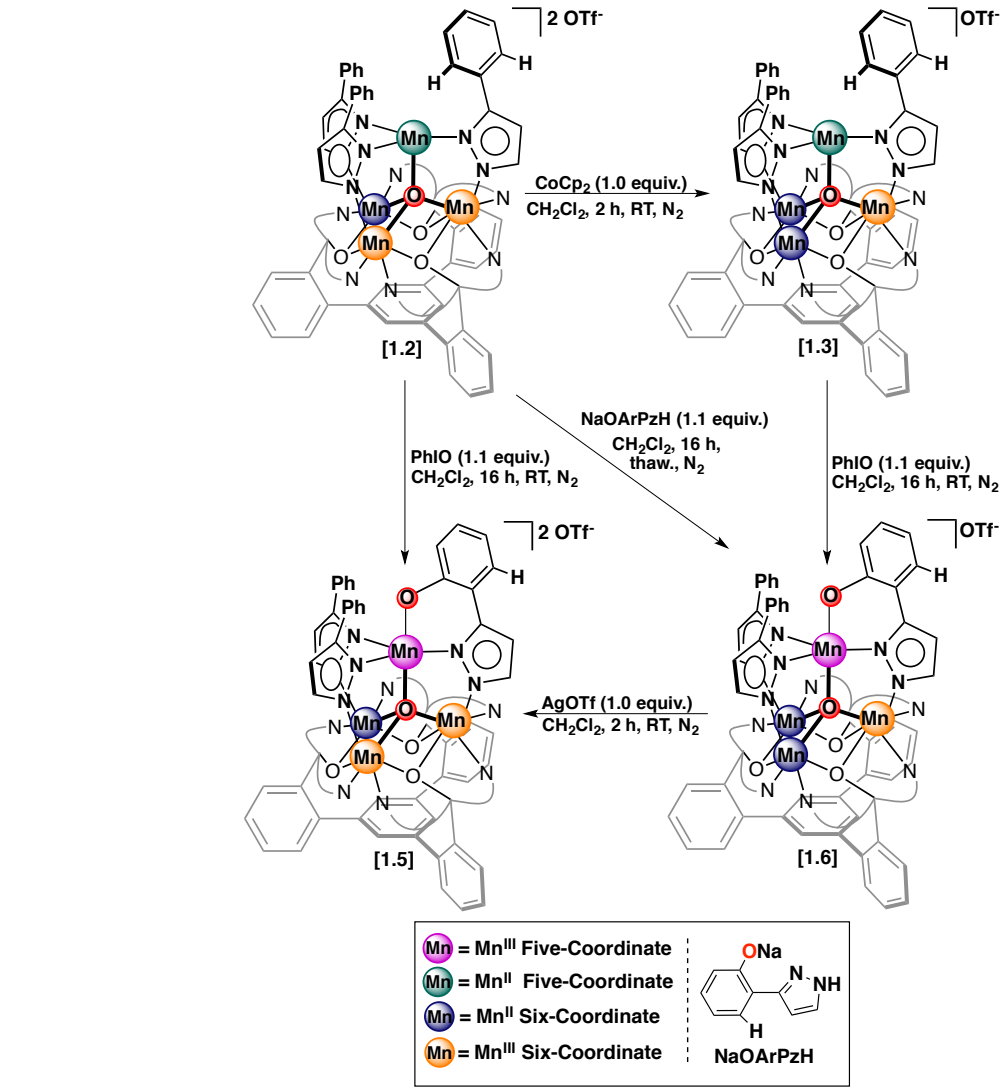


**Figure 1.9.** Synthesis of complexes **1.5** and **1.6**.

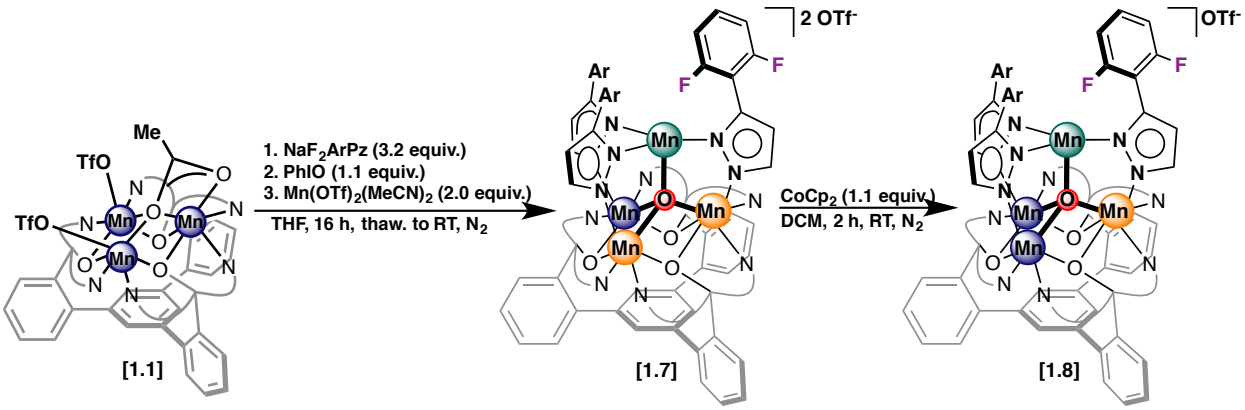


**Figure 1.10.** Synthesis of complexes **1.7** and **1.8**.

Large brown-violet crystals were obtained by vapor diffusion of diethyl ether into a concentrated solution of **1.7** in acetonitrile. The crystal structure of **1.7** (Figure 1.11A) is similar to that of **1.2**. The $Mn_{core}$–O1 bond distances of 1.902(4) Å, 2.222(4) Å, and 1.904(4) Å are similar to those of **1.2** (Table 1.1). Together with the presence of two outer sphere triflates, the Mn oxidation states are thus assigned as $[Mn^{III}_2Mn^{II}_2]^{2+}$. In contrast to **1.2**, the apical manganese (Mn4) in **1.7** is trigonal bipyramidal ($\tau = 0.80$), with the $\mu_4$-oxygen (O1) and the MeCN ligand in the axial position with respect to the N13|N23|N33 plane. The coordination of acetonitrile is due to a more electron deficient metal center (Mn4) resulting from the more electron-withdrawing nature of the 2,6-difluorophenyl pyrazolate bridging ligands. The coordination of acetonitrile and electron-deficient tri-manganese core result in Mn4–O1 bond distance elongation (2.098(4) Å vs. 1.993(6) Å in **1.2**) and contraction of the $Mn_{core}$–O1 bond distance (0.922 Å vs. 0.910 Å in **1.2**).

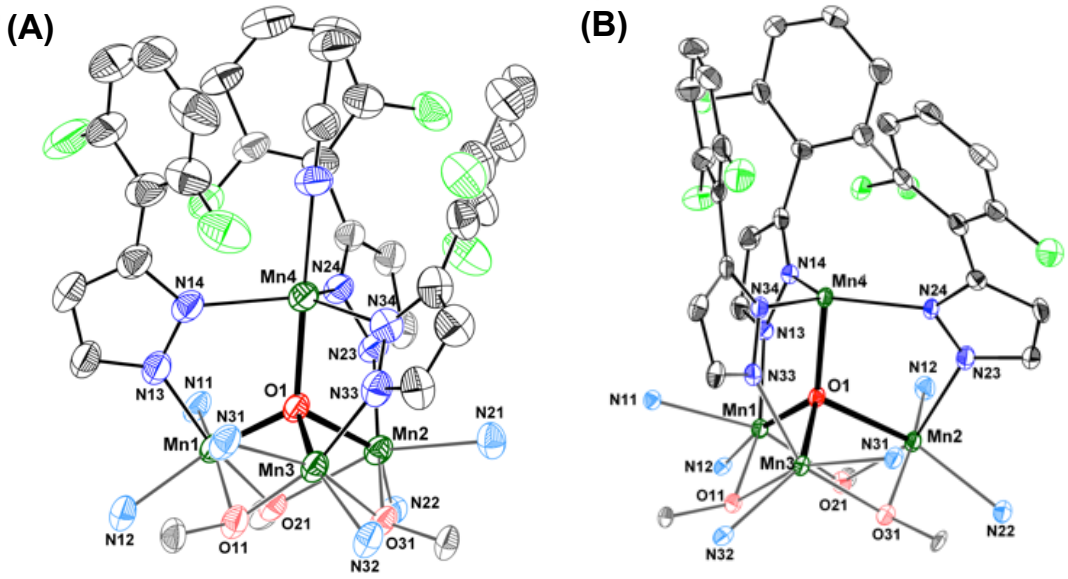


**Figure 1.11**. Truncated molecular structures of **1.7** (A) and **1.8** (B) with partial labeling scheme. Thermal ellipsoids are shown at the 50% probability level. Triflate counter anions, solvents, and hydrogen atoms are omitted for clarity.

Electrochemical studies of **1.7** revealed two quasi-reversible redox events at -1.67 V ($[Mn^{II}_4]^0/[Mn^{II}_3Mn^{III}]^{1+}$) and -0.66 V ($[Mn^{II}_3Mn^{III}]^{1+}/[Mn^{II}_2Mn^{III}_2]^{2+}$) versus $Fc/Fc^{1+}$ (Figure 1.12, green trace). An irreversible oxidation from $[Mn^{II}_2Mn^{III}_2]^{2+}$ to $[Mn^{II}Mn^{III}_3]^{3+}$ was observed at 0.30 V versus $Fc/Fc^{1+}$. Compared to **1.2**, the positive shift (> 50 mV) in all three redox events is in accord with the more electron-deficient nature of **1.7**.

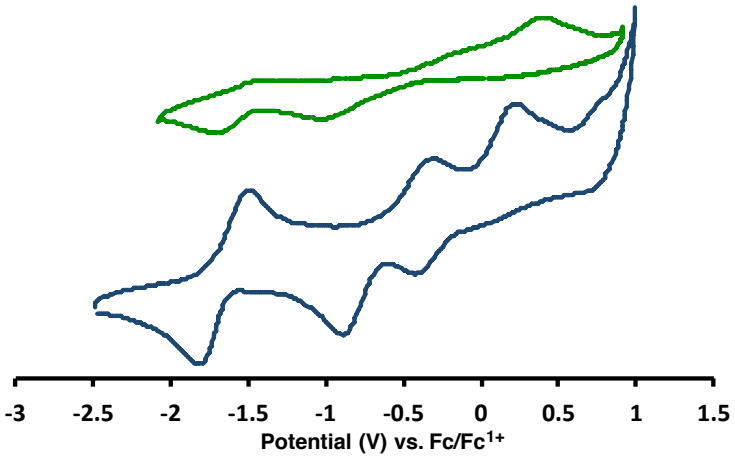


**Figure 12**. CVs of $[LMn_3(F_2ArPz)_3OMn][OTf]_2$ (**1.7**, green) and $[LMn_3(PhPz)_3OMn][OTf]_2$ (**1.2,** blue). The CV's were recorded at 100 mV $s^{-1}$ in $CH_2Cl_2$ at a concentration 2 mM. Glassy carbon, Pt-wire, and Ag-wire were used as working, counter, and reference electrode respectively. $TBAPF_6$ (0.1 M) was used as the supporting electrolyte.

The one-electron reduced complex $[LMn_3(F_2ArPz)_3OMn][OTf]$ was synthesized by addition of $CoCp_2$ (1.1 equiv.) to **1.7** in $CH_2Cl_2$, which resulted in a color change to red-violet. The $^1$H-NMR paramagnetic features of **1.8** are identical to those of **1.3** (Figure S13). Crystals suitable for XRD were obtained by vapor diffusion of diethyl ether into a solution of **1.8** in $CH_2Cl_2$, (Figure 11B). The $Mn_{core}$–O1 bond distances for **1.8** (Mn1–O1 (2.193(3) Å), Mn2–O1 (1.802(3) Å) and Mn3–O1 (2.128(3) Å)) closely resemble those of **1.3** (Table 1.1). Based on charge balance, the apical manganese is $Mn^{II}$ with an overall oxidation state of $[Mn^{II}_2Mn^{III}]$ for the tri-manganese core. The Mn4–O1 bond distance of 2.012(3) Å in **1.7** is nearly identical that of **1.3**. Similarly, the $Mn_{core}$–O1 bond length (0.958 Å) is near-identical to that for **1.3**.

With complexes **1.7** and **1.8** isolated, the formation of a terminal oxo motif was targeted. Treatment of **1.8** in $CH_2Cl_2$ with either $TBAIO_4$ (1.1 equiv.) or PhIO (1.1 equiv.) resulted in a mixture of two species. The ESI-MS spectrum showed equal intensity peaks, corresponding to $[LMn_3(F_2ArPz)_2(OFArPz)OMn]^{1+}$ (**1.10**; m/z = 1624.9) and $[LMn_3(F_2ArPz)_3OMnF]^{1+}$ (**1.11**; m/z = 1646.8). This data is consistent with arene hydroxylation with concomitant transfer of a fluoride anion followed by single-electron transfer to the phenoxide cluster; this transformation represents two one-electron oxidations for each product. Furthermore, the paramagnetic $^1$H-NMR spectrum is additionally consistent with the formation of multiple species. Unfortunately, **1.10** and **1.11** could not be separated by repeated crystallization, motivating the separate independent syntheses of **1.10** and **1.11**. Complex **1.8'** was successfully isolated upon addition of $AgBF_4$ (1.0 equiv.) to $LMn_3(F_2ArPz)_3OMn$ (**1.9**), resulting in a $^1$H-NMR spectrum identical to that of **1.8**, (Figure S14). The $^{19}$F-NMR confirms the presence of an outer-sphere tetrafluoroborate anion, (Figure S15). Addition of sodium 3-fluoro-2-(1*H*-pyrazol-5-yl)phenolate (NaOFArPzH; 1.1 equiv.) and $AgBF_4$ (1.0 equiv.) to **1.8'** resulted in $[LMn_3(F_2ArPz)_2(OFArPz)OMn][BF_4]$ (**1.10'**), (Figure 1.13).

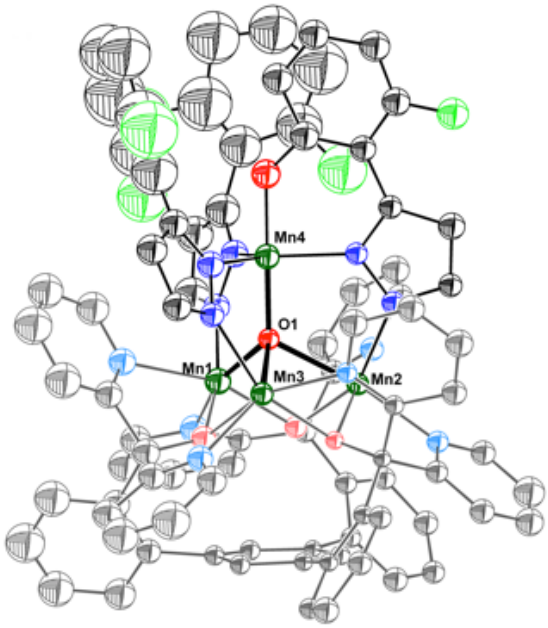


**Figure 1.13**. Crystal structure of **1.10'**. Tetrafluoroborate counter anion, solvents, and hydrogen atoms are omitted for clarity.

Two molecules of **1.10'** are present in the asymmetric unit. In contrast to the non-fluorinated analogs, different solid-state binding modes of the pyrazolate are observed, reflecting the electron-withdrawing nature of the fluorinated pyrazole ligand. In particular, electron-density assigned to a single flipped pyrazolate configuration is present. Complex **1.11** was synthesized by addition of $XeF_2$ (1.0 equiv.) to **1.8** in thawing MeCN. The $^1$H-NMR spectrum of both **1.10** and **1.11** are contained within that of the crude mixture (Figure S16).

Addition of PhIO (1.1 equiv.) to **1.7** in $CH_2Cl_2$ afforded a paramagnetic $^1$H-NMR spectrum with multiple species present. ESI-MS analysis shows two major peaks corresponding to $[LMn_3(F_2ArPz)_2(OFArPz)OMn]^{2+}$ (**1.12**; m/z = 812.7) and $[LMn_3(F_2ArPz)_3OMnF]^{2+}$ (**1.13**; m/z = 823.7). Both **1.12** and **1.13** were independently synthesized in a similar manner to **1.10** and **1.11**, (Figure S17)**.** The results of these independent preparations are summarized in Figure 1.14.

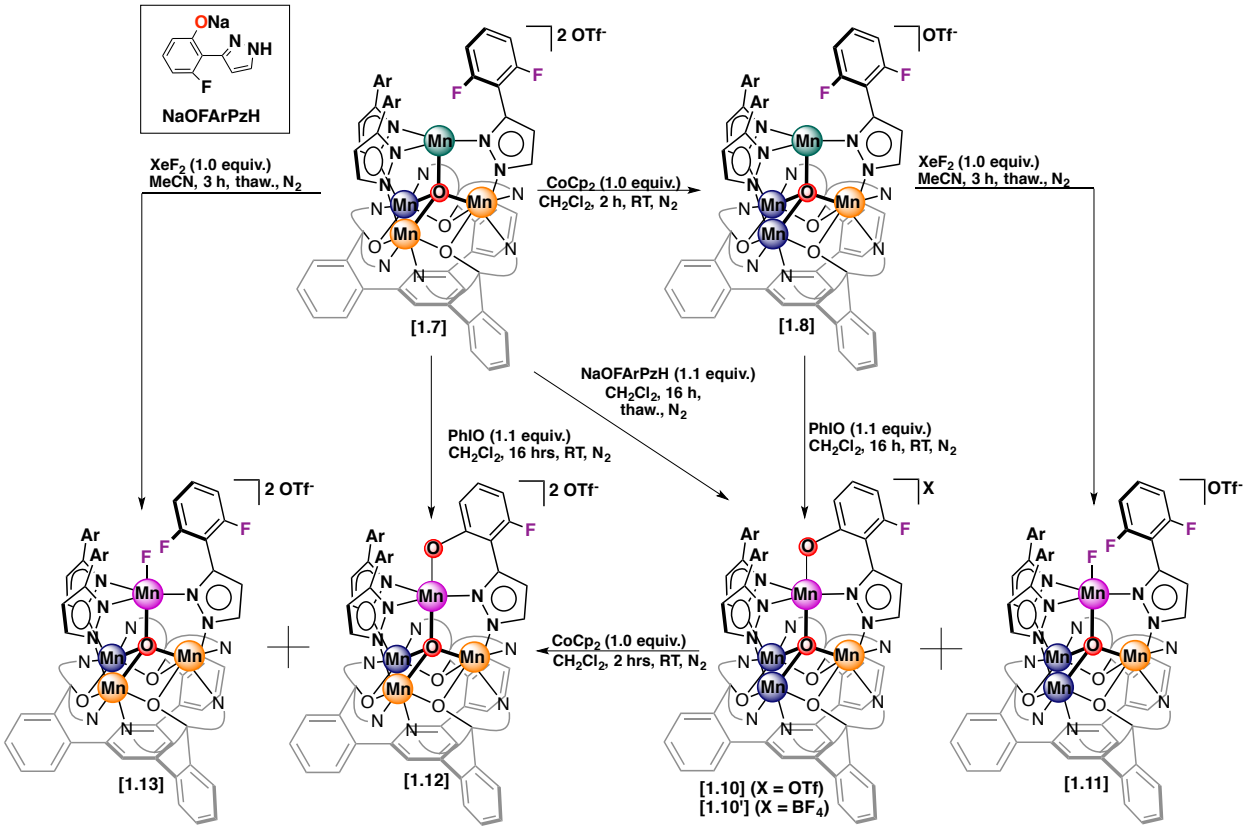


**Figure 1.14.** Synthesis of complexes **1.10'**, **1.11**, **1.12**, and **1.13**.

Assuming addition of oxidant furnishes a terminal high-valent manganese-oxo, we postulate the mechanism of C–F activation proceeds by radical arene activation, followed by fluoride transfer to unreacted starting material and single electron transfer to furnish a net one-electron oxidation in each cluster, (Figure 1.15). Although the electronic structure of the terminal manganese-oxo complex can be assigned as either $Mn^{IV}Mn^{III}_2Mn^{II}$ or $Mn^{III}_4$, preliminary DFT calculations indicate redox-localization in which the oxido stabilizes an adjacent $Mn^{IV}$ ion. The analogous mechanism is similarly proposed for C–F oxygenation in **1.8**.

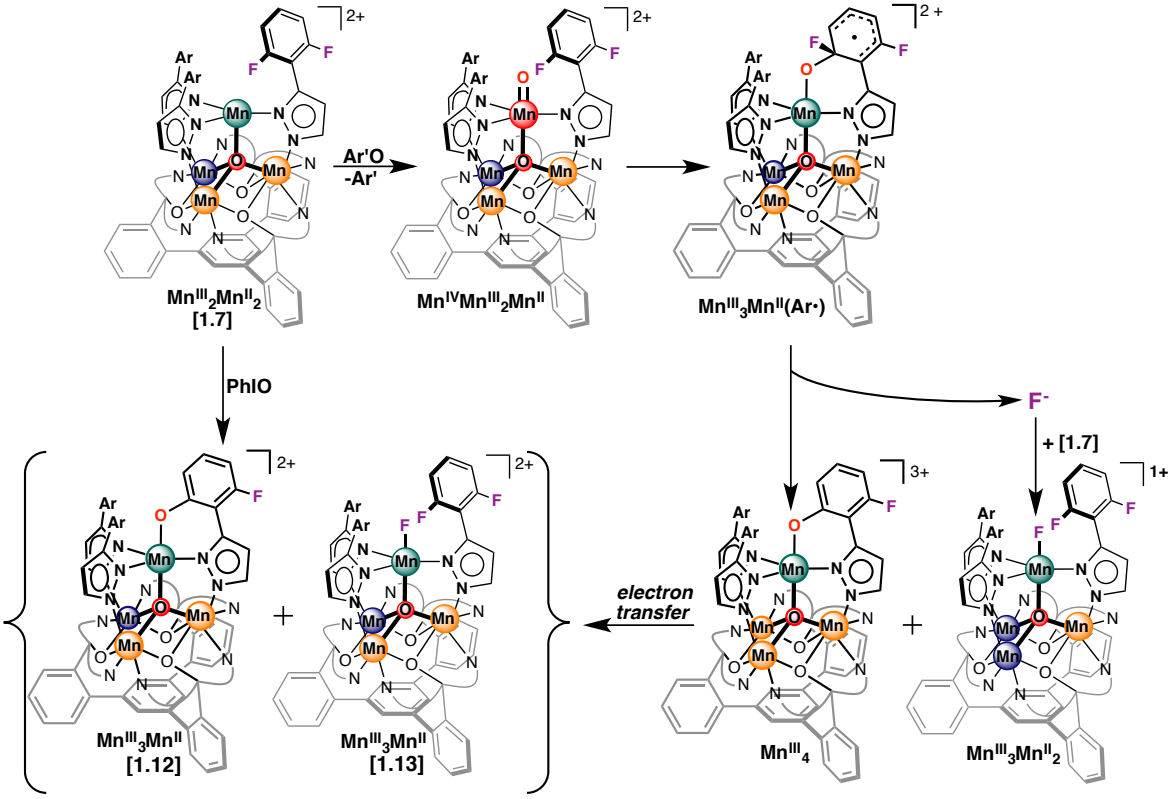


**Figure 1.15**. Proposed mechanism for synthesis of complexes **1.12** and **1.13** by putative $Mn^{IV}$-oxo motif.

For C–H oxygenation by treatment of **1.2** and **1.3** with PhIO, we propose four possible mechanisms: (i) concerted C–H activation through an iodosobenzene adduct, (ii) concerted C–H activation by a terminal manganese-oxo, (ii) H-atom abstraction from the proximal phenyl ring with subsequent radical rebound, and (iii) radical arene activation, (Figure 1.16). The overall reaction proceeds with loss of an H-atom, which has been observed in several transformations proposed to proceed through high-valent terminal metal-oxo motifs.[28,30] Mechanism (i) proceeds through concerted C–H insertion and elimination of iodobenzene, avoiding generation of a high-valent terminal manganese-oxo. The direct oxygenation of substrates by manganese oxidant adducts has been demonstrated for several manganese-porphyrin complexes.[31-34] Mechanisms (ii)-(iv) invoke the transient formation of a high-valent terminal manganese-oxo that directly activates the phenyl ring. Whereas mechanism (iii) is expected to operate through a large KIE,

mechanisms (i), (ii), and (iv) are proposed to illustrate a small or absence KIE. Preliminary DFT calculations support the assignment of the terminal metal-oxo complex as $[Mn^{IV}Mn^{III}{}_2Mn^{II}]^{2+}$ in lieu of $[Mn^{III}{}_4]^{2+}$, likely due to the terminal oxygen atom localizing charge on the adjacent manganese ion. Density functional theory (DFT) calculations are underway to elucidate the thermodynamics of each proposed pathway. The analogous pathways are proposed for **1.3**.

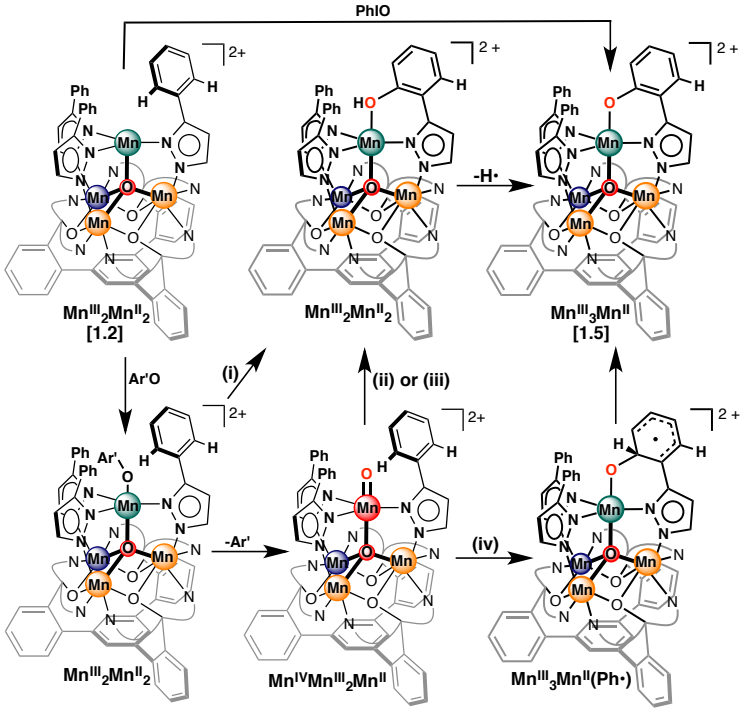


**Figure 1.16**. Proposed mechanisms for synthesis of complex **1.5**, involving (i) concerted C–H insertion by an oxidant-adduct, (ii) concerted C–H insertion by a terminal manganese-oxo, (iii) H-atom abstraction and radical rebound, or (iv) radical arene activation.

In pursuit of identifying the active species for arene functionalization, low-temperature and variable-temperature $^1$H-NMR experiments have been performed on **1.7**. Addition of soluble iodosobenzene (5 equiv.) to **1.7** in $CD_2Cl_2$ at -80ºC affords an intermediate species distinct from both **1.7** and **1.10** at -80 ºC. This $^1$H-NMR spectrum at -80 ºC does not change over a ten-hour period. Upon raising the temperature, complex **1.12** appears at -66 ºC with complete conversion to **1.12** occurring at -50 ºC. No additional paramagnetic shifts for additional intermediates are observed. Addition of oxidant $TBAIO_4$ (5 equiv.) to **1.7** at -80 ºC resulted in a different $^1$H-NMR

spectrum, suggesting a distinct intermediate species. Warming to -50 ºC similarly affords the $^{1}$H-NMR spectrum of **1.12**. Assuming both oxidants operate through common intermediates and an identical mechanism, this result suggests these intermediates are oxidant adducts. Nonetheless, a Mn(IV)=O species may still be responsible for the arene activation.

**1.3 Summary and Conclusions.** Two series of homometallic, tetra-manganese clusters with general formula $[LMn_3(PhPz)_3OMn][OTf]_x$ (x = 1 (**1.3**), 2 (**1.2**)) and $[LMn_3(F_2ArPz)_3OMn][OTf]_x$ (x = 1 (**1.7**), 2 (**1.8**)) were synthesized in a modular approach from $LMn_3(OAc)(OTf)_2$ (**1.1**). The synthesis of these clusters is inspired by the site-differentiation of the oxygen-evolving complex of photosystem II in which four metal ions are coordinated through a $\mu_4$-oxygen atom bridge. All complexes were characterized by $^{1}$H/$^{19}$F-NMR, CV, single-crystal XRD, and ESI-MS. These structures are supported solely by weak-field ligands and demonstrate charge localization as ascertained from bond parameters. Addition of the oxygen-atom transfer reagent iodosobenzene (PhIO) to **1.2** and **1.3** resulted in C–H oxygenation of the bridging phenyl pyrazolate. Addition of PhIO to **1.7** and **1.8** similarly resulted in arene hydroxylation (C–F activation) and F-transfer to unreacted starting material. Both arene activation events were confirmed by independently synthesis by pyrazolate/phenolate ligand exchange. Oxygenation of C($sp^2$)–H and C($sp^2$)–F bonds is proposed to proceed via a highly-reactive manganese-oxo intermediate. In reference to the oxygen-evolving complex, these results suggest that the mechanism for water oxidation may proceed through a high-valent terminal oxo, capable of similarly activating strong C–H bonds.

## Chapter 2. Intramolecular C–H Activation by Heterometallic $Fe_3Mn$ Clusters

**Abstract**. Site-differentiated heterometallic clusters of the general formula $[LFe_3(PhPz)_3OMn][OTf]_x$ (x = 2 (**2.1-Mn**), 3 (**2.3-Mn**)) were synthesized and characterized. A tri-nucleating ligand supports a tri-iron core, connected to a site-differentiated apical manganese ion through a bridging $\mu_4$-oxygen atom and three phenyl phyrazolate (PhPz) ligands. The steric protection provided by the phenyl rings engenders a vacant coordination site on the apical manganese, providing an excellent entry to explore the synthesis of a $Mn^{IV}$-oxo motif in a multimetallic scaffold. Characterization by zero-field $^{57}$Fe Mössbauer spectroscopy confirms the presence of a manganese metal center in the apical position. Treatment of these clusters with iodosobenzene furnishes $[LFe_3(PhPz)_2(OArPz)OMn][OTf]_x$ (x = 2 (**2.4-Mn**), 3 (**2.6-Mn**)) by C–H oxygenation of the proximal phenyl ring. This reactivity is similarly observed for the homometallic clusters $[LFe_3(PhPz)_3OFe][OTf]_x$ (x = 1 (**2.1-Fe**), 2 (**2.2-Fe**), 3 (**2.3-Fe**)) and $[LMn_3(PhPz)_3OMn][OTf]_x$ (x = 1, 2). Interestingly, from the addition of 1-(*tert*-butylsulfonyl)-2-iodosylbenzene (sPhIO) to **2.3-Mn**, an oxidant adduct was isolated and characterized by single-crystal XRD and $^1$H-NMR spectroscopy to reveal $[LFe_3(PhPz)_3OMn(sPhIO)][OTf]_3$ (**2.7-Mn**). Examples of paramagnetic oxidant-capped complexes are extremely scarce, and this example is the first iodosobenzene adduct in a multimetallic scaffold. Complex **2.7-Mn** further reacts to yield **2.6-Mn** after several hours at room temperature. The relative thermal stability of **2.7-Mn** is unparalleled for the homometallic analogs. Mechanistic pathways responsible for C–H oxygenation are discussed.

**2.1 Introduction**. High-valent terminal metal-oxos are proposed as reactive intermediates for a myriad of biological transformations, including the O–O bond coupling step by the oxygen-evolving complex of photosystem II[35] and $O_2$ reduction by cytochrome *c* oxidase.[36] To avoid the formation of kinetically-unfavorable and thermodynamically-unfavorable intermediates, biological enzymes position multiple metal sites in close proximity to facilitate multi-electron transformations. Although several monometallic manganese-oxo[21] and iron-oxo[37] motifs have been characterized by XRD and explored by spectroscopic methods, isolation of terminal metal-oxo motifs on a multimetallic framework remains elusive.

We previously reported a site-differentiated tetra-iron cluster $[LFe_3(PhPz)_3OFe][OTf]_x$ (x = 1–3) in which redox changes exclusively occurred at a remote site of the cluster.[25] Treatment of these clusters with iodosobenzene resulted in C–H oxygenation of the supporting phenyl pyrazolate ligand (Figure 2.1). We were interested in performing structure-function studies to probe how altering the active site – while maintaining the tri-iron core and supporting ligand constant – would influence the observed reactivity of this cluster. Since manganese possesses fewer *d* electrons than iron has, we postulated a terminal manganese-oxo would be less reactive than a terminal iron-oxo and provide an opportunity to characterize a putative high-valent metal oxo.

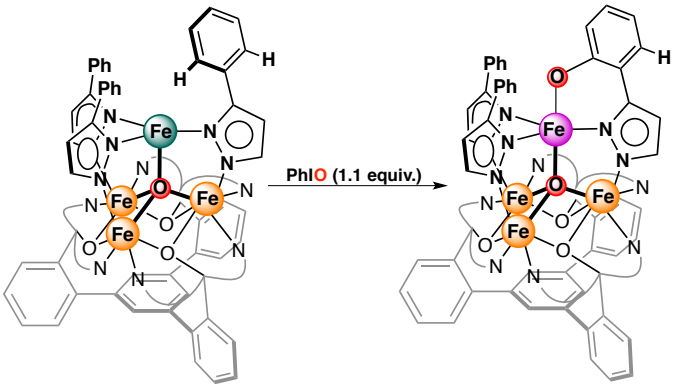


**Figure 2.1.** Reaction of tetra-iron cluster with iodosobenzene results in C–H oxygenation of phenyl pyrazole.

Herein, we describe the synthesis and characterization of $[LFe_3(PhPz)_3OMn][OTf]_x$ (x = 2 (**2.1-Mn**), 3 (**2.3-Mn**)), Scheme 2.1. These clusters consist of site-differentiated (apical) manganese, appended to tri-iron core through a $\mu_4$-oxygen atom and three phenyl pyrazolate ligands. The tri-iron core is supported by weak-field alkoxide and pyridine donors connected by a tri-aryl benzene framework. Zero-field $^{57}$Fe Mössbauer spectroscopy confirms the presence of a manganese ion in the apical position. Exposure of both **2.1-Mn** and **2.3-Mn** to oxygen-atom transfer reagents results in C–H oxygenation of a bridging pyrazolate ligand. This reactivity is similar to that observed in the corresponding tetra-iron and tetra-manganese analogs. Remarkably, the reaction of **2.3-Mn** with 1-(*tert*-butylsulfonyl)-2-iodosylbenzene (sPhIO) yields a thermally-sensitive intermediate which performs C–H oxygenation at room temperature. Characterization by XRD reveals an usual sPhIO adduct $[LFe_3(PhPz)_3OMn(sPhIO)][OTf]_3$ (**2.7-Mn**) with an intact I=O bond. Presumably, the reaction of **2.1-Mn** with sPhIO proceeds through an analogous sPhIO adduct prior to the formation of **2.4-Mn**, and this behavior is proposed to be general for the homometallic analogs. The mechanism responsible for arene hydroxylation is discussed.

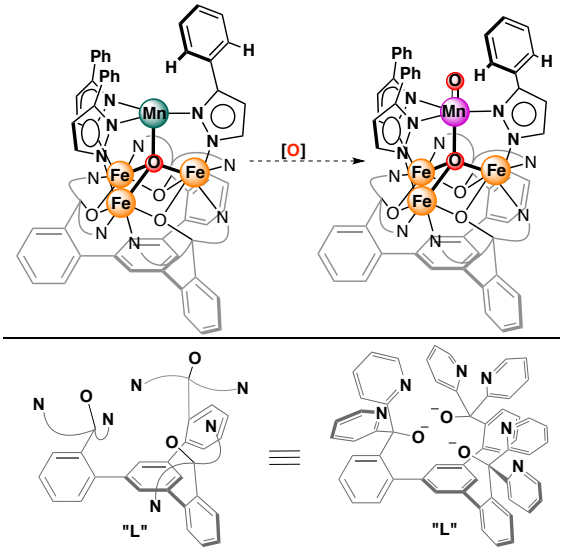


**Scheme 2.1.** Envision installation of terminal oxygen atom on heterometallic cluster supported by phenyl pyazolate ligands. The tri-iron core is supported by a tri-nucleating ligand ($\mathbf{L}^{3-}$).

**2.2 Results and Discussion.** The synthesis of the heterometallic cluster $[LFe_3(PhPz)_3OMn][OTf]_2$ was envisioned to proceed by salt metathesis from the previously reported cluster $[LFe_3(PhPz)_3ONa][OTf]$.[25] Indeed, addition of $Mn(OTf)_2(MeCN)_2$ (2.0 equiv.) to $[LFe_3(PhPz)_3ONa][OTf]$ as resulted in the formation of $[LFe_3(PhPz)_3OMn][OTf]_2$ (**2.1-Mn**) as a dark orange-brown solid in good yield (85 %), (Figure 2.2). The $^1$H-NMR spectrum is paramagnetically shifted over several 100 ppm and is distinct from the starting material and from that of $[LFe_3(PhPz)_3OFe][OTf]_2$. The site-specific installation of the manganese ion in the apical position was confirmed by zero-field $^{57}$Fe Mössbauer spectroscopy. The Mössbauer spectrum of **2.1-Mn** is satisfactorily modeled as three quadrupole doublets in an equal 1:1:1 ratio, consistent with the presence of three iron metal centers in distinct chemical environments. The isomer shift and quadrupole splitting for two quadrupole doublets ($\delta$ = 0.45 mm/s, $|\Delta E_Q|$ = 0.46 mm/s and $\delta$ = 0.48 mm/s, $|\Delta E_Q|$ = 0.89 mm/s) are consistent with two high-spin six-coordinate Fe(III) metal centers.[38] The remaining isomer shift and quadrupole splitting ($\delta$ = 1.14 mm/s, $|\Delta E_Q|$ = 3.22 mm/s) is consistent with a high-spin six-coordinate Fe(II) metal center, (Table 2.1).[39-43] These parameters resemble those observed for $[LFe_3(PhPz)_3OFe][OTf]_2$ (**2.1-Fe**; Table 2.1).[25] Moreover, the characteristic quadrupole doublet for the apical iron ($\delta$ = 0.859 mm/s, $|\Delta E_Q|$ = 1.563 mm/s) is absent in the Mössbauer spectrum of **2.1-Mn**, indicating the desired substitution of manganese into the apical position. Modeling **2.1-Mn** with four quadrupole doublets results in an unsatisfactory model, suggestive of only three iron metal centers in the complex.

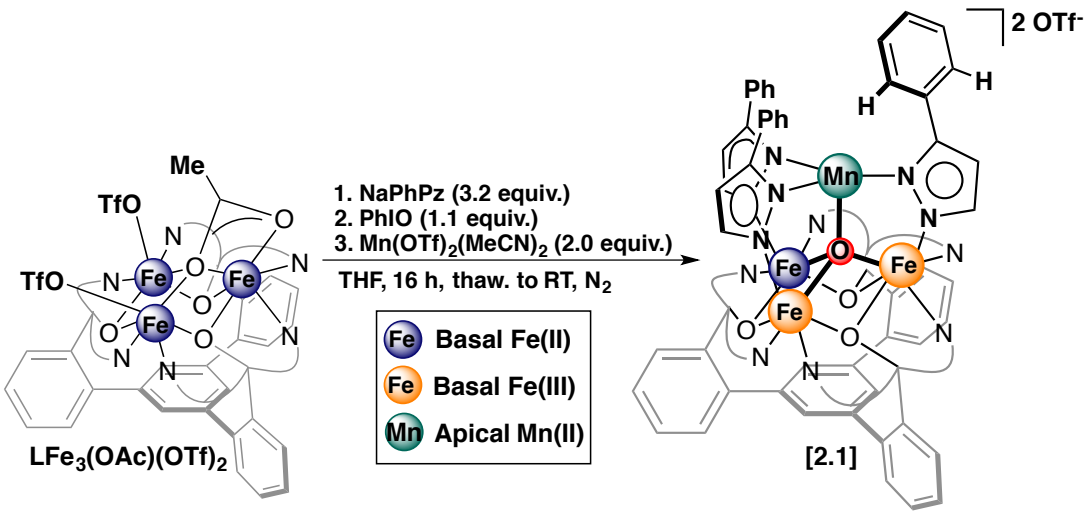


**Figure 2.2.** Synthesis of complex **2.1**.

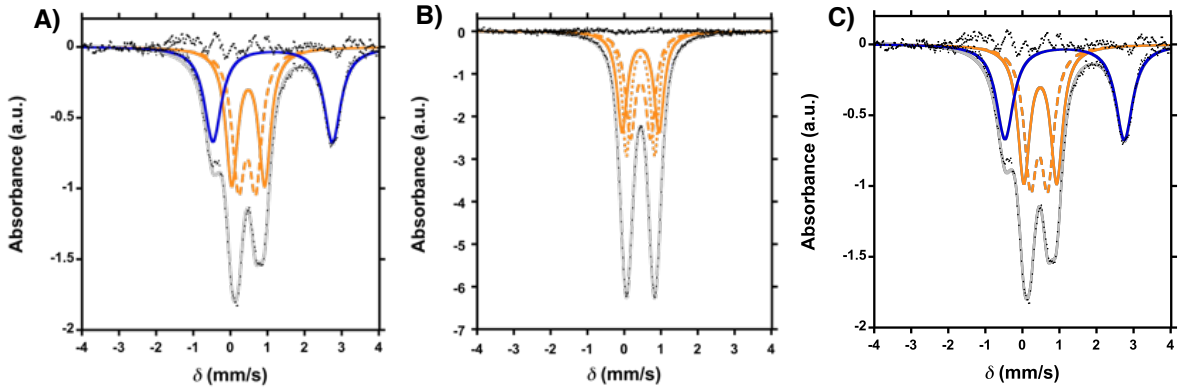


**Figure 2.3.** Zero-field $^{57}$Fe Mössbauer spectra at 80 K of (A) $[LFe_3(PhPz)_3OMn][OTf]_2$ (**2.1-Mn**) with simulated parameters: (i) $\delta = 0.45$ mm/s, $|\Delta E_Q| = 0.46$ mm/s (dashed orange trace); (ii) $\delta = 0.48$ mm/s, $|\Delta E_Q| = 0.89$ mm/s (solid orange trace); (iii) $\delta = 1.14$ mm/s, $|\Delta E_Q| = 3.22$ mm/s (solid blue trace). (B): $[LFe_3(PhPz)_3OMn][OTf]_3$ (**2.3-Mn**) with simulated parameters: (i) $\delta = 0.447$ mm/s, $|\Delta E_Q| = 1.005$ mm/s (dashed orange trace); $\delta = 0.447$ mm/s, $|\Delta E_Q| = 0.55$ mm/s (dotted orange trace); $\delta = 0.45$ mm/s, $|\Delta E_Q| = 0.77$ mm/s (solid orange trace). (C): $[LFe_3(PhPz)_2(OArPz)OMn][OTf]_2$ (**2.4-Mn**) with simulated parameters: (i) $\delta = 0.45$ mm/s, $|\Delta E_Q| = 0.59$ mm/s (dashed orange trace); (ii) $\delta = 0.47$ mm/s, $|\Delta E_Q| = 1.08$ (solid orange trace); (iii) $\delta = 1.11$ mm/s, $|\Delta E_Q| = 3.09$ mm/s (solid blue trace). The gray line is a spectral fit of the data.

X-ray quality crystals of **2.1-Mn** were grown by diffusion of diethyl ether into a concentrated solution of **2.1-Mn** in acetonitrile. The structure is analogous to that of **2.1-Fe** in which the basal iron centers (Fe1–Fe3) exhibit two relatively short Fe–O1 bond distances (1.999(3) Å, Fe2–O1; 1.937(2) Å, Fe3–O1) and one long Fe–O1 bond distance (2.079(2) Å, Fe1–O1; Figure 2.4A and

Table 2.2). The three iron atoms are in a pseudo-octahedral environment and coordinately saturated. The apical manganese is coordinated to the tri-iron core by a $\mu_4$-oxygen (1.980(2) Å, Mn1–O1) and resides in a trigonal pyramidal environment.

**Table 2.1**. Zero-field $^{57}$Fe Mössbauer parameters for **2.1**, **2.3**, and **2.4**.

| No. | Ref. | Complex | Parameters | | |
|---|---|---|---|---|---|
| | | | δ | $\|\Delta E_Q\|$ | % |
| **2.1-Mn** | *a* | $[LFe_3(PhPz)_3OMn][OTf]_2$ | 0.452 | 0.462 | 36 |
| | | | 0.484 | 0.887 | 36 |
| | | | 1.140 | 3.218 | 36 |
| **2.1-Fe** | *25* | $[LFe_3(PhPz)_3OFe][OTf]_2$ | 0.431 | 0.413 | 26 |
| | | | 0.475 | 0.927 | 26 |
| | | | 1.138 | 3.190 | 26 |
| | | | 0.859 | 1.563 | 26 |
| **2.3-Mn** | *a* | $[LFe_3(PhPz)_3OMn][OTf]_3$ | 0.447 | 1.005 | 34 |
| | | | 0.447 | 0.548 | 34 |
| | | | 0.448 | 0.771 | 34 |
| **2.3-Fe** | *25* | $[LFe_3(PhPz)_3OFe][OTf]_3$ | 0.394 | 0.667 | 27 |
| | | | 0.442 | 0.966 | 27 |
| | | | 0.501 | 0.662 | 27 |
| | | | 0.811 | 1.089 | 27 |
| **2.4-Mn** | *a* | $[LFe_3(PhPz)_2(OArPz)OMn][OTf]_2$ | 0.452 | 0.592 | 37 |
| | | | 0.468 | 1.082 | 37 |
| | | | 1.109 | 3.085 | 37 |
| **2.4-Fe** | *25* | $[LFe_3(PhPz)_2(OArPz)OFe][OTf]_2$ | 0.40 | 1.72 | 26 |
| | | | 0.47 | 0.99 | 26 |
| | | | 0.47 | 0.56 | 26 |
| | | | 1.17 | 2.96 | 26 |

[a]This work. All δ and $|\Delta E_Q|$ values are reported in mm/s.

Due to the presence of two outer-sphere triflate anions in the asymmetric unit cell, the apical manganese is assigned as Mn(II). The Mössbauer spectrum and solid-state data together corroborate the substitution of manganese into the apical position with an intact tri-iron core.

To probe the range of accessible oxidation states for **2.1-Mn**, the electrochemical properties were investigated by cyclic voltammogram (CV). The CV of **2.1-Mn** is shown in Figure 2.5 (maroon trace), and displays three reversible redox event corresponding to $[Fe^{II}_3Mn^{II}]^0/[Fe^{II}_2Fe^{III}Mn^{II}]^{1+}$ (-1.79 V vs. $Fc/Fc^{1+}$), $[Fe^{II}_2Fe^{III}Mn^{II}]/[Fe^{II}Fe^{III}_2Mn^{II}]^{2+}$ (-0.68 V), and $[Fe^{II}Fe^{III}_2Mn^{II}]/[Fe^{III}_3Mn^{II}]^{3+}$ (0.05 V). These features are reminiscent of the CV for **2.1-Fe** in

which three reversible redox events at nearly identical reduction potentials are observed: $[Fe^{II}_4]^0/[Fe^{II}_3Fe^{III}]^{1+}$ (-1.72 V vs. $Fc/Fc^{1+}$), $[Fe^{II}_3Fe^{III}]^{1+}/[Fe^{II}_2Fe^{III}_2]^{2+}$ (-0.72 V vs. $Fc/Fc^{1+}$), and $[Fe^{II}_2Fe^{III}_2]^{2+}/[Fe^{II}Fe^{III}_3]^{3+}$ (0.02 V vs. $Fc/Fc^{1+}$).[25] The similarities between the CVs for **2.1-Fe** and **2.1-Mn** are suggestive of the changes in electron count for **2.1-Mn** occurring strictly in the tri-iron core.

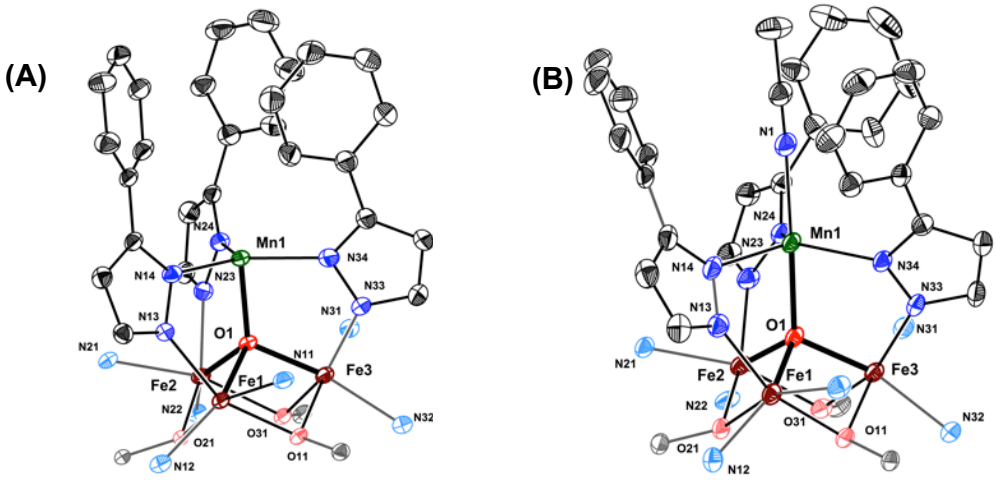


**Figure 2.4**. Truncated molecular structures of **2.1-Mn** (A) and **2.3-Mn** (B). Thermal ellipsoids are shown at the 50% probability level. Triflate counter anions, solvents, and hydrogen atoms are omitted for clarity.

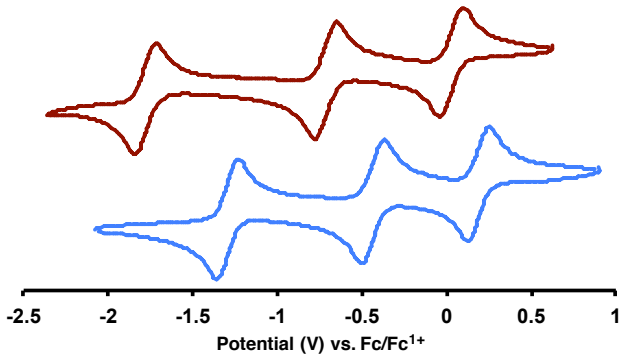


**Figure 2.5**. CVs of $[LFe_3(PhPz)_3OMn][OTf]_2$ (**2.1-Mn**, maroon) and $[LFe_3(PhPz)_2(OArPz)OMn][OTf]_2$ (**2.4-Mn**, sky blue). The CV's were recorded at scan rate of 100 mV $s^{-1}$ in $CH_2Cl_2$ and referenced against $Fc/Fc^{1+}$. Both samples were measured at concentration 2 mM with glassy carbon, Pt-wire, and Ag-wire as working, counter, and reference electrode, respectively. $TBAPF_6$ (0.1 M) was employed as the supporting electrolyte.

**Table 2.2**. Select bond parameters for **2.1-Mn**, 2**.3-Mn**, **2.4-Mn**, **2.5-Mn**, and **2.7-Mn**.

| Bond Distances (Å) | Complex | | | | |
|---|---|---|---|---|---|
| | **2.1-Mn** | **2.3-Mn** | **2.4-Mn** | **2.5-Mn** | **2.7-Mn** |
| Fe1–O1 | 2.079(2) | 1.985(3) | 2.140(6) | 2.087(3) | 1.994(7) |
| Fe2–O1 | 1.999(3) | 1.980(3) | 2.009(4) | 2.135(3) | 1.989(7) |
| Fe3–O1 | 1.937(2) | 1.972(3) | 2.007(5) | 1.973(3) | 1.967(6) |
| Mn1–O1 | 1.980(2) | 2.122(3) | 1.876(4) | 1.829(3) | 2.104(7) |
| Fe1–N11 | 2.227(3) | 2.118(4) | 2.206(6) | 2.157(4) | 2.167(9) |
| Fe1–N12 | 2.136(3) | 2.187(3) | 2.128(6) | 2.225(4) | 2.104(9) |
| Fe1–N13 | 2.116(3) | 2.037(4) | 2.112(6) | 2.140(4) | 2.104(9) |
| Fe2–N21 | 2.221(3) | 2.105(3) | 2.199(6) | 2.148(4) | 2.173(9) |
| Fe2–N22 | 2.142(3) | 2.192(4) | 2.141(5) | 2.288(4) | 2.125(9) |
| Fe2–N23 | 2.115(3) | 2.038(4) | 2.069(7) | 2.125(4) | 2.065(9) |
| Fe3–N31 | 2.203(3) | 2.134(4) | 2.208(7) | 2.164(4) | 2.147(9) |
| Fe3–N32 | 2.141(3) | 2.193(3) | 2.116(8) | 2.250(4) | 2.213(9) |
| Fe3–N33 | 2.078(3) | 2.038(4) | 2.058(5) | 2.105(4) | 2.04(1) |
| Mn1–N14 | 2.101(3) | 2.151(4) | 2.045(5) | 2.004(5) | 2.18(1) |
| Mn1–N24 | 2.117(3) | 2.165(3) | 2.119(7) | 2.131(4) | 2.173(9) |
| Mn1–N34 | 1.380(4) | 2.158(4) | 2.021(6) | 2.101(4) | 2.164(9) |
| N13–N14 | 1.384(4) | 1.377(5) | 1.38(1) | 1.364(6) | 1.41(1) |
| N23–N24 | 1.388(4) | 1.384(5) | 1.411(7) | 1.375(5) | 1.36(1) |
| N33–N34 | 1.380(4) | 1.391(5) | 1.386(8) | 1.385(6) | 1.38(1) |
| **Bond Angles (°)** | | | | | |
| N14–Mn1–N24 | 119.1(1) | 117.0(1) | 115.1(2) | 111.8(2) | 115.2(4) |
| N24–Mn1–N34 | 120.4(1) | 122.7(1) | 118.3(2) | 115.7(2) | 126.8(4) |
| N34–Mn1–N14 | 120.6(1) | 116.0(1) | 126.1(2) | 132.3(2) | 113.4(3) |
| **Torsion Angles (°)** | | | | | |
| Fe1–N13–N14–Mn1 | 3.0(3) | 17.2(4) | -11.4(7) | -18.8(5) | -23(1) |
| Fe2–N23–N24–Mn1 | -1.1(3) | 29.8(4) | -12.0(6) | 11.1(4) | -30(1) |
| Fe3–N33–N34–Mn1 | -1.6(3) | 16.3(4) | -9.5(7) | 16.2(4) | -14(1) |
| **Centroid Distances (Å)** | | | | | |
| Fe1\|Fe2\|Fe3–N14\|N24\|N34 | 2.923 | 2.763 | 2.824 | 2.889 | 2.750 |
| Fe1\|Fe2\|Fe3–O11\|O21\|O31 | 1.081 | 1.080 | 1.053 | 1.084 | 1.090 |
| Fe1\|Fe2\|Fe3–O1 | 0.946 | 0.899 | 1.035 | 1.113 | 0.918 |
| N14\|N24\|N34–O11\|O21\|O31 | 4.003 | 3.843 | 3.875 | 4.023 | 3.840 |

With the electrochemical properties of **2.1-Mn** established, reduction and/or oxidation of **2.1-Mn** was targeted with chemical reductants and oxidants. Treatment of **2.1-Mn** with cobaltocene ($CoCp_2$; 1.1 equiv.) in $CH_2Cl_2$ afforded a red-purple solution with a $^1$H-NMR spectrum indicative of a new paramagnetic species, assigned as $[LFe_3(PhPz)_3OMn][OTf]$ (**2.2-Mn**). Gradual metal scrambling to $[LFe_3(PhPz)_3OFe][OTf]$ (**2.2-Fe**) was observed, which precluded

further characterization and reactivity studies (Appendix A.11). Treatment of **2.1-Mn** with decamethylcobaltocene ($CoCp_2$*, 2.1 equiv.) in MeCN afforded a solid insoluble in all solvents and is postulated to be $LFe_3(PhPz)_3OMn$. Nonetheless, addition of silver triflate (AgOTf; 1.1 equiv.) to **2.1-Mn** furnished a deep purple solution with a new paramagnetic $^1$H-NMR spectrum. The zero-field $^{57}$Fe Mössbauer spectroscopy is consistent with three iron metal centers in similar chemical environments. The Mossbauer spectrum is best modeled with three quadrupole doublets in a 1:1:1 ratio, (Figure 2.4B and Table 2.1). The isomer shifts and quadrupole splittings are consistent with three six-coordinate Fe(III) metal centers ($\delta$ = 0.447 mm/s, $|\Delta E_Q|$ = 1.005 mm/s; $\delta$ = 0.447 mm/s, $|\Delta E_Q|$ = 0.548 mm/s; $\delta$ = 0.447 mm/s, $|\Delta E_Q|$ = 0.771 mm/s), (Figure 2.3 and Table 2.1). These parameters resemble those for $[LFe_3(PhPz)_3OFe][OTf]_3$ (**2.3-Fe**) and are consistent with a $Fe^{III}_3$ tri-iron core.[25,38] Crystallization from vapor diffusion of diethyl ether into a concentrated solution of **2.3-Mn** in acetonitrile yielded single crystals in 60 % yield. The bond parameters of the $Fe_{core}$–O1 distances are similar (1.972(3) Å, Fe3–O1; 1.980(3) Å, Fe2–O1; 1.985(3) Å, Fe1–O1), consistent with the $Fe^{III}_3$ core (Figure 2.4B and Table 2.2). The apical manganese (2.122(3) Å, Mn1–O1) is assigned as $Mn^{II}$ based on charge balance.

The formation of a high-valent terminal manganese-oxo from **2.1-Mn** and **2.3-Mn** was attempted, (Figure 2.6). Treatment of **2.1-Mn** with 1-(*tert*-butylsulfonyl)-2-iodosylbenzene (sPhIO) afforded a dark brown solution with a paramagnetic $^1$H-NMR spectrum consistent with a new species of lower symmetry. Electrospray ionization mass spectrometry (ESI-MS) showed a single peak corresponding to oxygen atom incorporation and loss of an H-atom. Single crystals were grown by diffusion of diethyl ether into a concentrated solution of the crude mixture in acetonitrile to provide $[LFe(PhPz)_2(OArPz)OMn][OTf]_2$ (**2.4-Mn**).

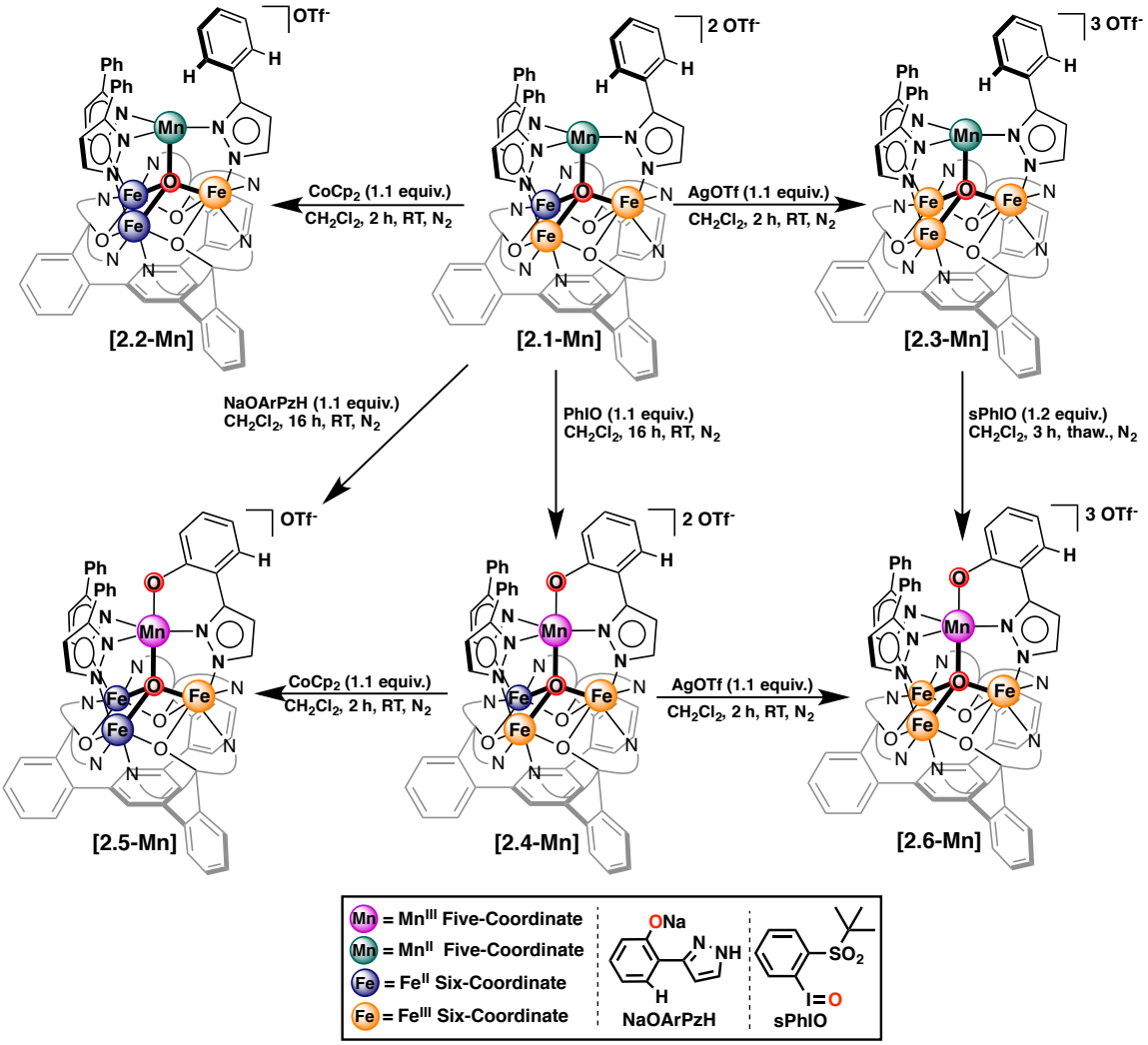


**Figure 2.6**. Synthesis of complexes **2.1-Mn** through **2.7-Mn**.

The $Fe_{core}$–O1 bond distances for **2.4-Mn** (Fe1–O1 (2.140(6) Å), Fe2–O1 (2.009(4) Å), and Fe3–O1 (1.876(4) Å)) closely resemble those of **2.4-Fe** (Figure 2.7A and Table 2.2).[25] Based on charge balance, the apical manganese is $Mn^{III}$, and the tri-iron core has oxidation states $Fe^{II}Fe^{III}_2$. The Mn4–O1 bond distance of 1.876(4) Å in **2.4-Mn** is similar to that of **2.4-Fe**. The zero-field $^{57}$Fe Mössbauer spectrum is best modeled as three doublets in a 1:1:1 ratio with two high-spin ferric iron metal centers ($\delta$ = 0.452 mm/s, $|\Delta E_Q|$ = 0.592 mm/s; $\delta$ = 0.468 mm/s, $|\Delta E_Q|$ = 1.082 mm/s) and one high-spin ferrous iron center ($\delta$ = 1.109 mm/s, $|\Delta E_Q|$ = 3.085 mm/s), (Figure 2.2 and Table 2.1).[27] The Mössbauer spectrum is near-identical to that of **2.1-Mn,** suggesting

oxidation from Mn(II) to Mn(III). The CV for **2.4-Mn** shows three reversible redox events: $[Fe^{II}_3Mn^{III}]^0/[Fe^{II}_2Fe^{III}Mn^{III}]^{1+}$ (-1.31 V vs. $Fc/Fc^{1+}$), $[Fe^{II}_2Fe^{III}Mn^{III}]/[Fe^{II}Fe^{III}_2Mn^{III}]^{2+}$ (-0.44 V), and $[Fe^{II}Fe^{III}_2Mn^{III}]/[Fe^{III}_3Mn^{III}]^{3+}$ (0.18 V), (Figure 2.5, sky blue trace). Complex [LFe(PhPz)$_2$(OArPz)OMn][OTf] (**2.5-Mn**) was synthesized by addition of NaOArPzH (1.1 equiv.) to **2.1-Mn**, and X-ray quality crystals were grown by diffusion of diethyl ether into a concentrated solution of **2.5-Mn** in acetonitrile (Figure 2.7B and Table 2.2).

Treatment of **2.1-Mn** with excess sPhIO (5 equiv.) at -78 ºC in $CD_2Cl_2$ afforded a paramagnetic $^1$H-NMR spectrum distinct from **2.1-Mn** and **2.4-Mn**, (Figure S25). Warming the sample from -70 ºC to - 30 ºC resulted in partial formation of **2.4-Mn**, and complete conversion to **2.4-Mn** was observed upon warming to 10 ºC.

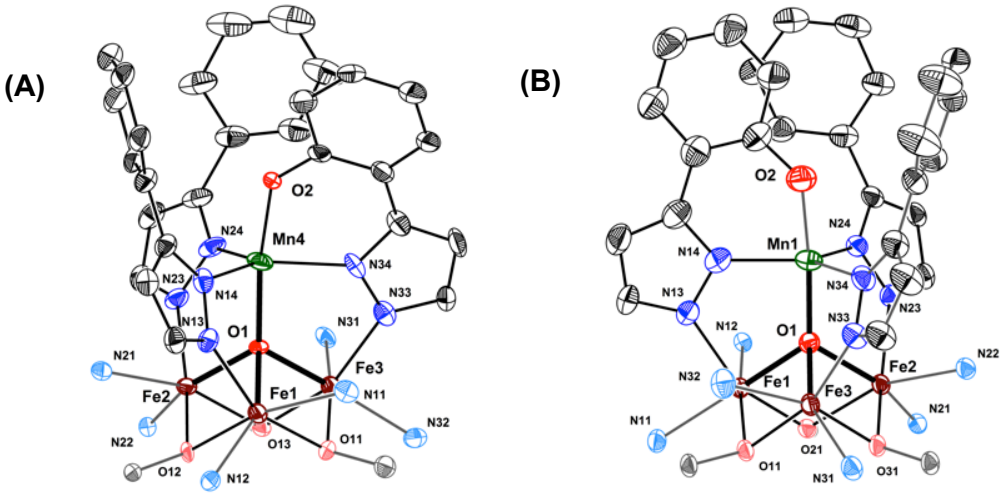


**Figure 2.7.** Truncated molecular structures of **2.4-Mn** (A) and **2.5-Mn** (B). Thermal ellipsoids are shown at the 50% probability level. Triflate counter anions, solvents, and hydrogen atoms are omitted for clarity.

Treatment of **2.3-Mn** with sPhIO (5 equiv.) in thawing $CH_2Cl_2$ yields a brown-violet paramagnetic $^1$H-NMR spectrum of an asymmetric species, suggestive of [LFe(PhPz)$_2$(OArPz)OMn][OTf]$_3$ (**2.6-Mn**). Although single crystals of **2.6-Mn** have not been successfully isolated (Appendix A.11), the $^1$H-NMR of **2.6-Mn** is reproduced by treatment of

**2.4-Mn** with AgOTf (1.1 equiv.) in $CH_2Cl_2$. Addition of sPhIO to **2.3-Mn** at low temperatures results in a purple-violet species that converts into **2.6-Mn** over several hours at room temperature. Single crystals of this intermediate species were grown at -35 ºC by layering a mixture of **2.4-Mn** and sPhIO in $CH_2Cl_2$ with toluene over two weeks. Single-crystal XRD revealed the structure as the iodosobenzene-bound adduct, $[LFe(PhPz)_3OMn(^{s}PhIO)][OTf]_3$ (**2.7-Mn**), (Figure 2.8 and Figure 2.9). The O2–I1 bond is unaffected upon coordination to Mn1 (1.873(9) Å vs. 1.848(6) Å).[44] The bond distance of $Fe_{core}$–O1 are consistent with a $Fe^{III}_3$ core (1.994(7) Å, Fe1–O1; 1.989(7) Å, Fe2–O1; 1.967(6) Å, Fe3–O1). Interestingly, treatment of **2.3-Fe** with sPhIO (5 equiv.) in $CH_2Cl_2$ results in immediate conversion to $[LFe(PhPz)_2(OArPz)OFe][OTf]_3$ (**2.6-Fe**) at room temperature. Exposure of **2.6-Mn** to acetonitrile quantitatively yields **2.3-Mn**, supporting the inactivation of sPhIO upon coordination.

We suspect the prolonged lifetime of **2.7-Mn** is consequent of the electron-deficient trication heterometallic and higher oxidation potential of manganese resulting in the delayed onset of oxidation to yield a putative $Mn^{IV}$-oxo. We propose the $^1$H-NMR spectrum of the intermediate at -78 ºC for conversion of **2.1-Mn** into **2.4-Mn** similarly represents an iosodobenzene-adduct, $[LFe(PhPz)_3OMn(^{s}PhIO)][OTf]_2$ (**2.8-Mn**). Non-porphyrin iodosobenzene adducts have been reported previously for manganese,[45,46] iron,[47] and rhodium.[48] The isolation of **2.7-Mn** is the first example of an oxidant adduct within a multimetallic framework, thus providing an opportunity to study the mechanism of oxygen-atom transfer to different substrates.

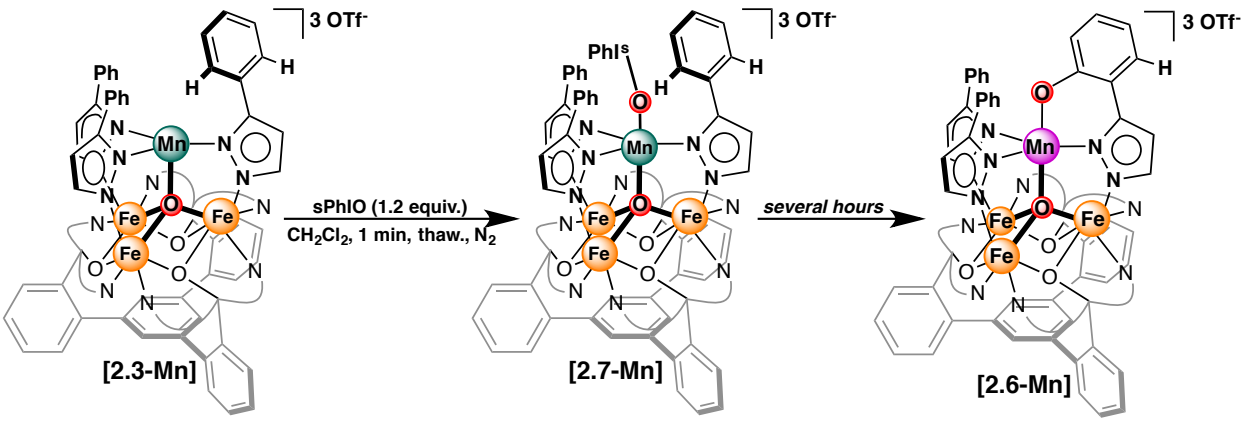


**Figure 2.8.** Synthesis of **2.6-Mn** through intermediate **2.7-Mn**.

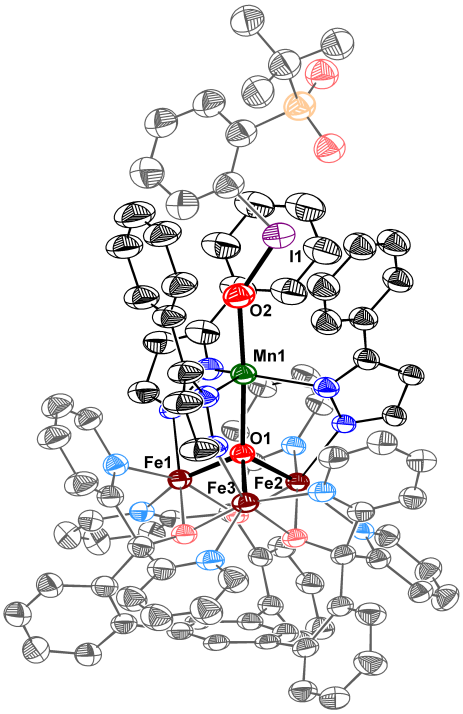


**Figure 2.9**. Molecular structures of **2.6-Mn**. Thermal ellipsoids are shown at the 50% probability level. Triflate counter anions, solvents, and hydrogen atoms are omitted for clarity.

To elucidate the mechanism of C($sp^2$)–H oxygenation, spin-unrestricted density functional theory (DFT) calculations were performed on **2.6-Mn** and the proposed terminal-oxo complex $[LMn_3(PhPz)_3OMnO][OTf]_3$ (**2.9-Mn**). The bond parameters for **2.6-Mn** were satisfactorily reproduced upon structural optimization with the functional/basis set pairing lacvp**/B3LYP-

d3[49,50,51] by assuming an overall spin of S = 21/2 ($[Fe^{III}_3Mn^{II}]^{3+}$). The lowest-energy ground state for **2.9-Mn** was isolated for the overall spin S = 19/2 ($[Fe^{III}_3Mn^{IV}]^{3+}$). The electronic manifold for **2.9-Mn** consists of π* interactions between the Mn *d* orbital set and proximal ligands. Whereas the two lowest-energy SOMO's consist of $d_{xy}/d_{x2-y2}$ antibonding with the pyrazolate π system, the HOMO consist of a $Mn(d_{yz})/O(p_y)$ π* interaction with significant contribution from the π system of the phenyl rings, (Figure 2.10). The LUMO and LUMO+1 respectively consist of π* $Mn(d_{xz})/O(p_x)$ and σ* $Mn(d_{z2})/O(p_z)$ interactions. For the HOMO, the presence of electron density along the Mn–O π vector attenuates the Mn–O bond order and furnishes radical character on the oxygen unit. Furthermore, electronic delocalization between the Mn–O motif and the phenyl ring suggests the oxygen is capable of activating the π system of the arene ring. Analogous computational studies on S = 1 Fe(IV)=O systems have illustrated population of π*-symmetric $Fe(d_{xz})/O(p_x)$ and $Fe(d_{yz})/O(p_y)$ frontier orbitals to furnish radical character on the terminal oxygen, promoting radical-based activation of external C–H bonds.[52] Although direct arene oxygenation by **2.6-Mn** cannot be excluded, this data supports C–H oxygenation to proceed by radical arene activation of the proximal phenyl ring.

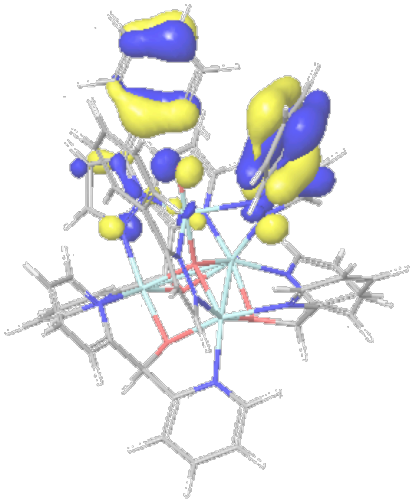

**Figure 2.10**. Highest occupied molecular orbital (SOMO) for **2.9-Mn**.

**2.3 Summary and Conclusions.** A series of heterometallic tri-iron/mono-manganese clusters of the general formula $[LFe_3(PhPz)_3OMn][OTf]_x$ was synthesized and juxtaposed with the previously reported $[LFe_3(PhPz)_3OFe][OTf]_x$ cluster series. All complexes were characterized by $^1H/^{19}F$-NMR, CV, single-crystal XRD, and ESI-MS. These structures are supported solely by weak-field ligands and demonstrate charge localization as ascertained from bond parameters of the solid-state structures. Addition of iodosobenzene (PhIO) to **2.1-Mn** and **2.3-Mn** resulted in C–H oxygenation of the bridging phenyl pyrazolate to furnish $[LFe_3(PhPz)_2(OPhPz)OMn][OTf]_x$. An intermediate prior to formation of **2.6-Mn** was observed and characterized by XRD and $^1H$-NMR spectroscopy to reveal $[LFe_3(PhPz)_3OMn(sPhIO)][OTf]_3$ (**2.7-Mn**). XAS and UV-vis studies are underway to characterize the intermediates responsible for phenyl pyrazolate hydroxylation. Preliminary DFT studies support the accumulation of radical character on a putative $Mn^{IV}$=O motif to result in radical arene activation. Current reactivity studies are underway to address oxygen-atom transfer from **2.7-Mn** to a range of substrates to elucidate the mechanism of oxygen-atom transfer and investigate the feasibility of a high-valent terminal manganese-oxo motif.

## Appendix A. Assorted Crystal Structures and Tangential Projects

### A.1. One-electron oxidation of $[LMn_3(PhPz)_3OMn][OTf]_2$ (1.2) by Addition of AgOTf.

Electrochemical studies of **1.2** showed an irreversible one-electron oxidation at 0.15 V vs. $Fc/Fc^{1+}$, corresponding to the formation of $[LMn_3(PhPz)_3OMn][OTf]_3$ (**A.1**) from **1.2**. Since both **1.3** and **1.4** were isolable despite their quasi-reversible CV features, the synthesis and isolation of **A.1** was targeted. Treatment of **1.2** with AgOTf (1.1 equiv.) in either $CH_2Cl_2$ or MeCN furnished a marked change in the $^1$H-NMR spectrum with a myriad of new paramagnetic shifts as well as paramagnetic $^1$H resonances corresponding to **1.2**. Single crystals amenable to X-ray diffraction were grown, albeit in low yield, by vapor diffusion of diethyl ether into a solution of the crude mixture in acetonitrile. XRD revealed the structure unexpectedly as $LMn_3(PhPz)_3OMn(MeCN)][OTf]_2$ (**A.1'**), (Figure A.1). Interestingly, the coordination of the acetonitrile to the apical metal is distinct from the solid-state structure of **1.2**, despite crystallization under identical conditions. The high-quality data set rules out the possibility of a highly disordered triflate counteranion. We propose the transient formation of $[LMn_3(PhPz)_3OMn(MeCN)][OTf]_3$, followed by electron transfer with a second equivalent of cluster to yield **A.1'** and decomposed product, (Figure A.2). The bond parameter of **A.1'** are reproduced well by DFT by modeling the structure with two implicit triflate counteranions; modeling **A.1'** with three implicit triflate counteranions furnishes significant structural distortions compared to the crystal structure.

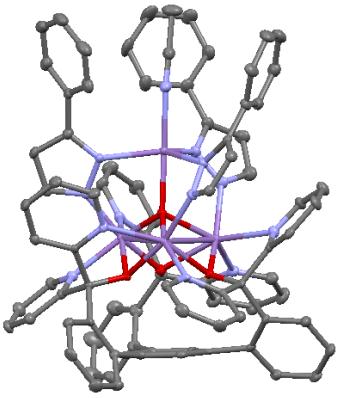

**Figure A.1.** Crystal Structure of **A.1'** with omitted counteranions, solvent, and hydrogen atoms.

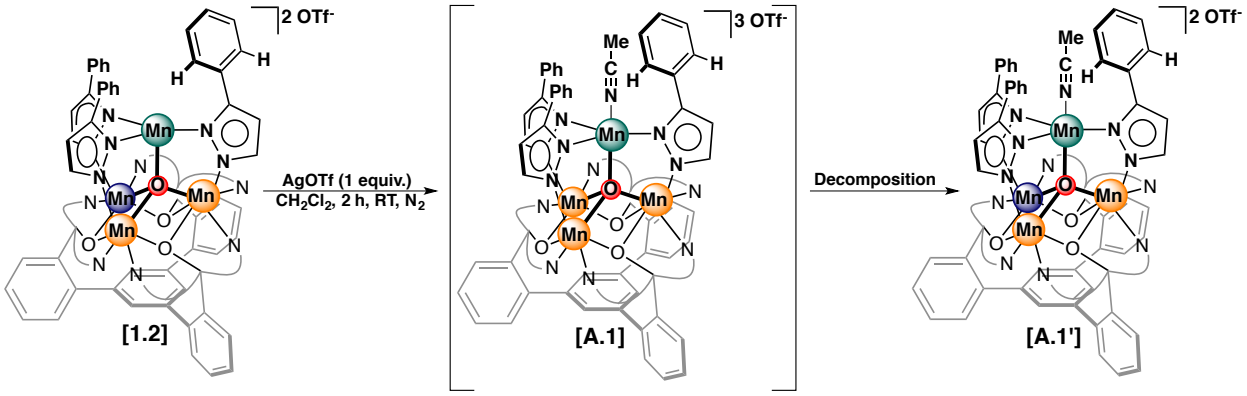


**Figure A.2**. Synthesis of $[LMn_3(PhPz)_3OMn(MeCN)][OTf]_2$ (**A.1'**) with transient formation of $[LMn_3(PhPz)_3OMn(MeCN)][OTf]_3$ (**A.1**).

**A.2**. **Non-oxidative synthesis of $LMn_3(PhPz)_3OMn$ and $LMn_3(F_2ArPz)_3OMn$**.

Toward characterizing **1.5** and **1.6** by single-crystal XRD, counteranion exchange from **1.4** was envisioned to alter the solubility of **1.5** and **1.6**, potentially promoting single-crystal formation. Due to the two-electron reduction of **1.2** to **1.4** proceeding in low-yield, an alternative synthesis procedure starting from **1.1** was envisioned. In a one-pot synthesis, addition of NaPhPz (3.2 equiv.), $Mn(N(SiMe_3)_2)_2$ (1.0 equiv.), and $H_2O$ (1.0 equiv.) to **1.1** afforded a yellow-orange solid, akin to **1.4**, with complete insolubility in all common organic solvents, (Figure A.3). Addition of various one-electron oxidants (including AgOTf, AgOTs, $AgBF_4$, $AgBAr^F_4$, $AgBPh_4$) re-afforded a $^1$H-NMR identical to that of **1.3** with $^{19}$F-NMR reflecting the absence of the OTf counteranion and installation of a new counteranion. Crystallization attempts are

currently underway to provide full characterization of **1.5** and **1.6**. The analogous procedure is applicable with $NaF_2ArPz$ (3.2 equiv.) to synthesize $LMn_3(F_2PhPz)_3OMn$ (**9**), albeit in mediocre yield (45 %).

**A.2. Decomposition and Lability of $[LMn_3(F_2ArPz)_2(OFArPz)OMn][OTf]$.**

Due to the similar solubility properties of **1.10** and **1.11** as well as **1.12** and **1.13**, attempted crystallizations were unsuccessful at isolating the separate clusters from the crude mixture when using PhIO as the oxidant. Instead, independent syntheses of the C–F activated clusters (**1.10**, **12**) and terminal-fluoride clusters (**1.11, 1.13**) were envisioned. Treatment of **1.7** in $CH_2Cl_2$ with sodium 3-fluoro-2-(1*H*-pyrazol-5-yl)phenolate (NaOFArPzH; 1.1 equiv.) led to a rapid darkening of the solution. The resulting $^1$H-NMR spectrum was similar although distinct from the crude reaction **1.8** with PhIO. Crystallization by vapor diffusion of diethyl ether into a concentration solution of the crude product in acetonitrile furnished $[LMn_3(F_2ArPz)_2(OFArPz)OMn][Mn_8O_4(OFArPz)_8]$ (**A.2**) in low yield, (Figure A.3 and Figure A.4). We suspect cluster decomposition is consequent of the high substitutional lability of the fluorinated clusters. Repeating this procedure in thawing $CH_2Cl_2$ results in a $^1$H-NMR spectrum near-identically resembling **10**, indicating that low-temperature ligand-exchange suppresses cluster decomposition.

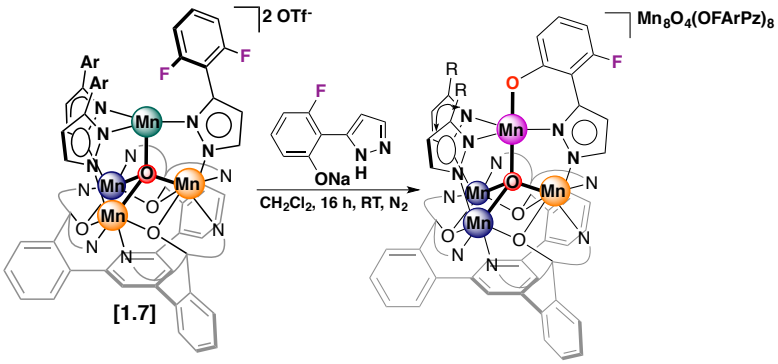


**Figure A.3**. Room-temperature addition of NaOFArPzH to **1.7**, resulting in cluster decomposition.

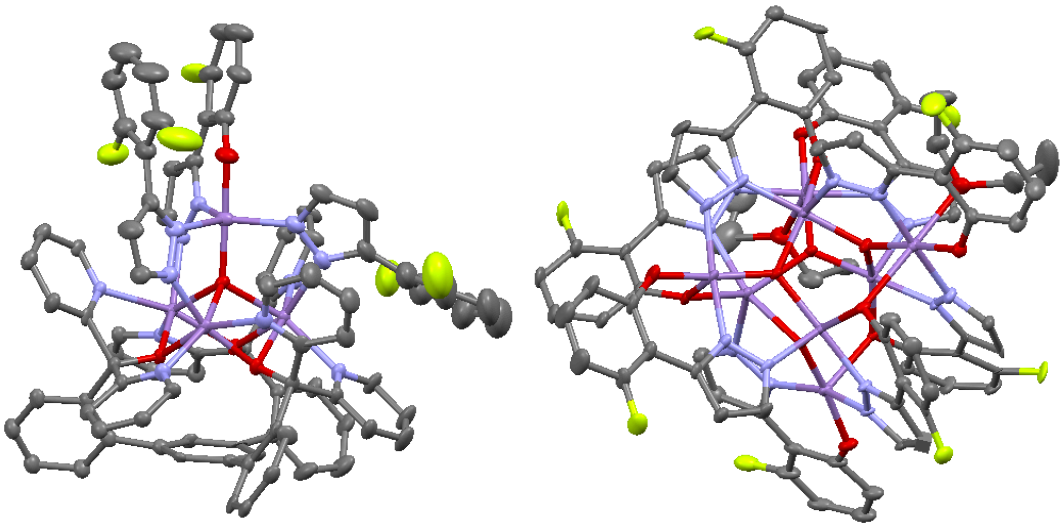

**Figure A.4**. Crystal structure of **A.2** (left) with decomposition counteranion (right). By charge balance, the counteranion is mono-anionic.

### A.3 Hydrolysis of [LMn$_3$(F$_2$ArPz)$_2$(OFPhPz)OMn][OTf].

Crystalline material of presumed **1.10** was obtained by vapor diffusion of diethyl ether into the crude independently prepared **1.10** in acetonitrile. These crystals, shipped to the Advanced Light Source beamline, revealed [LMn$_3$O(MeCN)$_3$][OTf]$_2$, (**A.3**) indicative of cluster decomposition (Figure A.5). The tri-manganese core is highly robust and maintains its ensemble of oxidation states at $Mn^{III}Mn^{II}_2$. We suspect the cluster decomposition is due to hydrolysis by adventitious water during the shipping process.

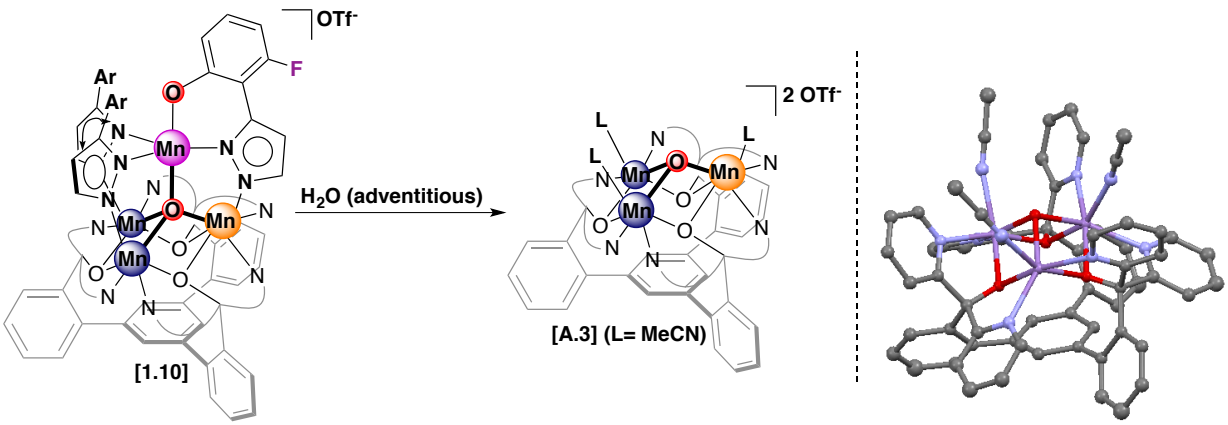


**Figure A.5.** Hydrolysis of **1.10** and accompanying solid-state structure. Counteranions, solvent, and hydrogen atoms are omitted.

**A.5 Attempted Synthesis and Characterization of a [$Mn_3Fe$] Heterometallic Cluster.**

Preliminary variable temperature $^1$H-NMR studies on **1.2** in the presence of excess sPhIO (5 equiv.) at -70 ºC in $CD_2Cl_2$ revealed paramagnetic species with a $^1$H-NMR distinct from **1.2** and **1.5**. Nonetheless, this species quickly decayed to **1.5** at -50 ºC. We envisioned the synthesis of the heterometallic cluster $[LMn_3(FArPz)_3OFe][OTf]_x$ (x = 1, 2) to differentiate the metal ions for X-ray absorption spectroscopy (XAS) studies and to contrast heterometallic reactivity with the homometallic tetra-iron and tetra-manganese analogs. The site-differentiated (apical) iron metal center allows for zero-field $^{57}$Fe Mössbauer spectroscopy to identify the coordination environment and electronic structure of temperature-sensitive intermediates. The ligand set 2-fluorophenyl pyrazolate (NaFArPz) was selected in which a putative metal-oxo would have access to oxygenate either C–H bonds or C–F bonds. Oxidative procedures with PhIO as the interstitial $\mu_4$-oxygen atom source were unsuccessful as assessed by $^1$H-NMR spectroscopy and ESI-MS. These procedures yielded intractable mixtures, often with silent $^1$H-NMR spectra. In a one-pot non-oxidation procedure, addition of $H_2O$ (1.0 equiv.) and $Fe(N(SiMe_3)_2)_2$ (1.0 equiv.) to a stirring solution of **1.1** and NaFArPz (3.2 equiv.) in THF afforded an insoluble green powder, postulated as $LMn_3(FPhPz)_3OFe$ (**A.4**). Treatment of **A.4** with AgOTf (1.0 equiv.) in MeCN resulted in a brown-green slurry. The $^1$H-NMR spectrum of an aliquot resembled that of **1.3**; however, ESI-MS analysis was consistent with $[LMn_3(FPhPz)_3OFe]^{1+}$ (m/z = 1576.1) and not $[LMn_3(FPhPz)_3OMn]^{1+}$ (m/z = 1575.2). These data supported the tentative assignment of this species as $[LMn_3(FPhPz)_3OFe][OTf]$ (**A.5**). Over several days, new paramagnetic peaks appeared in the $^1$H-NMR spectrum of **A.5**, even when stored in the solid state.

Zero-field $^{57}$Fe Mössbauer spectroscopy was employed to assess the dynamic $^1$H-NMR spectra for **A.5.** Mössbauer spectroscopy on **A.5** following AgOTf addition revealed a prominent

six-coordinate high-spin ferrous signal ($\delta$ = 0.469, $|\Delta E_Q|$ = 0.830, 94 %), consistent with a $Mn^{II}_2Fe^{III}$ heterometallic core and an apical $Mn^{II}$ ion. Mössbauer spectroscopy on crystals revealed three separate iron metal centers signals, consistent with Mn/Fe scrambling and internal electron transfer. We suspect the lower oxidation potential of $Fe^{II}$ compared to $Mn^{II}$ favors oxidation of $Fe^{II}$ to $Fe^{III}$, followed by Fe scrambling to the basal position to yield $[LMn_2Fe(PhPz)_3OMn][OTf]$ (**A.5'**), (Figure A.6). This kinetic product rearranges to the thermodynamically favored statistical distribution as electron transfer occurs between the different metal centers.

Treatment of **A.4** with AgOTf (2.1 equiv.) in acetonitrile results in a $^1$H-NMR spectrum identical to that of **1.2** and was speculated to be $[LMn_3(FPhPz)_3OFe][OTf]_2$ (**A.6**); nonetheless, additional paramagnetic peaks appeared during crystallization attempts. This result is suggestive of Fe/Mn scrambling. Due to the facile internal rearrangements of the $[Mn_3Fe]$ clusters, this project has been abandoned.

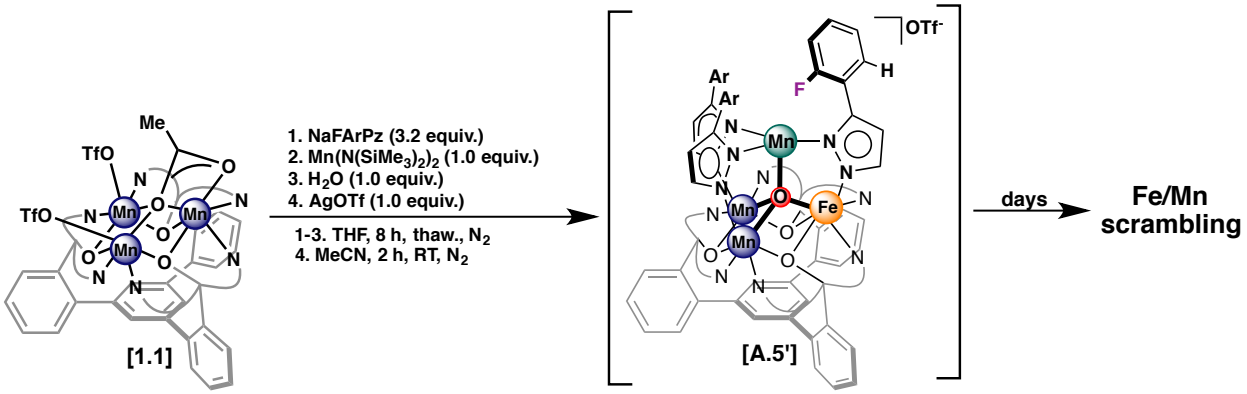


**Figure A.6**. Cluster decomposition and Mn/Fe scrambling for $[Fe_3Mn]$ heterometallic cluster.

**A.6. Competitive C–H versus C–F Activation for 2-fluorophenyl Pyrazolate Clusters.**

Because C–H (**1.2**, **1.3**) and C–F (**1.7**, **1.8**) oxygenation was observed upon exposure of the tetra-manganese clusters to oxygen-atom transfer reagents, we reasoned that cluster construction with 2-fluorophenyl pyrazolate (NaFArPz) would provide the putative manganese-oxo species access to both C–H and C–F bonds. Quantification of C–H and C–F oxygenation provides insight into the relative barriers of each process and supports a common intermediate – such as a high-valent manganese-oxo – if different oxygen-atom transfer reagents would yield identical product distributions. Similarly, if a difference in product distribution based on the oxidant source is observed, then an oxidant adduct may be responsible for reactivity. Homometallic tetra-manganese ($[LMn_3(FArPz)_3OMn][OTf]_x$; x = 1, 2) and tetra-iron ($[LFe_3(FArPz)_3OFe][OTf]_x$; x = 1, 2) complexes were envisioned. The isolation of a heterometallic $Mn_3Fe$ cluster was unsuccessful due to facile Mn/Fe scrambling (Appendix A.5).

Addition of NaFArPz (3.2 equiv.) and PhIO (1.1 equiv.) to **1.1** afforded a paramagnetic purple-brown species with ESI-MS consistent with *in situ* formation of $[LMn_3(FArPz)_3ONa][OTf]$ (**A.7**). Single crystals of **A.7** were grown by diethyl ether diffusion into a solution of **A.7** in $CH_2Cl_2$. XRD confirms the expected $Mn_3ONa$ core and one outer-sphere triflate counteranion (Figure A.7). Salt metathesis with $Mn(OTf)_2(MeCN)_2$ (2.0 equiv.) afforded $[LMn_3(FArPz)_3OMn][OTf]_2$ (**A.8**) with an identical $^1$H-NMR spectrum to that of **1.2**. One-electron reduction of **A.8** with $CoCp_2$ (1.1 equiv.) in $CH_2Cl_2$ afforded $[LMn_3(FArPz)_3OMn][OTf]_2$ (**A.9**) with a $^1$H-NMR spectrum identical to that of **1.3**. Complex **1.3** was characterized by XRD with bond parameters resembling those of **1.8**. Exposure of **A.8** and **A.9** to either iodosobenzene or $TBAIO_4$ affords both C–H and C–F oxygenations according

to ESI-MS. The presence of both species suggests the rate-determining step for C–H and C–F oxygenations to be similar in transition state barrier.

To quantify relative C–H to C–F activation, several different approaches have been explored. Unfortunately, phenolates HOArPzH (from C–F oxygenation) and HOFArPzH (from C–H oxygenation) co-elute under standard conditions in gas chromatography and liquid chromatography. Because HOFArPzH and FArPzH have different $^{19}$F peaks by $^{19}$F-NMR, an alternative method of quantification is to integrate the relative areas of these peaks. It must be assumed that the integration of FArPzH is twice the integration of the sum of HOFArPzH and HOArPzH. To facilitate quantification, the synthesis of a 2,4-difluorophenyl pyrazole ligand would allow quantification by integration of the *para*-fluorine signal by $^{19}$F-NMR; however, this ligand will greatly alter the solubility properties of the homometallic clusters.

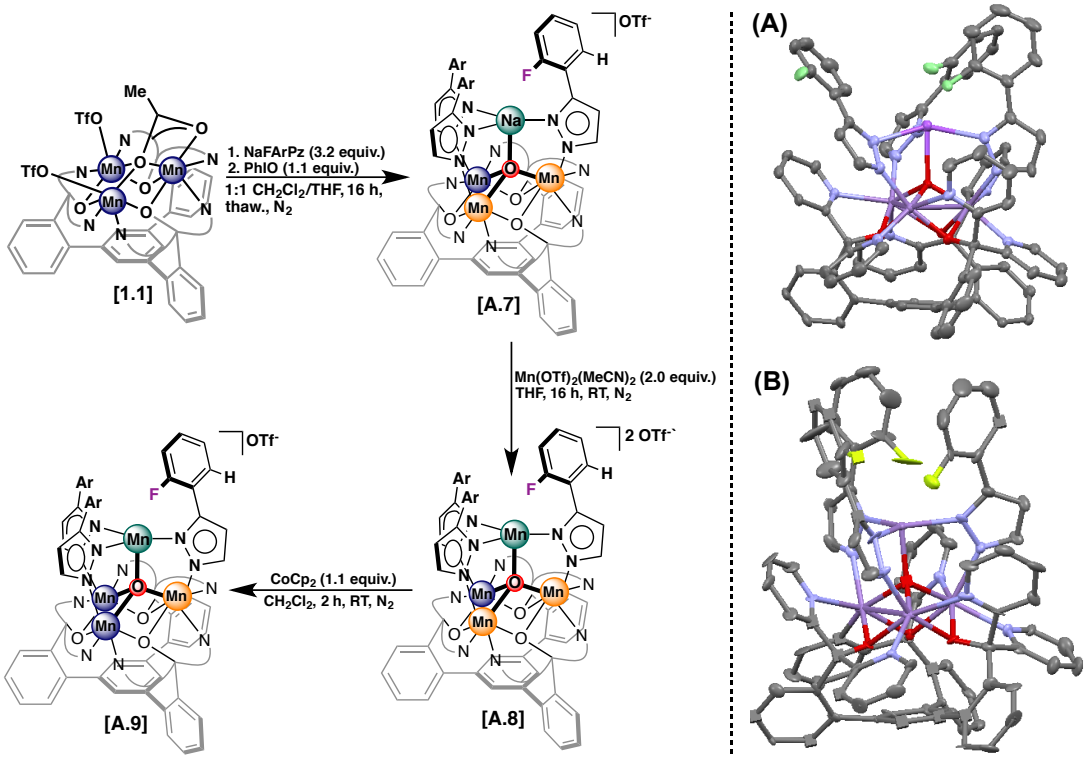


**Figure A.7**. Synthesis of complexes **A.7, A.8**, and **A.9** with crystal structures of **A.7** (A) and **A.9** (B). Both **A.7** and **A.9** are of publishable quality. Counteranions, solvent, and hydrogen atoms are omitted.

**A.7. Synthesis of [$LFe_3(FArPz)_3OFe$][OTf]**.

Toward quantifying relative C–H to C–F oxygenation by treatment of homometallic tetra-iron clusters with iodosobenzene, the complex [$LFe_3(FArPz)_3OFe$][OTf] (**A.10**) was synthesized from $LFe(OAc)(OTf)_2$ in route analogous to the synthesis of **A.9**. The $^1$H-NMR spectrum of **A.10** was identical to that of [$LFe_3(F_2ArPz)_3OFe$][OTf], and ESI-MS showed a single peak corresponding to the desired product. Single crystals suitable for XRD were obtained by diffusing diethyl ether into a concentrated solution of **A.10** in acetonitrile. The preliminary crystal structure, with a rhombohedral unit cell, revealed substantial electron density, likely corresponding to an extremely disordered second metal-containing cluster, which could not be adequately modeled. The data collection was prematurely killed.

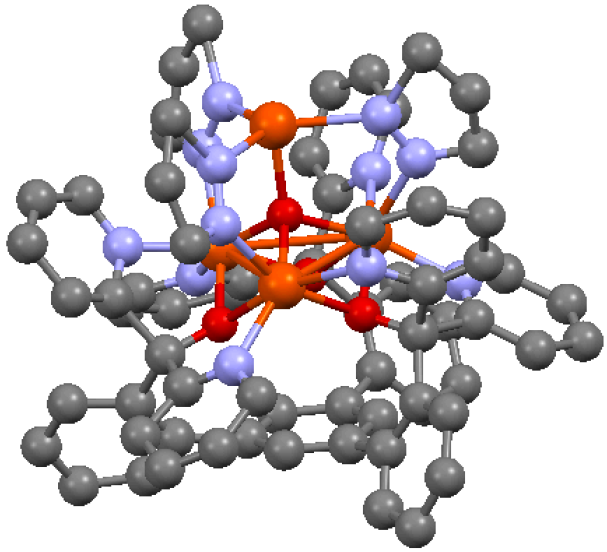

**Figure A.8**. Preliminary crystal structure of complex **A.10**. Counteranions, solvent, and hydrogen atoms are omitted. The fluorophenyl rings are omitted to due unresolved crystallographic disorder.

**A.8. Synthesis of $[LMn_3(F_2ArPz)_3OMnF][OTf]_2$.**

To confirm fluoride-transfer upon treatment of $[LMn_3(F_2ArPz)_3OMn][OTf]_2$ (**1.7**) with iodosobenzene, an independent synthesis was pursued. Exposure of **1.7** to $XeF_2$ (1.0 equiv.) in thawing MeCN afforded a purple solution, postulated to be $[LMn_3(F_2ArPz)_3OMnF][OTf]_2$ (**1.13**). Single crystals were grown by layering a solution of **1.13** with toluene; unfortunately, the crystals were of poor quality and very small. The preliminary XRD structure is consistent with the placement of the fluorine on the apical manganese. The unit cell of the crystal structure is rhombohedral in which a $C_3$ axis of symmetry overlaps the $Mn_{apical}$-F vector.

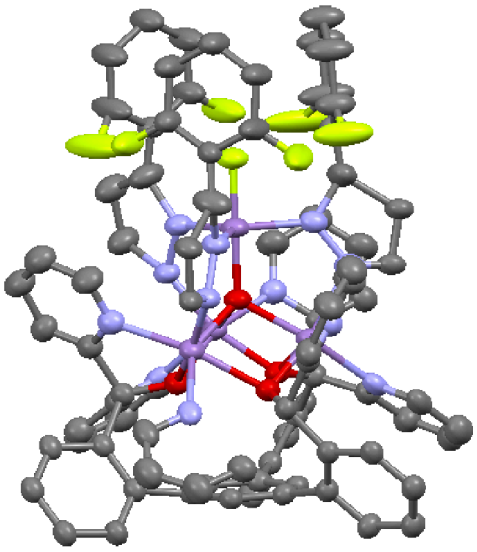

**Figure A.9**. Preliminary crystal structure of complex **1.13**. Counteranions, solvent, and hydrogen atoms are omitted.

**A.9. Decomposition of $[LMn_3(PhPz)_2(OArPz)OMn][BPh_4]$.**

Toward obtaining X-ray quality crystals of the C–H oxygenated products (**1.5** and **1.6**), counterion exchange was envisioned to change the solubility properties of the complex and potentially promote the formation of single crystals. Treatment of $[LMn_3(PhPz)_3OMn][BPh_4]$ with iodosobenzene afforded a $^1$H-NMR spectrum near-identical to **1.6**; however, features associated with $[LMn_3(PhPz)_3OMn][BPh_4]$ were still detectable by $^1$H-NMR spectroscopy. Allowing diethyl ether to diffuse into a concentrated solution of the crude mixture in MeCN afforded X-ray quality crystals. Although the preliminary X-ray structure showed the desired C–H oxygenated product, the oxygen atom bridging the apical manganese and phenyl ring exhibited partial occupancy. This result suggests co-crystallization of $[LMn_3(PhPz)_2(OArPz)OMn][BPh_4]$ with $[LMn_3(PhPz)_3OMn][BPh_4]$. Addition of excess iodosobenzene to $[LMn_3(PhPz)_3OMn][BPh_4]$ affords $[LMn_3(PhPz)_2(OArPz)OMn][BPh_4]$ without the presence of starting material; however, preliminary crystallization attempts have been so-far unsuccessful.

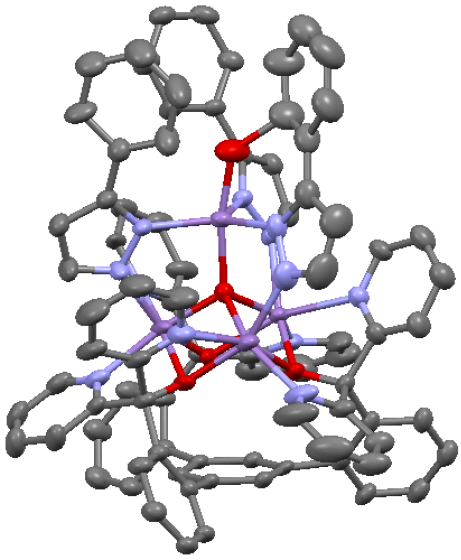

**Figure A.10**. Preliminary crystal structure of complex **1.6**. Tetraphenylborate counteranion, solvent, and hydrogen atoms are omitted.

**A.10. Crystal Structure of [LFe$_3$(PhPz)$_3$OMn][OTf].**

Toward understanding the influence of the tri-iron core on the apical manganese active site, [LFe$_3$(PhPz)$_3$OMn][OTf] was targeted by chemical reduction of [LFe$_3$(PhPz)$_3$OMn][OTf]$_2$. Addition of $CoCp_2$ (1.1 equiv.) affords a color change to red-purple upon addition with a $^1$H-NMR spectrum corresponding to a new paramagnetic species, assigned as [LFe$_3$(PhPz)$_3$OMn][OTf] (**2.2-Mn**). Large X-ray quality crystals were obtained by layering a solution of **2.2-Mn** in $CH_2Cl_2$ with toluene. The solid-state structure reveals four molecules of **2.2-Mn** in the asymmetric unit with four outer-sphere triflates. The tri-iron core in each cluster is consistent with a two long bonds and one short bond.

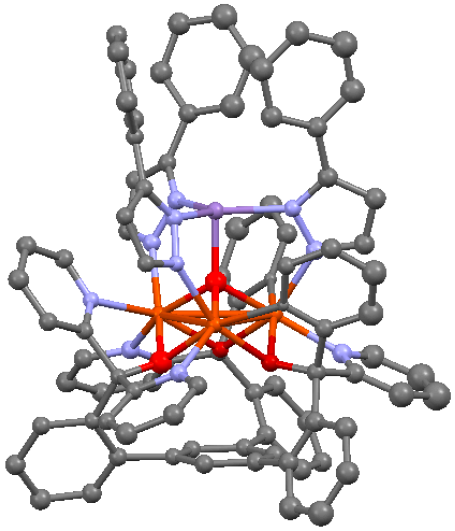

**Figure A.10**. Crystal structure of complex **2.2-Mn**. Triflate counteranions, solvent, and hydrogen atoms are omitted. Four molecules of **2.2-Mn** are present in the asymmetric unit.

**A.11. Decomposition of $[LFe_3(PhPz)_2(OPhPz)OMn][OTf]_3$.**

The $^1$H-NMR spectra from treatment of **2.4-Mn** with AgOTf (1.1 equiv.) in $CH_2Cl_2$ and treatment of **2.3-Mn** with sPhIO (1 equiv.) in $CH_2Cl_2$ produce the same $^1$H-NMR, suggesting both reactions to yield $[LFe_3(PhPz)_2(OArPz)OMn][OTf]_3$ (**2.6-Mn**). X-ray quality crystals were grown by diffusing diethyl ether into a concentrate solution of **2.6-Mn** in acetonitrile; XRD analysis of **2.6-Mn** revealed the desired complex with three outer-sphere triflate counteranions; however, preliminary $Fe_{core}$–O1 bond distances were consistent with a $Fe^{II}Fe^{III}_2$ tri-iron core, (Figure A.11). Neither the unit cell nor bond metrics were consistent with **2.4-Mn**. The $^1$H-NMR of the crystals is consistent with a mixture of **2.4-Mn** and **2.6-Mn**, suggestive of decomposition of **2.6-Mn** in solution to **2.4-Mn**. The data collection was stopped prematurely due to the inconsistent $Fe_{core}$-O1 bond parameters and number of outer-sphere triflates.

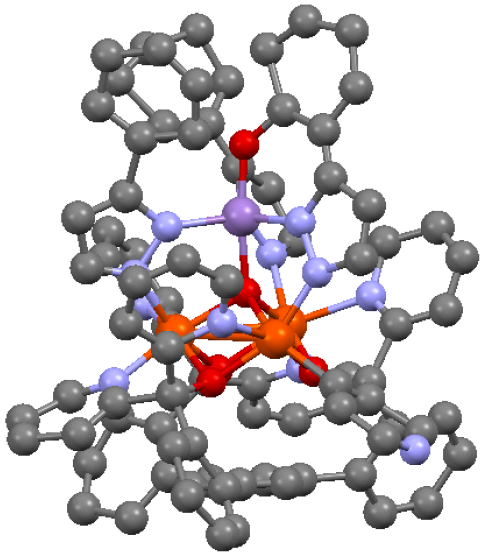

**Figure A.11**. Preliminary crystal structure of complex **2.6-Mn**. Counteranions, solvent, and hydrogen atoms are omitted.

**Supporting Information**

# Bio-Inspired Homometallic and Heterometallic Clusters Relevant to the Oxygen-Evolving Complex of Photosystem II

Kurtis M. Carsch, Graham de Ruiter, Theodor Agapie*

*Division of Chemistry and Chemical Engineering, California Institute of Technology, Pasadena, California 91125, United States.*

**Email: Agapie@caltech.edu*

## Table of Contents.

**General Considerations.** Unless otherwise specified, all operations were carried out in an MBraun drybox under a nitrogen atmosphere or using standard Schlenk techniques. Glassware was oven dried at 140 ºC for a minimum of 2 h prior to use and allowed to cool under vacuum. Solvents for air- and moisture-sensitive reactions were dried over sodium benzophenone ketyl, calcium hydride, or by the method of Grubbs.[53] Deuterated solvents were purchased from Cambridge Isotope Laboratories and vacuum transferred from sodium benzophenone ketyl. Solvents, once dried and degassed, were vacuum transferred directly prior to use or stored under inert atmosphere over 4 Å molecular sieves. Reagents phenyl-1H-pyrazole (PhPzH),[25] sodium 5-phenylpyrazolate (NaPhPz),[27] 2,6-difluorophenyl-1H-pyrazole ($F_2$ArPzH),[27] sodium 5-(2,6-difluoro)phenylpyrazolate (Na$F_2$ArPz),[27] sodium 2-(1*H*-pyrazol-5-yl)phenolate (NaOArPzH),[27] sodium 3-fluoro-2-(1*H*-pyrazol-5-yl)phenolate (NaOFArPzH),[27] iodosobenzene (PhIO),[54] 2-tert-butylsulfonyliodosylbenzene (sPhIO),[55] $Mn(N(SiMe_3)_2)_2$,[56] and $Mn(OTf)_2(MeCN)_2$[57] were prepared according to literature procedures. Caution! *Reagent PhIO is a potential explosive and should therefore be synthesized and stored in minimal quantities. Similarly, an explosion hazard for the synthesis of the oxygen-atom transfer reagent 2-tert-butylsulfonyliodosylbenzene (sPhIO) has been recorded.*[58,59] *An alternative procedure following Lin was implemented to maximize safety.*[55] Reagents 2-(1*H*-pyrazol-5-yl)phenol (HOArPzH), Na($N(SiMe_3)$), MeOTf, and AgOTf were

purchased from Sigma Aldrich and Strem Chemicals. Reagents cobaltocene ($Cp_2Co$) and decamethylcobaltocene ($Cp^*_2Co$) were purchased from Strem Chemicals and sublimed before use.
All commercially available pyrazoles were sublimed before use. Anhydrous tetrahydrofuran (THF) was purchased from Aldrich in 18 L Pure-Pac$^{TM}$ containers. Anhydrous $CH_2Cl_2$, diethyl ether, hexane and THF were purified by sparging with nitrogen for 15 minutes and then passing under nitrogen pressure through a column of activated A2 alumina. Anhydrous 1,2-dimethoxyethane (DME) was dried over sodium/benzophenone and vacuum-transferred onto molecular sieves. The $^1H$ and $^{19}F$ NMR spectra were recorded at 300.13 and 282.36 MHz, respectively, on a Varian 300 MHz spectrometer. All chemical shifts ($\delta$) are reported in ppm, and coupling constants ($J$) are in Hz. The $^1H$ NMR spectra were referenced using residual solvent peaks in the deuterated solvent. The $^{19}F$ chemical shifts are reported relative to the internal lock signal. Deuterated solvents ($CD_2Cl_2$ and $CD_3CN$) were purchased from Cambridge Isotope Laboratories, dried over calcium hydride, degassed by three freeze-pump-thaw cycles and vacuum-transferred prior to use. The UV-vis spectra were recorded on a Varian Cary Bio 50 spectrophotometer. Fast atom bombardment-mass spectrometry (FAB-MS) analysis was performed with a JEOL JMS-600H high-resolution mass spectrometer. Elemental analyses were performed at Caltech.

**Electrochemical measurements.** CVs were recorded with a Pine Instrument Company AFCBP1 bipotentiostat using the AfterMath software package. All measurements were performed in a three-electrode cell configuration that consisted of (1) a glassy-carbon (ø = 3.0 mm) working electrode, (2) a Pt wire as the counter electrode, and (3) an Ag wire as the reference electrode. All electrochemical measurements were performed at RT in an M. Braun $N_2$-filled glovebox with $O_2$ and $H_2O$ levels < 2 ppm. Dry dichloromethane or acetonitrile that contained 0.1 M $Bu_4NPF_6$ was used as the electrolyte solution. The ferrocene/ferrocenium ($Fc/Fc^{1+}$) redox couple was used as an internal standard for all measurements.

**Mössbauer spectroscopy**. Zero-field $^{57}Fe$ Mössbauer spectra were recorded at 80 K in the constant acceleration mode on a spectrometer from See Co (Edina, MN) equipped with an SVT-400 cryostat (Janis, Wilmington, WA). The quoted isomer shifts are relative to the centroid of the spectrum of a $\alpha$-Fe foil at room temperature. Samples were prepared by grinding polycrystalline material (20 mg) into a fine powder and pressed into a homogeneous pellet with boron nitride in a cup fitted with a screw cap. The data were fitted using the program WMOSS (www.wmoss.org). All spectra were simulated by three pairs of symmetric quadrupole doublets with equal populations and Lorentzian lineshapes, and refined to a minimum by the method of least squares optimization. For all spectra, the observed resonances spanned the region from -1–3 mm $s^{-1}$. Any resonances appearing above 2 mm $s^{-1}$ indicate the presence of high spin $Fe^{II}$ centers and must correspond to species with isomer shifts ~1 mm $s^{-1}$, given the range of observed

resonances. The Mössbauer data were modeled to be consistent with our previously reported triiron-oxo/hydroxyl clusters, and our previously reported tetranuclear iron clusters. Overall, the observed Mössbauer parameters are in-line with other six-coordinate $Fe^{II}/Fe^{III}$ centers bearing N- and O-donor atoms.

**X-ray crystallography.** Low temperature (100 K) X-ray data was obtained on a Bruker PHOTON100 CMOS based diffractometer (microfocus sealed X-ray tube, Mo Kα (λ) = 0.71073 Å or with Cu Kα (λ) = 1.54178). All diffractometer manipulations, including data collection, integration, and scaling were carried out using the Bruker APEXII software.[60] Absorption corrections were applied using SADABS.[61] Structures were solved by direct methods using XS[62] (incorporated into SHELXTL), and refined by full-matrix least squares on $F^2$. All non-hydrogen atoms were refined using anisotropic displacement parameters. Hydrogen atoms were placed in the idealized positions and refined using a riding model. The structures were refined (weighed least squares refinement on $F^2$) to convergence.

**Synthetic Procedures.**

**Chapter 1.**

**Synthesis of $LMn_3(OAc)(OTf)_2$ (1.1)**. In the glovebox, to a yellow slurry of $LMn_3(OAc)_3$ (480.0 mg, 0.401 mmol) in $CH_2Cl_2$ (10 mL) was added methyl triflate (MeOTf; 0.132 mL, 1.203 mmol). Over ten minutes, the mixture became an opaque off-white suspension. After stirring for thirty minutes, solvent and volatiles were removed under reduced pressure to yield an off-white powder. The solid was triturated in diethyl ether (10 mL) and collected on a medium porosity glass frit with additional diethyl ether washings (3 x 10 mL). Drying the off-white powder yielded **1.1** (540 mg, 98 %). $^1$H-NMR (300 MHz, $CD_3CN$): δ 63.9 (br), δ43.7 (br), δ 11.01 (br), δ -10.8 (br). $^{19}$F-NMR (282 MHz, $CD_2Cl_2$): δ-76.9 (br). UV-Vis ($CH_3CN$) [ε ($M^{-1}$ $cm^{-1}$)]: 254 nm (6.4 x $10^4$). Anal Calcd. for $C_{61}H_{42}F_6Mn_3N_6O_{11}S_2$ ($LMn_3(OAc)(OTf)_2$, **1.1**): C 53.17, H 3.07, N 6.10. Found: C 52.93, H 3.28, N 6.36.

**Synthesis of $LMn_3(PhPz)_3OMn][OTf]_2$ (1.2)**. In the glovebox, a suspension of **1.1** (550.0 mg, 0.401 mmol) in $CH_2Cl_2$ (5 mL) was frozen in a cold well. To this thawing suspension was added NaPhPz (220.0 mg, 1.323 mmol) as a homogeneous solution in THF (7 mL). The resulting suspension became homogeneous yellow-orange over the course of thirty minutes. After two hours, iodosobenzene (PhIO; 93.0 mg, 0.421 mmol) was added as a suspension in $CH_2Cl_2$ (2 mL), resulting in the formation of a purple slurry. After sixteen hours, solvent was removed under reduced pressure, and the solids were triturated in

diethyl ether (10 mL). The suspension was filtered on a celite pad on top a coarse porosity glasses frit, following by washings with benzene (5 mL), and diethyl ether (10 mL). The remaining purple-brown solid was collected using a minimal volume of $CH_2Cl_2$. Purple needles (500 mg) of the proposed $[LMn_3(F_2ArPz)_3ONa][OTf]$ were obtained by diffusing diethyl either into the concentration $CH_2Cl_2$ filtrate over several days. The crystals were dissolved in minimal THF (5 mL) to produce a purple-brown slurry, followed by addition of $Mn(OTf)_2(MeCN)_2$ (338.7 mg, 0.856 mmol). Over one hour, the solution turned brown-purple with visible precipitate. The mixture was allowed to stir for sixteen hours, followed by collection of the brown-purple solids on a celite pad on top a coarse porosity glass. The solids were washed with additional THF (*ca.* 10 mL) until the purple filtrate became near-colorless. The remaining brown-purple solid on the frit was collected with acetonitrile and dried under reduced pressure, yielding **1.2** (512.0 mg, 45 %). X-ray quality crystals of **1.2** were obtained by vapor diffusion of diethyl ether into a concentrated solution of **1.2** in acetonitrile over the course of one week. $^1$H-NMR (300 MHz, $CD_2Cl_2$): δ 50.0 (br), δ 35.2 (br), δ 31.2 (br), δ 13.3 (br), δ 10.61 (br), δ -12.4 (br), δ -19.0 (br). $^{19}$F-NMR (282 MHz, $CD_2Cl_2$): δ -78.6 (s). UV-Vis ($CH_2Cl_2$) [ε ($M^{-1}$ $cm^{-1}$)]: 253 nm (8.9 x $10^4$).

**Synthesis of $LMn_3(PhPz)_3OMn][OTf]_1$ (1.3)**. In the glovebox, to a stirring solution of **1.2** (100.0 mg, 55.0 μmol) in $CH_2Cl_2$ (4 mL) was added cobaltocene ($Cp_2Co$, 10.9 mg, 58.0 μmol), accompanied by a color change upon addition from brown-purple to red-purple. After two hours, solvent was removed under reduced pressure. The solid was stirred as a purple suspension in dimethoxyethane (DME; 8 mL) and filtered over a celite pad on top a coarse porosity glass frit to remove cobaltocenium triflate. The remaining purple solid was collected in $CH_2Cl_2$ (2 mL) and dried under reduced pressure to yield **1.3** (74.0 mg, 81 % yield) X-ray quality crystals of **1.3** were obtained by vapor diffusion of diethyl ether into a solution of **1.3** in acetonitrile. $^1$H-NMR (300 MHz, $CD_2Cl_2$): δ 39.9 (br), δ 36.6 (br), δ 31.1 (br), δ 11.7 (br), δ -7.5 (br), δ -8.9 (br). $^{19}$F-NMR (282 MHz, $CD_2Cl_2$): - δ 78.8 (s). UV-Vis ($CH_2Cl_2$) [ε ($M^{-1}$ $cm^{-1}$)]: 256 nm (9.9 x $10^4$), 371 nm (2.8 x $10^3$). Anal Calcd. for $C_{85}H_{60}F_3Mn_4N_{12}O_7S$ ($[LMn_3(PhPz)_3OMn][OTf]_1$, **1.3**): C 61.12, H 3.62, N 10.06. Found: C 61.36, H 3.76, N 9.87.

**Synthesis of $LMn_3(PhPz)_3OMn$ (1.4)**.

***Procedure A.*** In the glovebox, to a stirring solution of **1.2** (37.0 mg, 20.4 μmol) in MeCN (4 mL) was added reagent decamethylcobaltocene ($CoCp^*_2$; 13.7 mg, 41.7 μmol), resulting in the precipitation of a yellow solid upon addition. After two hours, the mother liquor was decanted, and the yellow solid – speculated to be **1.4** – was dried under reduced pressure (11.4 mg, 40 %). UV-Vis could not be performed on **1.4** due to its insolubility. A satisfactory elemental analysis could not be obtained for **1.4**.

***Procedure B.*** In the glovebox, a 500 mL Schlenk tube was charged with **1.1** (3.00 g, 0.02 mmol) and THF (50 mL) to yield an off-white slurry. The Schlenk tube was placed in a cold well and frozen. To this thawing slurry was added NaPhPz (1.16 g, 0.007 mmol) in THF (50 mL), resulting in the formation of a homogeneous red-orange solution after thirty-minutes. After one hour, the mixture became a thick yellow slurry. To this suspension was added $Mn(N(SiMe)_3)_2$ (0.86 g, 0.002 mmol) in THF (10 mL), accompanied by a consistency and color change to homogeneous red-purple. After ten minutes, the Schlenk tube was exported from the drybox and imported into a nitrogen-filled wetbox. To this vigorously stirring solution was added water (39 μL, 0.002 mmol), resulting in precipitation of a pink-yellow solid upon addition. The mixture was stirred for an additional four hours. The Shlenk tube was subject to reduced pressure at 40 ºC for 48 hours to remove solvent and volatiles. The Schlenk tube was re-imported into the drybox. The solids were loaded onto a medium porosity glass frit and washed with hexanes (*ca.* 30 mL), THF (*ca.* 100 mL), and MeCN (*ca.* 100 mL) until the filtrate ran colorless with each solvent. The cherry red filtrate was discarded, and the insoluble yellow solids were collected and dried under reduced pressure to yield **1.4** (2.3 g, 70 % yield).

**Synthesis of $[LMn_3(PhPz)_2(OArPz)OMn][OTf]_2$ (1.5).**

***Procedure A***. In the glovebox, to a stirring solution of **1.2** (320.0 mg, 0.180 mmol) in $CH_2Cl_2$ (20 mL) was added PhIO (40.3 mg, 0.18 mmol) as a suspension in $CH_2Cl_2$ (5 mL). The darkening of the brown-purple slurry to off-black was accompanied by the disappearance of precipitate. After sixteen hours, solvent was removed under reduced pressure to yield an off-black solid. The solid was triturated in benzene (10 mL) and filtered over a glass frit to remove iodobenzene. The remaining solid was dissolved in $CH_2Cl_2$ (8 mL) and dried under reduced pressure to yield **1.5** (310 mg, 96 %). $^1$H-NMR (300 MHz, $CD_2Cl_2$): δ 82.0 (br), δ 77.6 (br), δ 73.1 (br), δ 70.5 (br), δ 68.0 (br), δ 64.5 (br), δ 58.7 (br), δ 55.7 (br), δ 51.4 (br), δ 48.7 (br), δ 46.9 (br), δ 41.8 (br), δ 38.6 (br), δ 36.1 (br), δ 33.8 (br), δ 24.9 (br), δ 16.6 (br), δ 14.9 (br), δ 13.8 (br), δ 13.1 (br), δ 10.66 (br), δ -2.1 (br), δ -3.5 (br), δ -4.5 (br), δ -10.1 (br), δ -11.0 (br), δ -12.8 (br), δ -14.4 (br), δ -17.2 (br), δ -19.4 (br), δ -20.7 (br), δ -21.9 (br), δ -24.3 (br), δ -29.3 (br), δ -30.2 (br). $^{19}$F-NMR (282 MHz, $CD_2Cl_2$): - δ 78.8 (s).

***Procedure B.*** In the glovebox, to a stirring solution of **1.6** (40.0 mg, 23.7 μmol) in $CH_2Cl_2$ (2 mL) was dropwise added silver triflate (AgOTf; 6.4 mg, 24.9 μmol) as a suspension in $CH_2Cl_2$ (2 mL). The solution darkened to off-black over the course of ten minutes. After two hours, the solution was filtered over a glass frit to remove metallic silver. Solvent was removed under reduced pressure to yield **1.5** as an off-black powder 39.8 mg, 90 %). The $^1$H-NMR spectrum is identical to that from *Procedure A*.

**Synthesis of $[LMn_3(PhPz)_2(OArPz)OMn][OTf]_1$ (1.6).**

***Procedure A*.** In the glovebox, to a stirring solution of **1.3** (40.0 mg, 23.9 μmol) in $CH_2Cl_2$ (2 mL) was added PhIO (5.5 mg, 25.1 μmol) as a suspension in $CH_2Cl_2$ (2 mL). Over the course of one hour, the darkening of the red-purple slurry to dark brown was accompanied by the disappearance of precipitate. After sixteen hours, solvent was removed under reduced pressure to yield a dark brown solid. The solid was triturated in benzene (3 mL) and filtered over a glass frit. The remaining solid was dissolved in $CH_2Cl_2$ (2 mL) and dried under reduced pressure to yield **1.6** (36.5 mg, 92 %). $^1$H-NMR (300 MHz, $CD_2Cl_2$): δ 56.6 (br), δ 55.2 (br), δ 52.5 (br), δ 49.4 (br), δ 47.0 (br), δ 42.9 (br), δ 38.1 (br), δ 36.2 (br), δ 34.5 (br), δ 30.0 (br), δ 27.8 (br), δ 22.8 (br), δ 13.5 (br), δ 13.2 (br), δ 12.3 (br), δ 10.55 (br), δ -1.11 (br), δ -1.79 (br), δ -2.63 (br), δ -4.0 (br), δ -10.7 (br), δ -12.8 (br), δ -13.8 (br), δ -15.6 (br), δ -16.9 (br), δ -17.9 (br), δ -26.7 (br). $^{19}$F-NMR (282 MHz, $CD_2Cl_2$): - δ 78.8 (s).

***Procedure B*.** In the glovebox, to a stirring solution of **1.2** (40.0 mg, 22.0 μmol) in $CH_2Cl_2$ (2 mL) was added NaOArPzH (4.4 mg, 24.2 μmol) in $CH_2Cl_2$ (2 mL). After thirty minutes, the reaction mixture darkened to off-black. After sixteen hours, the solvent was removed under reduced pressure and rinsed over a glass frit with benzene (10 mL) and diethyl ether (5 mL). The remaining off-black solid was dissolved in $CH_2Cl_2$ (5 mL) and dried under reduced pressure to yield **1.6** (23.7 mg, 85 %). The $^1$H-NMR spectrum was identical to that of *Procedure A*.

**Synthesis of $[LMn_3(F_2ArPz)_3OMn][OTf]_2$ (1.7).**

In the glovebox, a suspension of **1.1** (100.0 mg, 0.073 mmol) in $CH_2Cl_2$ (5 mL) was frozen in a cold well. To this thawing suspension was added $NaF_2ArPz$ (220.0 mg, 1.323 mmol) as a homogeneous solution in THF (7 mL). The resulting suspension became homogeneous yellow-orange over the course of thirty minutes. After two hours, PhIO (16.8 mg, 0.076 mmol) was added as a suspension in $CH_2Cl_2$ (2 mL) to the existing mixture, resulting in the formation of a purple-brown slurry. After sixteen hours, solvent was removed under reduced pressure, and the solids were subsequently triturated in diethyl ether (15 mL). The suspension was filtered on a celite pad on top a coarse porosity glass frit, following by washings with benzene (20 mL), and diethyl ether (10 mL). The yellow filtrate was discarded. The remaining purple-brown solid was collected using a minimal volume of $CH_2Cl_2$. Purple needles 50 mg) of the proposed $[LMn_3(F_2ArPz)_3ONa][OTf]$ were obtained by allowing diethyl either to diffuse into the concentration $CH_2Cl_2$ filtrate over two days. The crystals were dissolved in minimal THF (5 mL) to produce a purple-brown slurry, followed by addition of $Mn(OTf)_2(MeCN)_2$ (60 mg, 0.057 mmol). Over one hour, the solution turned brown-violet with visible precipitate. The mixture was allowed to stir for sixteen hours, followed by removal of solvent under reduced pressure. X-ray quality crystals of **1.7** were obtained by

vapor diffusion of diethyl ether into a concentrated solution of **1.7** in acetonitrile over the course of one week (60 mg, 45 %). $^{1}$H-NMR (300 MHz, $CD_2Cl_2$): δ 51.1 (br), δ 35.1 (br), δ 31.2 (br), δ 14.1 (br), δ 10.7 (br), δ 8.4 (br), δ -11.9 (br), δ -19.6 (br). $^{19}$F-NMR (282 MHz, $CD_2Cl_2$): - δ 78.8 (s). UV-Vis ($CH_2Cl_2$) [ε ($M^{-1}$ $cm^{-1}$)]: 249 nm (9.9 x $10^4$), 324 nm (4.5 x $10^3$). Anal Calcd. for $C_{86}H_{54}F_{12}Mn_4N_{12}O_{10}S_2$ [$LMn_3(F_2ArPz)_3OMn$][OTf]$_2$, **1.7**): C 53.60, H 2.82, N 8.72. Found: C 53.90, H 2.04, N 8.57.

**Synthesis of [$LMn_3(F_2ArPz)_3OMn$][OTf]$_1$ (1.8).** In the glovebox, to a stirring solution of **1.7** (55.0 mg, 0.029 mmol) in THF (3 mL) was added $CoCp_2$ (5.7 mg, 0.030 mmol). A color change from brown-violet to red-purple occurred upon addition. After two hours, solvent was removed under reduced pressure. The solid was stirred as a violet suspension in DME (3 mL) and filtered over a celite pad on top a coarse porosity glass frit to remove cobaltocenium triflate. The remaining purple solid was collected in $CH_2Cl_2$ (2 mL) and dried under reduced pressure to yield **1.8** (30 mg, 60 % yield) X-ray quality crystals of **1.8** were obtained by vapor diffusion of diethyl ether into a solution of **1.8** in $CH_2Cl_2$. $^{1}$H-NMR (300 MHz, $CD_2Cl_2$): δ 40.1 (br), δ 37.0 (br), δ 31.1 (br), δ 11.66 (br), δ 9.9 (br), δ -8.8 (br). $^{19}$F-NMR (282 MHz, $CD_2Cl_2$): - δ 78.8 (s). UV-Vis ($CH_2Cl_2$) [ε ($M^{-1}$ $cm^{-1}$)]: 249 nm (9.9 x $10^4$), 324 nm (4.5 x $10^3$). UV-Vis ($CH_2Cl_2$) [ε ($M^{-1}$ $cm^{-1}$)]: 253 nm (7.6 x $10^4$), 380 nm (2.9 x $10^3$). Anal Calcd. for $C_{85}H_{60}F_3Mn_4N_{12}O_7S$ ([$LMn_3(F_2ArPz)_3OMn$][OTf]$_1$, **1.8**): C 57.41, H 3.06, N 9.45. Found: C 56.01, H 3.09, N 8.97.

**Synthesis of $LMn_3(F_2ArPz)_3OMn$ (1.9).**

***Procedure A.*** In the glovebox, to a stirring solution of **1.7** (55.0 mg, 0.029 mmol) in MeCN (4 mL) was added $Cp^*_2Co$ (20.1 mg, 0.061 mmol), resulting in the precipitation of an orange-yellow solid upon addition. After two hours, the mother liquor was decanted, and the orange-yellow solid – speculated to be **1.9** – was dried under reduced pressure (36 mg, 80 %). UV-Vis could not be performed on **1.9** due to its insolubility. A satisfactory elemental analysis for **1.9** could not be obtained.

***Procedure B.*** In the glovebox, a 100 mL Schlenk tube was charged with **1.1** (400 mg, 0.290 mmol) and THF (20 mL) to yield an off-white slurry. The Schlenk tube was placed in a cold well and frozen. To this thawing slurry was added $NaF_2ArPz$ (187.8 mg, 0.929 mmol) in THF (20 mL), resulting in the formation of a homogeneous cherry red solution after thirty minutes. After one hour, the mixture became a thick orange-yellow slurry. To this suspension was added $Mn(N(SiMe)_3)_2$ (114.5 mg, 0.304 mmol) in THF (5 mL), accompanied by a consistency and color change to homogeneous red-violet. After ten minutes, the Schlenk tube was exported from the drybox and imported into a nitrogen-filled wetbox. To this vigorously stirring solution was added water (5.3 μL, 0.290 mmol), resulting in precipitation of a pink-yellow solid upon addition. The mixture was stirred for an additional four hours. The Shlenk tube was

subject to reduced pressure at 35 ºC for 48 hours to remove solvent and volatiles. The Schlenk tube was re-imported into the drybox. The solids were loaded onto a medium porosity glass frit and washed with copious quantities of hexanes (ca. 10 mL), THF (ca. 40 mL), and MeCN (ca. 40 mL) until the filtrate ran colorless with each solvent. The cherry red filtrate was discarded, and the insoluble orange-yellow solids were collected and dried under reduced pressure to yield **1.9** (200 mg, 42 % yield).

**Synthesis of $[LMn_3(F_2PhPz)_2(OFArPz)OMn][OTf]_1$ (1.10).**

***Procedure A***. In the glovebox, a solution of **1.7** (40.0 mg, 0.021 mmol) in $CH_2Cl_2$ (2 mL) was frozen in the cold well. To this thawing solution was added NaOFArPzH (4.6 mg, 0.022 mmol) as an off-white suspension in $CH_2Cl_2$ (2 mL), accompanied by a color change from red-purple to off-black. After sixteen hours, the solvent was removed under reduced pressure. The solid was loaded onto a glass frit and washed with benzene (*ca.* 3 mL). The off-black solid was filtered in $CH_2Cl_2$ and dried under reduced pressure to yield **1.10** (32.0 mg, 80 %). $^1$H-NMR (300 MHz, $CD_2Cl_2$): δ 59.6 (br), δ 54.1 (br), δ 50.9 (br), δ 46.7 (br), δ 44.0 (br), δ 41.9 (br), δ 39.4 (br), δ 35.2 (br), δ 30.6 (br), δ 29.3 (br), δ 13.3 (s), δ 10.8 (s), δ 2.0 (s), δ 1.3 (s), δ 0.9 (s), δ -0.6 (s), δ -8.5 (br), δ -9.6 (br), δ -10.8 (br), δ -11.2 (br), δ -12.2 (br), δ -13.4 (br), δ -14.0 (br), δ -14.8 (br), δ -16.4 (br), δ -24.2 (br). $^{19}$F-NMR (282 MHz, $CD_2Cl_2$): δ -75.7 (s).

**Synthesis of $[LMn_3(F_2PhPz)_2(OFArPz)OMn][BF_4]_1$ (1.10').**

In the glovebox, to a suspension of **1.7** (100 mg, 0.061 mmol) in MeCN (3 mL) was added $AgBF_4$ (12.2 mg, 0.063 mmol) in MeCN (1 mL). After one hour, the suspension changed color from orange to purple-gray, accompanied by the formation of metallic silver. The mixture was stirred for an additional two hours, followed by removal of solvent under reduced pressure. The results solid was stirred in DME (10 mL) to yield a purple suspension. The suspension was filtered over a pad of celite on top a coarse porosity glass frit. The purple solid was washed with DME (ca. 20 mL) until the filtrate ran colorless. The red-brown filtrate was discarded, and the purple brown solid was dissolved in $CH_2Cl_2$, filtered, and dried under reduced pressure to yield 70 mg of purple-brown presumed **$[LMn_3(F_2ArPz)_3OMn][BF_4]_1$** (**1.8'**) with an identical $^1$H-NMR spectrum to that of **1.8**. $^{19}$F-NMR (282 MHz, $CD_2Cl_2$): δ -153.1 (s). To **1.8'** was added MeCN (5 mL) to yield a purple slurry. The slurry was subsequently frozen in the cold well, followed by addition of NaOFArPzH (9.0 mg, 0.045 mmol) in MeCN. The slurry was allowed to thaw and stir at room temperature for 48 hours, accompanied by no color change. To this suspension was added $AgBF_4$ (8.1 mg, 0.042 mmol) in MeCN (2 mL) dropwise, accompanied by a color change to brown. The solvent was removed under reduced pressure, and the solid was subsequently loaded on a glass frit and washed with benzene (*ca*. 3 mL) until the filtrate ran colorless. The solid was dissolved in $CH_2Cl_2$, filtered, and dried under reduced pressure to yield **1.10**' (30.0 mg, 28.6 %). X-ray quality crystals were

obtained by diffusing diethyl ether into a concentrated solution of **1.10'** in acetonitrile. The $^{1}$H-NMR spectrum is identical to that of **1.10**. $^{19}$F-NMR (282 MHz, $CD_2Cl_2$): δ -153.1 (s).

***Procedure B.*** In the glovebox, to a stirring solution of **1.8** (20.0 mg, 0.011 mmol) in $CH_2Cl_2$ (2 mL) was added PhIO (2.5 mg, 0.011 mmol) as a suspension in $CH_2Cl_2$ (2 mL). The gradual darkening to off-black over one hour accompanied the disappearance of heterogeneous material. The reaction was allowed to stir for sixteen hours with no additional color change. Solvent was removed under reduced pressure to yield an intense dark-brown powder. The powder was triturated in benzene (2 mL), collected on top a glass frit, followed by washing with additional benzene (*ca.* 2mL). The remaining solid was dissolved in $CH_2Cl_2$, filtered, and dried under reduced pressure to yield both **1.10** and **1.11**. $^{1}$H-NMR (300 MHz, $CD_2Cl_2$): δ 78.1 (br), δ 74.4 (br), δ 71.9 (br), δ 69.9 (br), δ 68.0 (br), δ 64.1 (br), δ 54.9 (br), δ 46.7 (br), δ 44.2 (br), δ 41.8 (br), δ 33.0 (br), δ 22.3 (br), δ 13.5 (s), δ 11.7 (s), δ -4.2 (s), δ -6.4 (s), δ -11.4 (s), δ -13.6 (s), δ -18.8 – -23.3 (br), δ 27.2 (br), -33.9 (s), -38.3 (s), δ -50.0 (br), δ -54.5 (br), δ -62.8 (br). $^{19}$F-NMR (282 MHz, $CD_2Cl_2$): δ -75.7 (s). The $^{1}$H-NMR is consistent with both **1.12** and **1.13**.

**Synthesis of $[LMn_3(F_2PhPz)_3OMnF][OTf]_1$ (1.11).** In the glovebox, a solution of **1.8** (20.0 mg, 0.011 mmol) in MeCN (2 mL) was frozen in the cold well. To this thawing solution was added $XeF_2$ (1.9 mg, 0.011 mmol) in MeCN 2 mL), resulting in a color change to violet-purple upon addition. After two hours, solvent and volatiles were removed under reduced pressure to yield **1.11** as a violet-purple solid (18.9 mg, 85 %). $^{1}$H-NMR (300 MHz, $CD_2Cl_2$): δ 76.2 (br), δ 68.5 (br), δ 57.3 (br), δ 54.4 (br), δ 49.2 (br), δ 45.4 (br), δ 43.3 (br), δ 41.1 (br), δ 38.1 (br), δ 35.6 (br), δ 33.9 (br), δ 31.1 (br), δ 25.0 (br), δ 16.5 (s), δ 13.6 (br), δ 1.2 (s), -4.8 (br), δ -7.9 – -16.2 (br), δ -18.6 (br), δ -24.5 (br), δ -35.5 (br). $^{19}$F-NMR (282 MHz, $CD_2Cl_2$): δ -78.8 (s). UV-Vis ($CH_2Cl_2$) [ε ($M^{-1}$ $cm^{-1}$)]: 252 nm (7.3 x $10^4$), 379 nm (2.0 x $10^3$), 534 nm (1.2 x $10^3$).

**Synthesis of $[LMn_3(F_2ArPz)_2(OFArPz)OMn][OTf]_2$ (1.12).**

***Procedure A.*** In the glovebox, to a stirring solution of **1.12** (100.0 mg, 0.056 mmol) in $CH_2Cl_2$ (3 mL) was added AgOTf (15.1 mg, 0.059 mmol) as a suspension in $CH_2Cl_2$ (3 mL), accompanied by a minor darkening of solution to an intense off-black powder. The reaction was allowed to stir for two hours, followed by filtering over a glass frit. Solvent was removed under reduced pressure to yield an off-black powder (102.0 mg, 95 %). $^{1}$H-NMR (300 MHz, $CD_2Cl_2$): δ 77.5 (br), δ 71.5 (br), δ 68.1 (br), δ 55.4 (br), δ 50.5 (br), δ 47.1 (br), δ 44.6 (br), δ 39.5 (br), δ 35.8 (br), δ 21.8 (br), δ 18.2 (br), δ 17.0 (s), δ 15.0 (s), δ 12.6 (br), δ 11.2 (br), δ -1.2 (s), δ -9.7 (br), δ -10.4 (s), δ -12.6 (br), δ -13.8 (br), δ -15.8 (br), δ -16.6 (br),

δ -18.1 (br), δ -19.2 (s), δ -21.3 (br), δ -23.6 (br), δ -28.7 (br), δ -30.5 (br), δ -31.7 (br), δ -46.7 (br). $^{19}$F-NMR (282 MHz, $CD_2Cl_2$): - δ 78.8 (s).

***Procedure B*.** In the glovebox, to a stirring solution of **1.7** (25.0 mg, 0.013 mmol) in $CH_2Cl_2$ (3 mL) was added PhIO (3.0 mg, 0.014 μmol) as a suspension in $CH_2Cl_2$ (2 mL). The gradual darkening to off-black over one hour accompanied the disappearance of heterogeneous material. The reaction was allowed to stir for sixteen hours with no additional color change. Solvent was removed under reduced pressure to yield an off-black powder. The powder was triturated in benzene (2 mL), collected on top a glass frit, followed by washing with additional benzene (*ca.* 2mL). The remaining solid was dissolved in $CH_2Cl_2$, filtered, and dried under reduced pressure to yield both **1.12** and **1.13**. $^1$H-NMR (300 MHz, $CD_2Cl_2$): δ 78.1 (br), δ 74.4 (br), δ 71.9 (br), δ 69.9 (br), δ 68.0 (br), δ 64.1 (br), δ 54.9 (br), δ 46.7 (br), δ 44.2 (br), δ 41.8 (br), δ 33.0 (br), δ 22.3 (br), δ 13.5 (s), δ 11.7 (s), δ -4.2 (s), δ -6.4 (s), δ -11.4 (s), δ -13.6 (s), δ -18.8 – -23.3 (br), δ 27.2 (br), -33.9 (s), -38.3 (s), δ -50.0 (br), δ -54.5 (br), δ -62.8 (br). $^{19}$F-NMR (282 MHz, $CD_2Cl_2$): δ -75.7 (s).

**Synthesis of $[LMn_3(F_2ArPz)_3OMnF][OTf]_2$ (1.13).** In the glovebox, a solution of **1.7** (40.0 mg, 0.021 mmol) in MeCN (2 mL) was frozen in the cold well. To this thawing solution was added $XeF_2$ (3.6 mg, 0.021 mmol) in MeCN 2 mL), resulting in a color change to purple upon addition. After two hours, solvent and volatiles were removed under reduced pressure to yield **1.13** as a purple solid (22.7 mg, 75 %). X-ray quality crystals were obtained by layering a solution of **1.13** in $CH_2Cl_2$ with toluene. $^1$H-NMR (300 MHz, $CD_2Cl_2$): δ 75.6 (br), δ 71.6 (br), δ 67.7 (br), δ 49.9 (br), δ 48.0 (br), δ 45.3 (br), δ 35.5 (br), δ 16.9 (br), δ 15.1 (br), δ 11.4 (br), δ 10.0 (br), δ -0.9 (br), δ -7.1 (br), δ -10.0 (br), δ -17.7 (br), δ -23.8 (br), δ -30.6 (br), δ -41.7 (br), δ -59.7 (br), δ -67.9 (br).$^{19}$F-NMR (282 MHz, $CD_2Cl_2$): δ -75.5 (s), δ -101.0 (br). $^{19}$F-NMR (282 MHz, $CD_2Cl_2$): δ -75.7 (s). UV-Vis ($CH_2Cl_2$) [ε ($M^{-1}$ $cm^{-1}$)]: 251 nm (5.7 x $10^4$), 531 nm (1.2 x $10^3$).

**Chapter 2.**

**Synthesis of $[LFe_3(PhPz)_3OMn][OTf]_2$ (2.1-Mn).** In the glovebox, a suspension of $LFe_3(OAc)(OTf)_2$ (2.2 g, 0.002 mol) in THF (30 mL) was frozen in the cold well. To this thawing suspension was added NaPhPz (847 mg, 0.006 mol) in THF (30 mL), resulting in a color and consistency change to a homogeneous orange solution. After two hours, PhIO (368 mg, 0.002 mmol) was added as a suspension in THF, resulting in a brown precipitate over one hour. After two hours, the brown precipitate was collected on a coarse frit and washed with a copious volume of THF (*ca*. 20 mL) until the filtrate ran faint

orange. To a suspension of the brown solid (761 mg, 0.469 mmol) in THF (20 mL) was added $Mn(OTf)_2(MeCN)_2$ (410 mg, 0.939 mmol). The suspension turned brown-red and became a thick slurry after two hours. After sixteen hours, the slurry was filtered over a thick bed of celite (0.5 cm) on top a coarse porosity glass frit. The remaining brown solid was dissolved in acetonitrile and filtered, followed by solvent removal under reduced pressure to yield **2.1-Mn** as a brown-orange solid (600 mg, 20 %). $^1$H-NMR (300 MHz, $CD_2Cl_2$): δ 120.0 (br), δ 77.8 (br), δ 72.5 (s), δ 70.3 (s), δ 54.1 (s), δ 51.6 (s), δ 44.7 (s), δ 15.3 (s), δ 13.4 (s), δ 9.5 (s), δ 8.2 (s), δ 5.3 (s), δ 4.7 (s), δ 3.2 (s), δ 2.8 (br), δ 1.6 (s), δ 1.2 (s), δ -2.5 (br). $^{19}$F-NMR (282 MHz, $CD_2Cl_2$): δ -77.8 (s). Anal. calcd. (%) for $C_{86}H_{60}F_6Fe_3MnN_{12}O_{10}S_2$: C 56.69, H 3.32, N 9.22; found: C 56.67, H 3.38, N 9.46.

**Synthesis of $[LFe_3(PhPz)_3OMn][OTf]_1$ (2.2-Mn).** In the glovebox, to a stirring solution of **2.1-Mn** (25.0 mg, 0.014 mmol) in $CH_2Cl_2$ (3 mL) was added dropwise a solution of $Cp_2Co$ (2.8 mg, 0.018 mmol) in $CH_2Cl_2$ (1 mL), accompanied by a color change to red-purple upon addition. After two hours, solvent was removed under reduced pressure. The solid was stirred as a purple suspension in DME (3 mL) and filtered over a celite pad on top a coarse porosity glass frit to remove cobaltocenium triflate. The remaining purple solid was collected in $CH_2Cl_2$ (2 mL) and dried under reduced pressure to yield **2.2-Mn** (7.0 mg, 31 % yield) X-ray quality crystals of **2.2-Mn** were obtained by layering a solution of **2.2-Mn** in $CH_2Cl_2$ with toluene.

**Synthesis of $[LFe_3(PhPz)_3OMn][OTf]_3$ (2.3-Mn).** In the glovebox, to a stirring solution of **2.1-Mn** (60.0 mg, 0.032 mmol) in $CH_2Cl_2$ (3 mL) was added dropwise a suspension of AgOTf (8.6 mg, 0.034 mmol) in $CH_2Cl_2$ (3 mL), accompanied by a color change to intense violet upon addition. After two hours, the reaction was filtered over a glass frit, and the filtrate was pumped down to yield **2.3-Mn** as a purple solid in quantitative yield. X-ray quality crystals of **2.3-Mn** were obtained by diffusing diethyl ether into a solution of **2.3-Mn** in acetonitrile. Yield: 60 %. $^1$H-NMR (300 MHz, $CD_2Cl_2$): δ 158.9 (br), δ 158.9 (br), δ 122.2 (br), δ 78.5 (br), δ 73.8 (br), δ 45.3 (br), δ 16.2 (s), δ 11.8 (s), δ 78.5 (br), δ 9.6 (br), δ 6.4 (s), δ 5.3 (s), δ 2.0 (s), δ -2.3 (s). $^{19}$F-NMR (282 MHz, $CD_2Cl_2$): -78.9 (s). UV-Vis ($CH_2Cl_2$) [ε ($M^{-1}$ $cm^{-1}$)]: 247 nm ($9.7 \times 10^4$), 532 nm ($7.5 \times 10^3$). Anal. calcd. (%) for $C_{85}H_{59}F_3Fe_4N_{12}O_8S$: C 60.48, H 3.52, N 9.96; found: C 59.53, H 3.54, N 9.75.

**Synthesis of $[LFe_3(PhPz)_2(OArPz)OMn][OTf]_2$ (2.4-Mn).** In the glovebox, to a stirring solution of **2.1-Mn** (105.0 mg, 0.065 mmol) in $CH_2Cl_2$ (5 mL) was added PhIO (15.8 mg, 0.072 mmol), resulting in a darkening of solution to brown over one hour. After sixteen hours, solvent was removed under reduced pressure to yield a brown solid. The solid was triturated in benzene (2 mL) and filtered over a glass frit.

The remaining brown solid was dissolved in $CH_2Cl_2$, filtered, and dried under reduced pressure to yield **2.4-Mn** (78.1 mg, 70 %). X-ray quality crystals of **2.4-Mn** were obtained by diffusing diethyl ether into a concentration solution of **2.4-Mn** in acetonitrile. $^1$H-NMR (300 MHz, $CD_2Cl_2$): δ 162.6 (br), δ 159.9 (br), δ 157.0 (br), δ 120.4 (br), δ 110.4 (br), δ 105.7 (br), δ 93.4 (s), δ 91.7 (s), δ 86.6 (s), δ 85.2 (s), δ 81.4 (s), δ 73.5 (s), δ 71.3 (s), δ 69.5 (s), δ 67.5 (s), δ 58.3 (br), δ 58.0 (br), δ 57.1 (s), δ 17.4 (s), δ 17.0 (s), δ 15.2 (s), δ 14.5 (s), δ 13.5 (s), δ 12.6 (br), δ 10.8 (s), δ 10.6 (s), δ -0.7 (s), δ -1.1 (s), δ -2.0 (s). $^{19}$F-NMR (282 MHz, $CD_2Cl_2$): -78.9 (s). Anal. calcd. (%) for $C_{86}H_{59}F_6Fe_4N_{12}O_{11}S_2$: C 56.23, H 3.24, N 9.12; found: C 55.69, H 3.36, N 9.32.

**Synthesis of $[LFe_3(PhPz)_2(OArPz)OMn][OTf]_1$ (2.5-Mn).** In the glovebox, a solution of **2.1-Mn** (88.8 mg, 0.048 mmol) in $CH_2Cl_2$ (5 mL) was frozen in the cold well. To this thawing solution was added NaOArPzH (9.8 mg, 0.054 mmol) in $CH_2Cl_2$ (2 mL), accompanied by a color change to dark brown. After sixteen hours, solvent was removed under reduced pressure to yield a dark brown solid. The solid was triturated in benzene (2 mL) and filtered over a glass frit. The remaining brown solid was dissolved in $CH_2Cl_2$, filtered, and dried under reduced pressure to yield **2.5-Mn** (49.1 mg, 80 %). X-ray quality crystals of **2.5-Mn** were obtained by diffusing diethyl ether into a concentration solution of **2.5-Mn** in acetonitrile. $^1$H-NMR (300 MHz, $CD_2Cl_2$): δ 160.7 (br), δ 155.9 (br), δ 109.2 (br), δ 96.9 (br), δ 88.9 (s), δ 87.4 (s), δ 86.8 (s), δ 84.2 (s), δ 80.6 (br), δ 80.0 (br), δ 68.3 (br), δ 66.2 (s), δ 65.4 (s), δ 60.8 (s), δ 59.2 (s), δ 57.5 (s), δ 49.9 (s), δ 28.9 (s), δ 25.6 (s), δ 22.4 (s), δ 22.1 (s), δ 20.7 (s), δ 19.7 (s), δ 17.2 (s), δ 16.6 (s), δ 15.4 (s), δ 14.0 (s), δ 13.0 (s), δ 10.6 (s), δ -3.9 (s), δ -7.6 (br), δ -16.1 (br). $^{19}$F-NMR (282 MHz, $CD_2Cl_2$): δ -78.8 (s). Anal. calcd. (%) for $C_{85}H_{59}F_3Fe_4N_{12}O_8S$: C 60.48, H 3.52, N 9.96; found: C 59.53, H 3.54, N 9.75.

**Synthesis of $[LFe_3(PhPz)_2(OArPz)OMn][OTf]_3$ (2.6-Mn).**

***Procedure A.*** In the glovebox, to a thawing solution of **2.3-Mn** (74.5 mg, 0.038 mmol) in $CH_2Cl_2$ (5 mL) was added sPhIO (11.1 mg, 0.05 mmol), resulting in a darkening of solution to brown-purple over two hours. After sixteen hours, solvent was removed under reduced pressure to yield a brown-violet solid. The solid was triturated in benzene (3 mL) and filtered over a glass frit. The remaining brown-violet solid was dissolved in $CH_2Cl_2$, filtered, and dried under reduced pressure to yield **2.3-Mn** (60.0 mg, 80 %). $^1$H-NMR (300 MHz, $CD_2Cl_2$): δ 102.9 (br), δ 91.6 (br), δ 87.0 (br), δ 84.1 (br), δ 82.0 (br), δ 60.6 (br), δ 53.8 (br), δ 46.2 (br), δ 17.6 (s), δ 15.1 (s), δ 13.5 (s), δ 12.5 (s), δ -3.2 (s), δ -6.6 (s), δ -9.5 (s), δ -18.9 (s). $^{19}$F-NMR (282 MHz, $CD_2Cl_2$): δ -78.8 (s).

***Procedure B.*** In the glovebox, to a stirring solution of **2.4-Mn** (78.0 mg, 0.043 mmol) in $CH_2Cl_2$ (3 mL) was added AgOTf (11.5 mg, 0.045 mmol) as a suspension in $CH_2Cl_2$ (2 mL). The reaction was stirred for two hours and accompanied by color change from dark-brown to violet-brown. After two hours, the mixture was filtered over a glass frit. The filtrate was dried under reduced pressure to yield **2.4-Mn** (55.1 mg, 65 %). The $^1$H-NMR spectrum and $^{19}$F-spectrum are near-identical to that from *Procedure A*. X-ray quality crystals were obtained by diffusing diethyl ether into a concentrated solution of **2.6-Mn** in acetonitrile.

**Synthesis of $[LFe_3(PhPz)_3OMn(^sPhIO)][OTf]_3$ (2.7-Mn)**. In the glovebox, **2.3-Mn** (15.0 mg, 7.6 μmol) was dissolved in $CD_2Cl_2$ (0.50 mL) and frozen in the cold well. To this thawing solution was added sPhIO (2.8 mg, 8.4 μmol) in $CD_2Cl_2$ (0.50 mL). No discernable color change was observed. The $^1$H-NMR spectrum shows a new paramagnetic $^1$H-NMR spectrum. After five hours at room temperature, the $^1$H-NMR spectrum is identical to that of **2.6-Mn**. Single crystals were obtained by layering **2.3-Mn** in $CH_2Cl_2$ (0.45 mL), sPhIO in $CH_2Cl_2$ (0.55 mL), and toluene (1 mL) at -35 ºC and allowing the layers to mix over two weeks. $^1$H-NMR (300 MHz, $CD_2Cl_2$): δ 154.0 (br), δ 121.1 (br), δ 76.1 (br), δ 70.0 (br), δ 67.7 (br), δ 43.0 (br), δ 15.8 (s), δ 11.7 (s), δ -3.2 (s). $^{19}$F-NMR (282 MHz, $CD_2Cl_2$): δ -78.8 (s). Due to the thermal instability of **2.7-Mn**, elemental analysis could not be satisfactorily conducted.

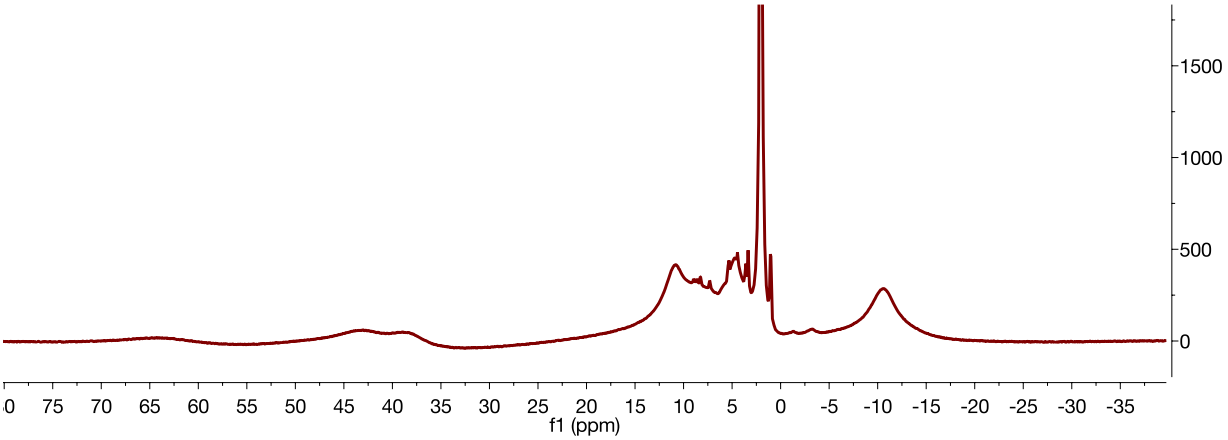


**Figure S1**. $^{1}$H-NMR (300 MHz, $CD_3CN$) spectrum of **1.1**.

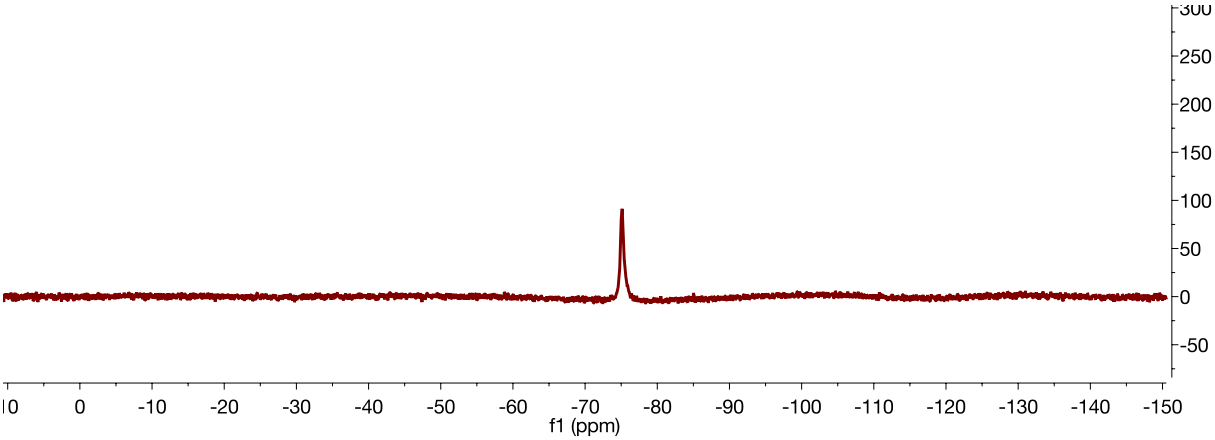


**Figure S2**. $^{19}$F-NMR (282 MHz, $CD_3CN$) spectrum of **1.1**.

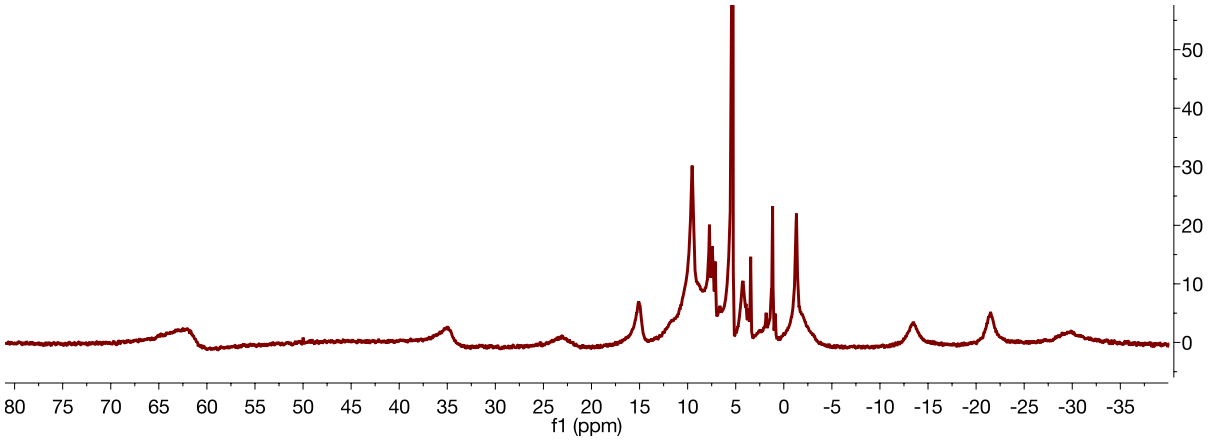


**Figure S3**. $^{1}$H-NMR (300 MHz, $CD_2Cl_2$) spectrum of proposed [$LMn_3(PhPz)_3ONa$][OTf].

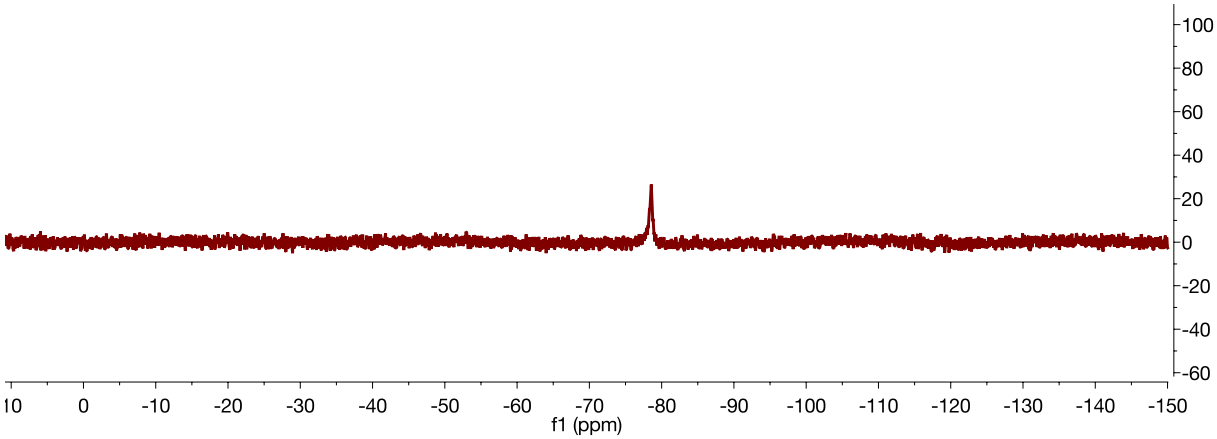


**Figure S4**. $^{19}$F-NMR (282 MHz, $CD_2Cl_2$) spectrum of proposed [$LMn_3(PhPz)_3ONa$][OTf].

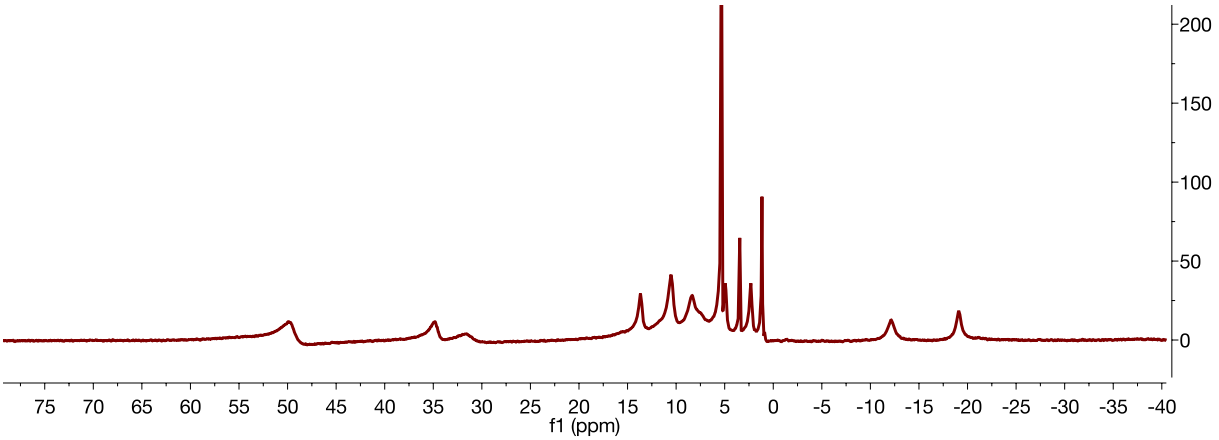


**Figure S5**. $^{1}$H-NMR (300 MHz, $CD_2Cl_2$) spectrum of **1.2**.

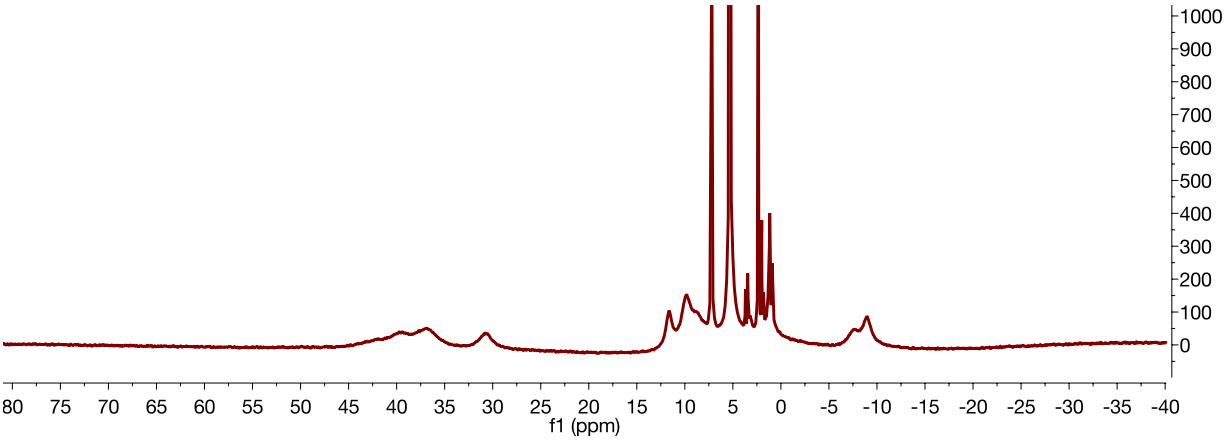


**Figure S6**. $^{1}$H-NMR (300 MHz, $CD_2Cl_2$) spectrum of **1.3**.

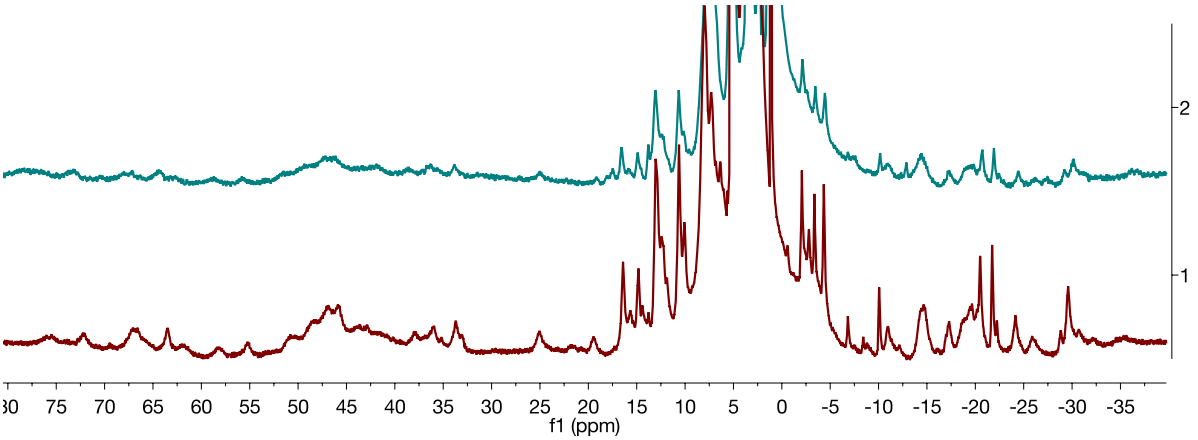


**Figure S7**. $^{1}$H-NMR (300 MHz, $CD_2Cl_2$) spectrum of **1.5** from *Procedure A* (top, cyan) and *Procedure B* (bottom, maroon).

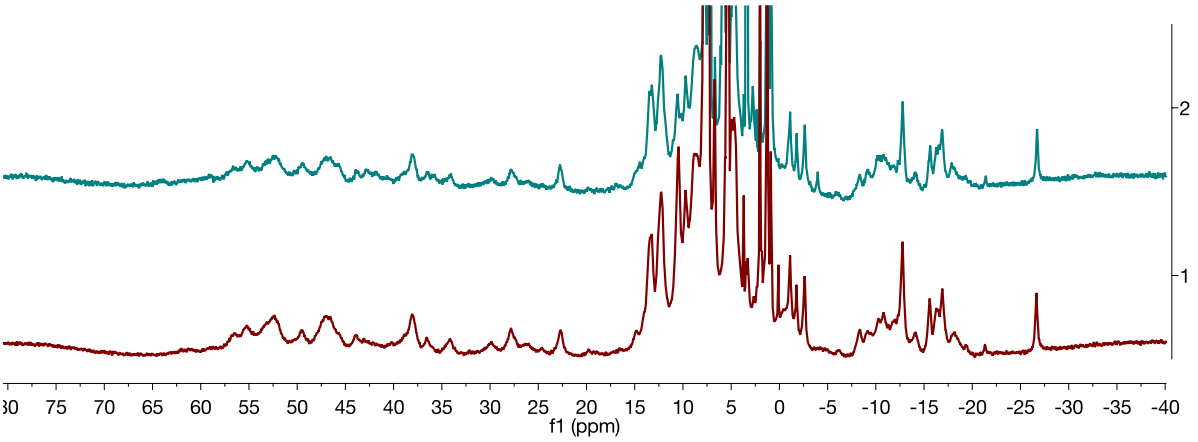


**Figure S8**. $^{1}$H-NMR (300 MHz, $CD_2Cl_2$) spectrum of **1.6** from *Procedure A* (top, cyan) and *Procedure B* (bottom, maroon).

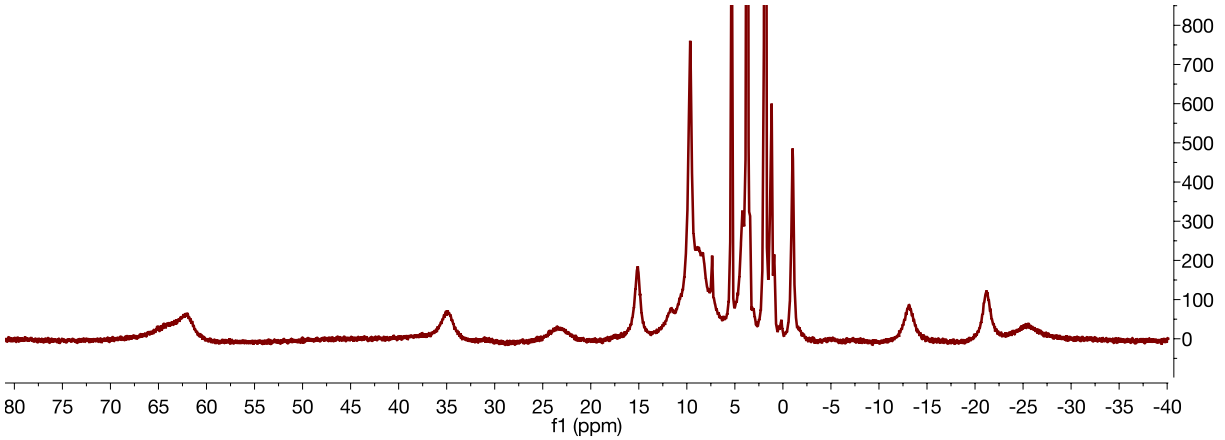


**Figure S9**. $^{1}$H-NMR (300 MHz, $CD_2Cl_2$) spectrum of proposed [$LMn_3(F_2ArPz)_3ONa$][OTf].

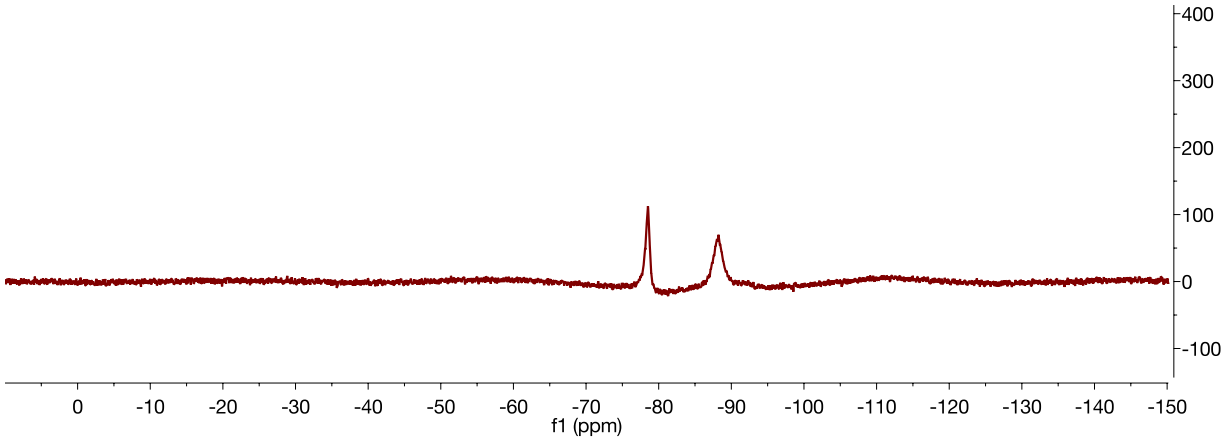


**Figure S10**. $^{19}$F-NMR (282 MHz, $CD_2Cl_2$) spectrum of proposed [$LMn_3(F_2ArPz)_3ONa$][OTf].

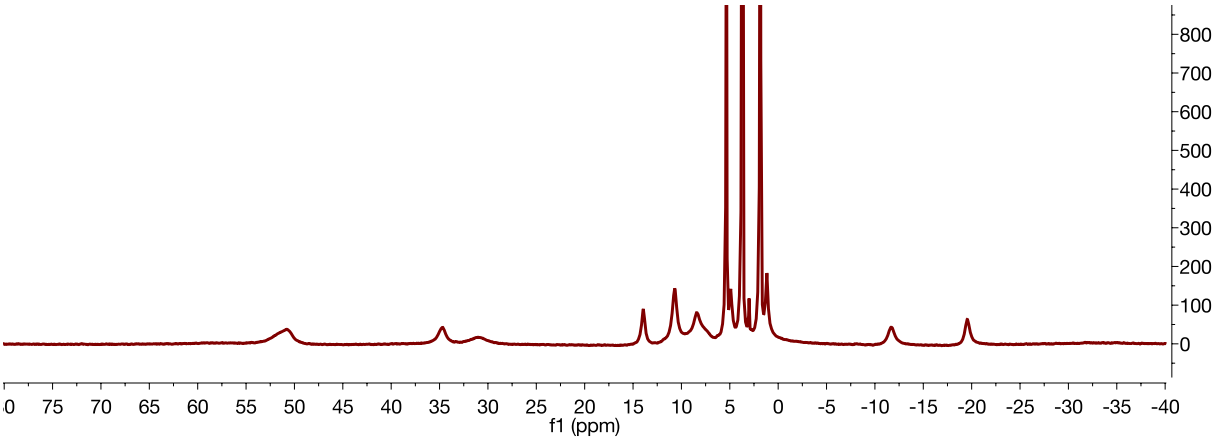


**Figure S11**. $^{1}$H-NMR (300 MHz, $CD_2Cl_2$) spectrum of **1.7**.

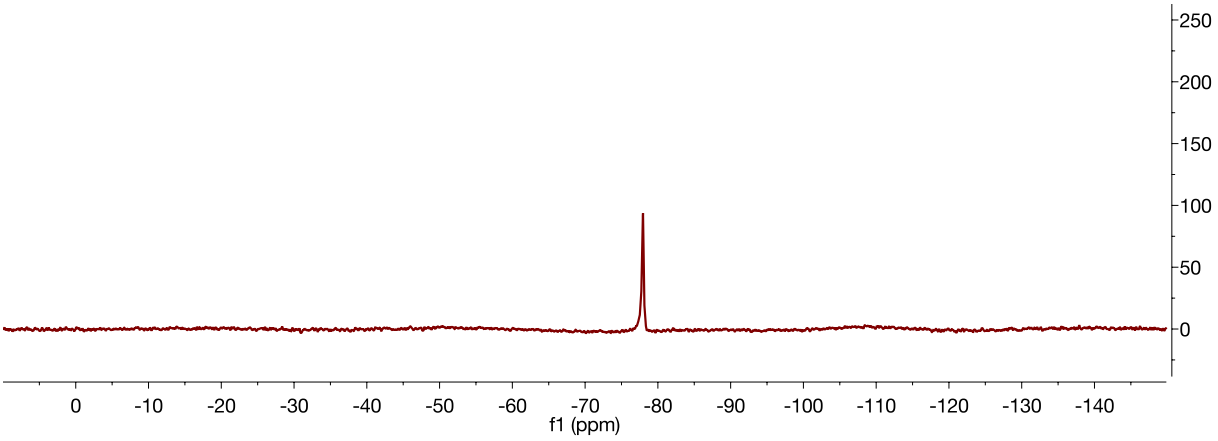


**Figure S12**. $^{19}$F-NMR (282 MHz, $CD_2Cl_2$) spectrum of **1.7**.

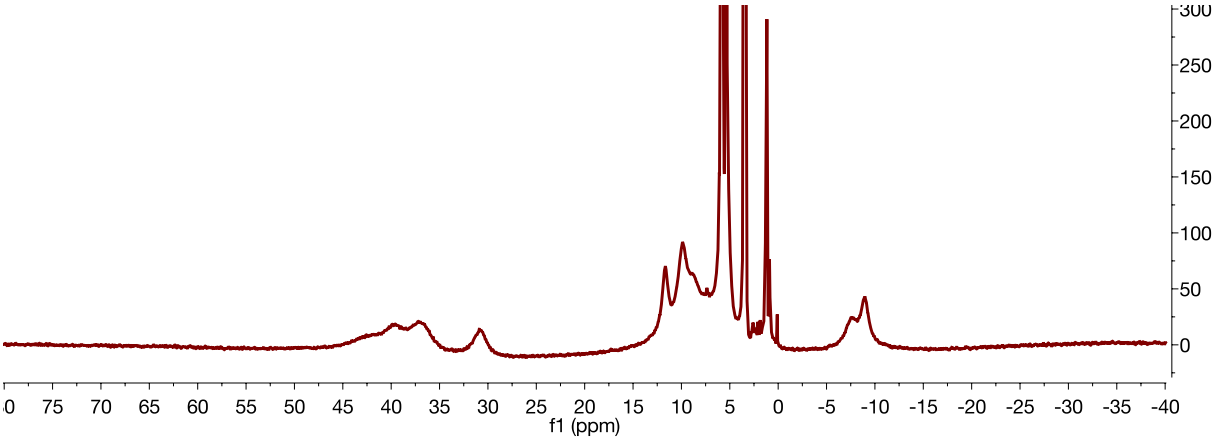


**Figure S13**. $^{1}$H-NMR (300 MHz, $CD_2Cl_2$) spectrum of **1.8**.

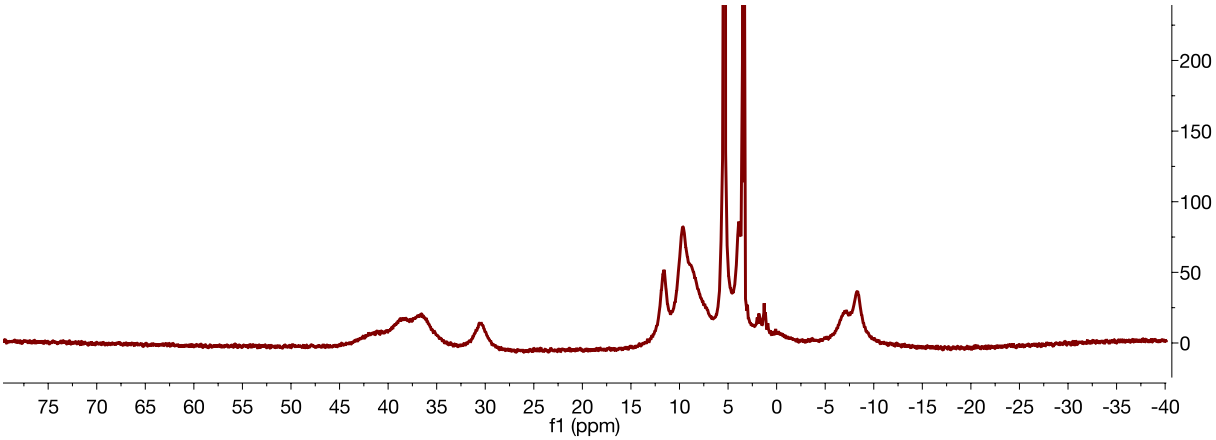


**Figure S14**. $^{1}$H-NMR (300 MHz, $CD_2Cl_2$) spectrum of proposed $[LMn_3(F_2ArPz)_3OMn][BF_4]$.

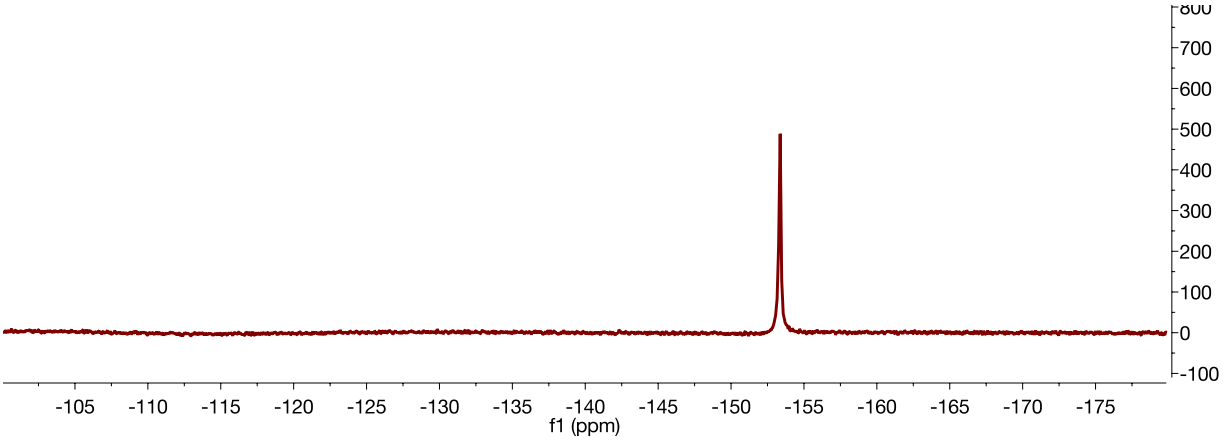


**Figure S15**. $^{19}$F-NMR (282 MHz, $CD_2Cl_2$) spectrum of proposed $[LMn_3(F_2ArPz)_3OMn][BF_4]$.

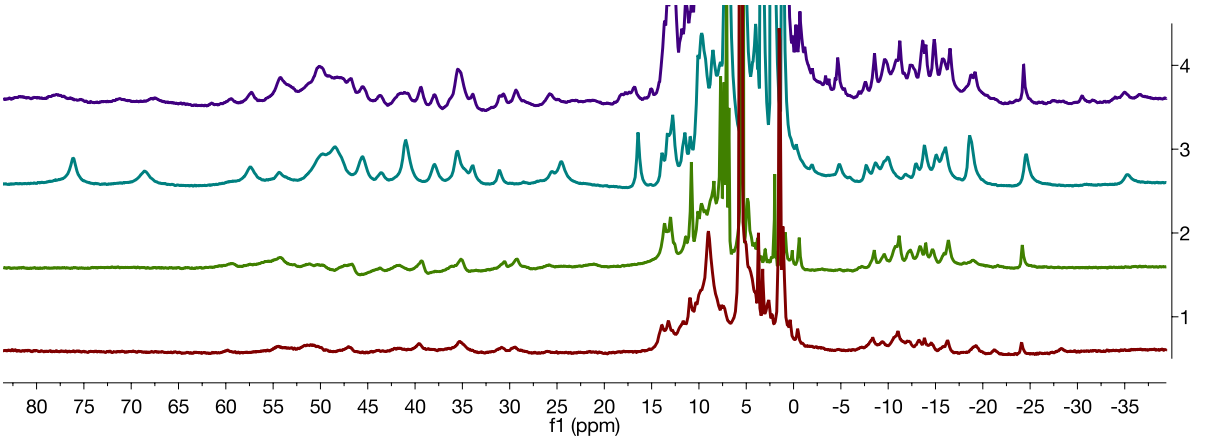


**Figure S16**. $^{1}$H-NMR (300 MHz, $CD_2Cl_2$) spectrum of **1.10** from *Procedure A* (bottom quartile, red), **1.10'** (lower-middle quartile, green), **1.11** (upper-middle quartile, cyan), and **1.10** *from Procedure B* (top quartile, purple).

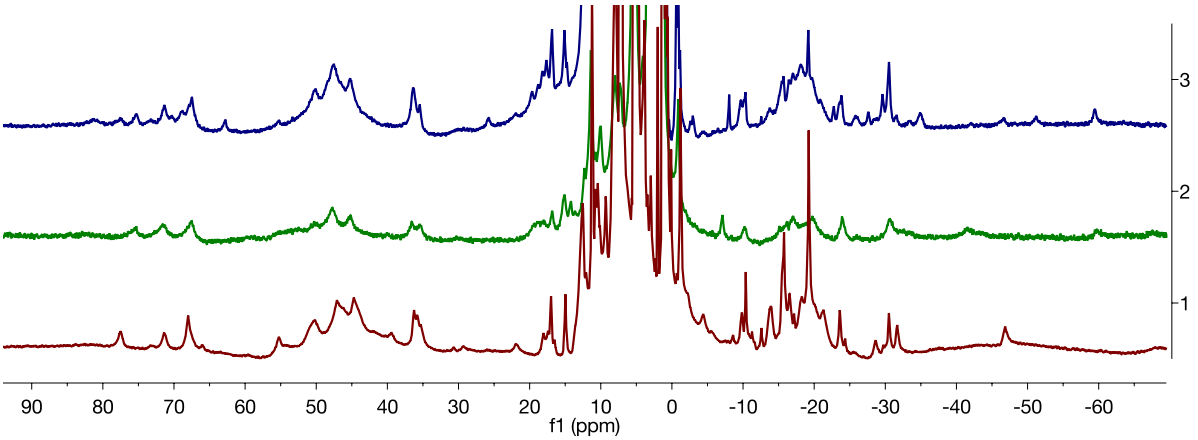


**Figure S17**. $^{1}$H-NMR (300 MHz, $CD_2Cl_2$) spectrum of **1.12** from *Procedure B* (bottom, red), **1.13** (middle, green), and **1.12** from *Procedure A* (top, blue).

**Chapter 2.**

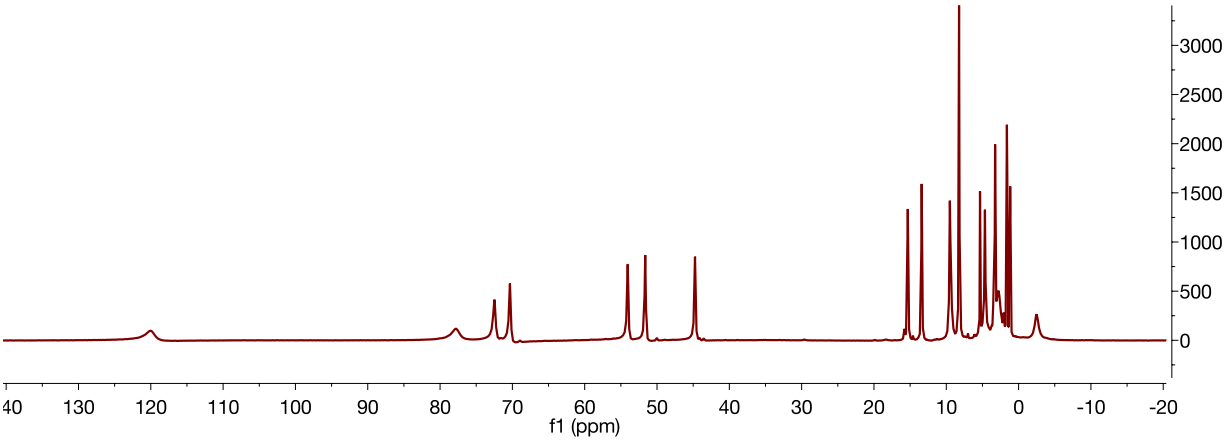


**Figure S18**. $^{1}$H-NMR (300 MHz, $CD_2Cl_2$) spectrum of **2.1-Mn**.

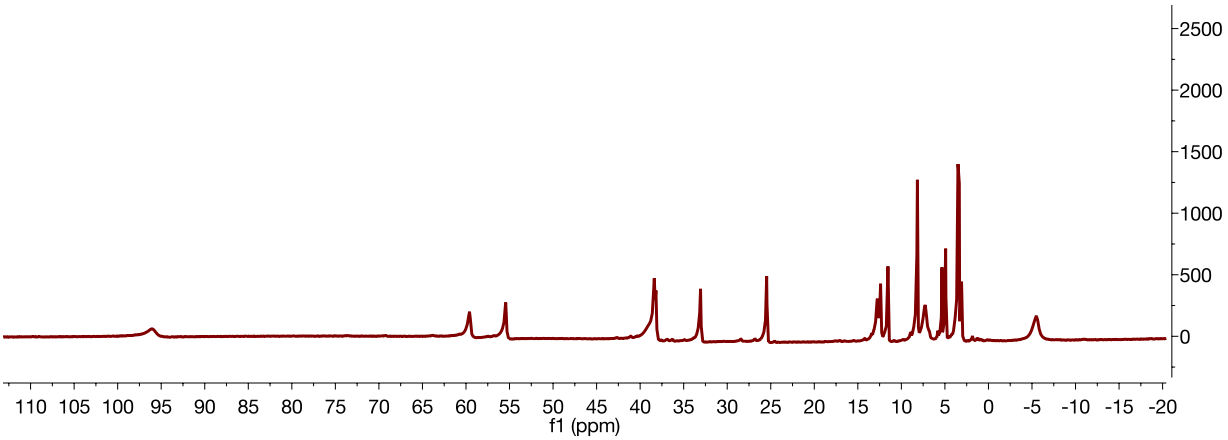


**Figure S19**. $^{1}$H-NMR (300 MHz, $CD_2Cl_2$) spectrum of **2.2-Mn**.

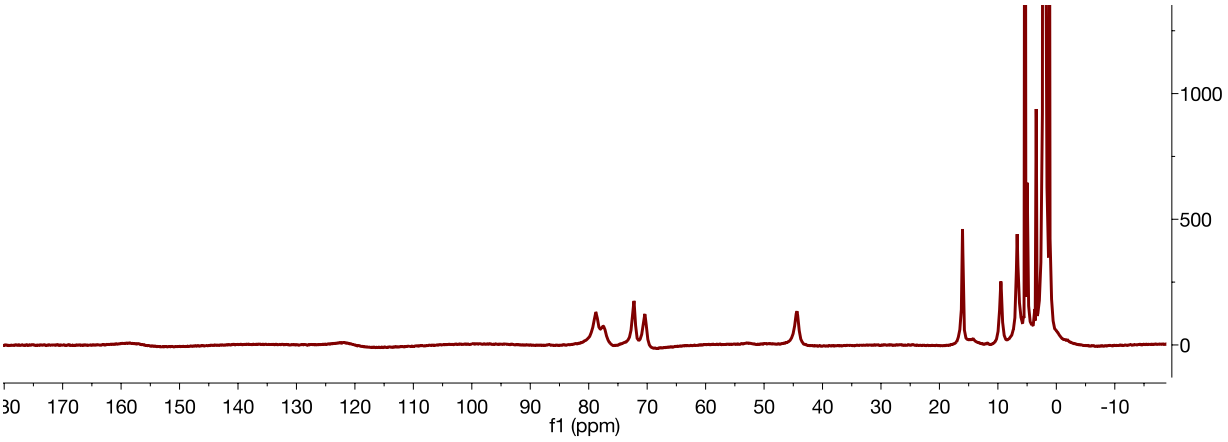


**Figure S20**. $^{1}$H-NMR (300 MHz, $CD_2Cl_2$) spectrum of **2.3-Mn**.

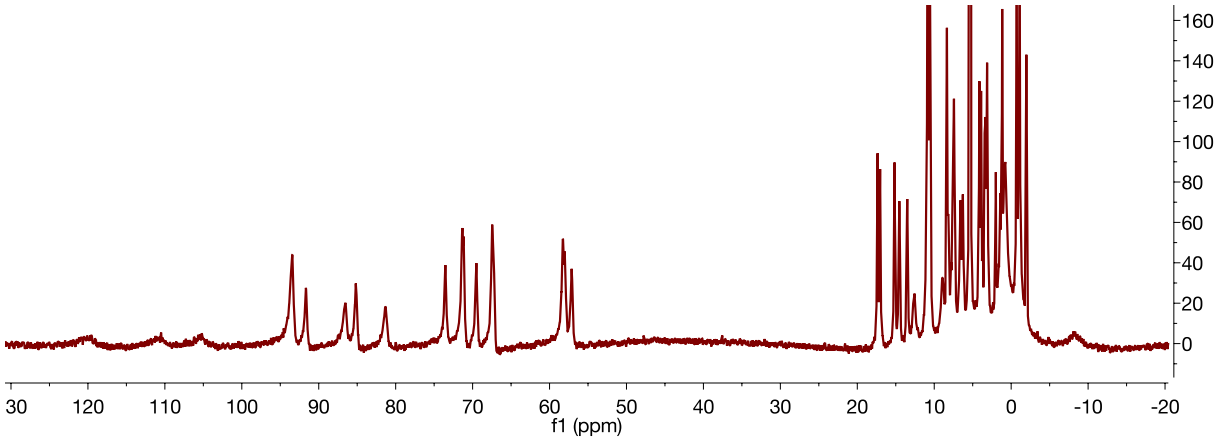


**Figure S21**. $^{1}$H-NMR (300 MHz, $CD_2Cl_2$) spectrum of **2.4-Mn**.

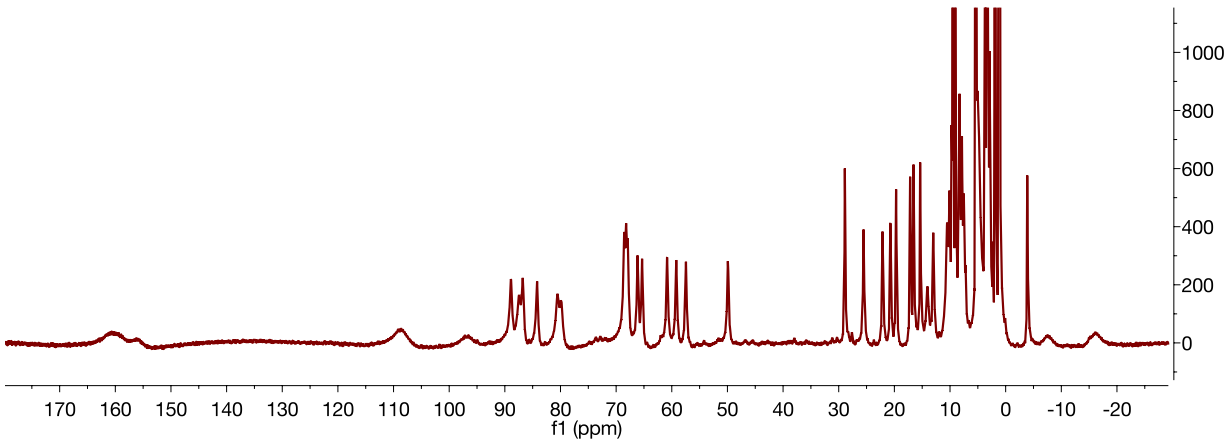


**Figure S22**. $^{1}$H-NMR (300 MHz, $CD_2Cl_2$) spectrum of **2.5-Mn**.

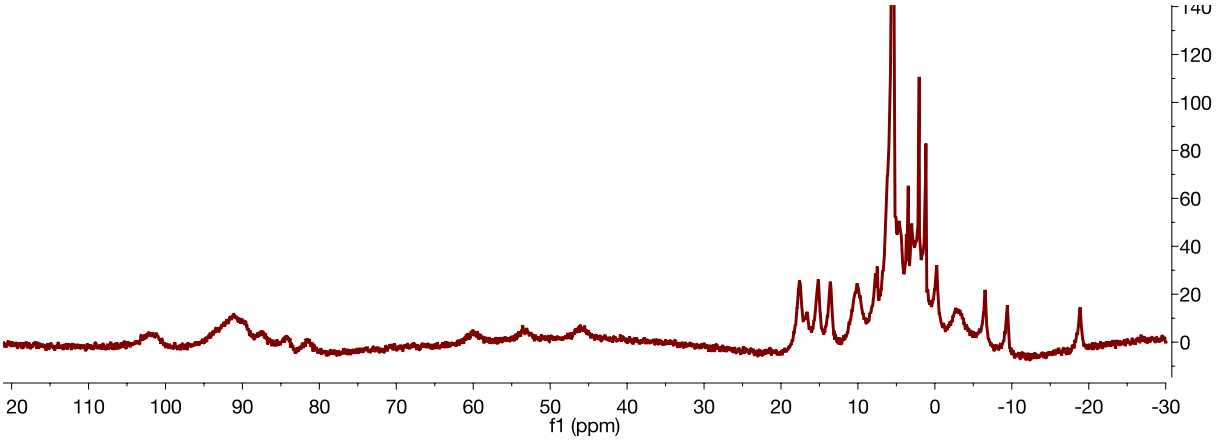


**Figure S23**. $^{1}$H-NMR (300 MHz, $CD_2Cl_2$) spectrum of **2.6-Mn**.

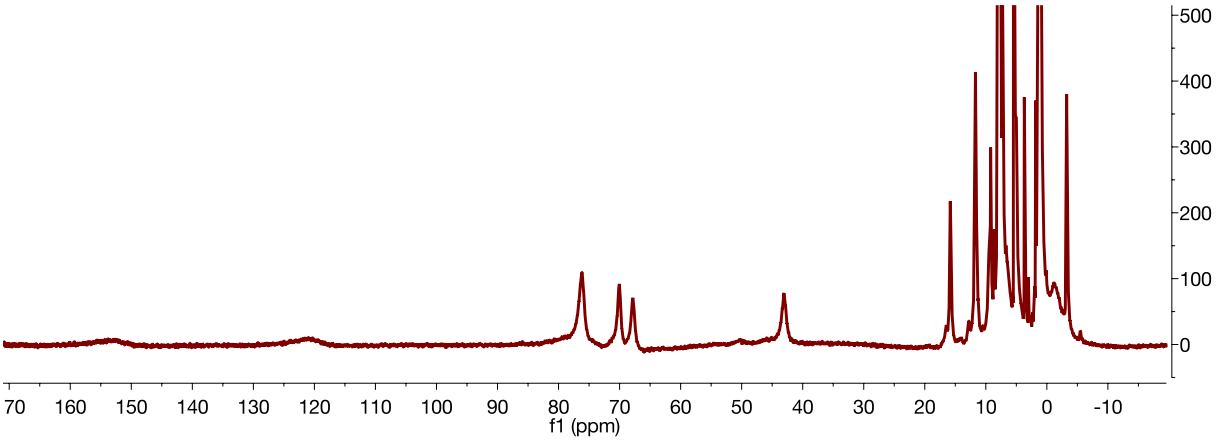


**Figure S24**. $^{1}$H-NMR (300 MHz, $CD_2Cl_2$) spectrum of **2.7-Mn**.

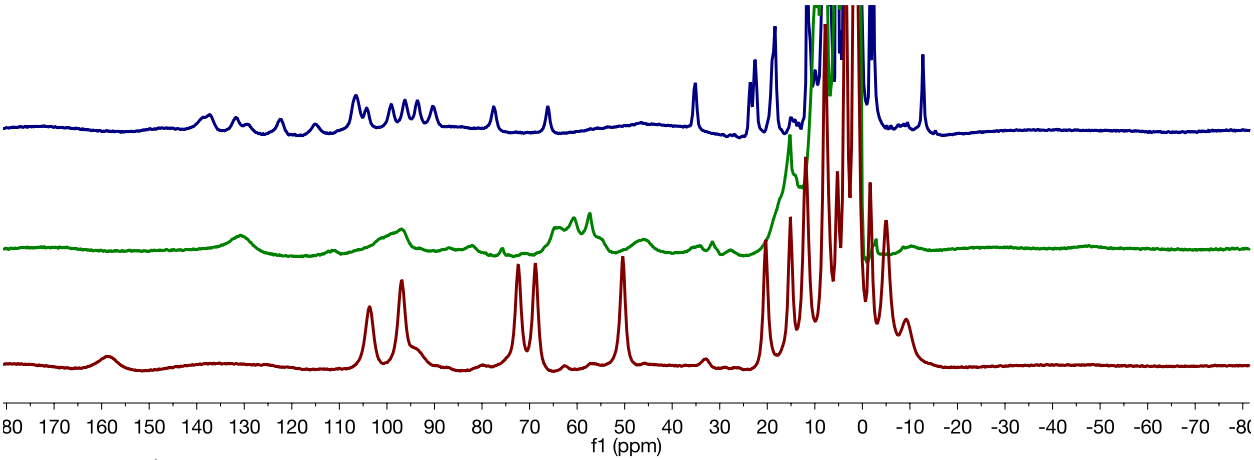


**Figure S25**. $^{1}$H-NMR (500 MHz, $CD_2Cl_2$, -70 ºC) spectrum of **2.1-Mn** (red, bottom), intermediate species, **2.8-Mn** (green, middle), **2.4-Mn** (top, blue).

## REFERENCES


(1) Brudvig, G. W. *Phil. Trans. R. Soc. B* **2008**, *363*, 1211.
(2) Cox, N.; Pantazis, D. A.; Neese, F.; Lubitz, W. *Acc. Chem. Res.* **2013**, *46*, 1588.
(3) Lewis, N. S.; Nocera, D. G. *Proc. Nat. Acad. Sci. USA*. **2006**, *103*, 15729.
(4) Gray, H. B. *Nat. Chem.* **2009**, *1*, 1.
(5) Pantazis, D. A.; Ames, W.; Cox, N.; Lubitz, W.; Neese, F. *Angew. Chem. Int. Ed.* **2012**, *51*, 9935.
(6) Powers, T. M.; Betley, T. A. *J. Am. Chem. Soc.* **2013**, *135*, 12289.
(7) Umena, Y.; Kawakami, K.; Shen, J.-R.; Kamiya, N. *Nature* **2011**, *473*, 55.
(8) Suga, M.; Akita, F.; Hirata, K.; Ueno, G.; Murakami, H.; Nakajima, Y.; Shimizu, T.; Yamashita, K.; Yamamoto, M.; Ago, H.; Shen, J.-R. *Nature* **2015**, *517*, 99.
(9) Taguchi, T.; Gupta, R.; Lassalle-Kaiser, B.; Boyce, D. W.; Yachandra, V. K.; Tolman, W. B.; Yano, J.; Hendrich, M. P.; Borovik, A. S. *J. Am. Chem. Soc.* **2012**, *134*, 1996.
(10) Betley, T. A.; Wu, Q.; Van Voorhis, T.; Nocera, D. G. *Inorg. Chem.* **2008**, *47*, 1849.
(11) Sproviero, E. M.; Gascón, J. A.; McEvoy, J. P.; Brudvig, G. W.; Batista, V. S. *J. Am. Chem. Soc.* **2008**, *130*, 3428.
(12) McEvoy, J. P.; Gascon, J. A.; Batista, V. S.; Brudvig, G. W. *Photochem. Photobiol. Sci.* **2005**, *4*, 940.
(13) Siegbahn, P. E. M. *Inorg. Chem.* **2008**, *47*, 1779.
(14) Siegbahn, P. E. M. *Acc. Chem. Res.* **2009**, *42*, 1871.
(15) Siegbahn, P. E. M. *BBA* **2013**, *1827*, 1003.
(16) Liu, F.; Concepcion, J. J.; Jurss, J. W.; Cardolaccia, T.; Templeton, J. L.; Meyer, T. J. *Inorg. Chem.* **2008**, *47*, 1727.
(17) Limburg, J.; Vrettos, J. S.; Liable-Sands, L. M.; Rheingold, A. L.; Crabtree, R. H.; Brudvig, G. W. *Science* **1999**, *283*, 1524.
(18) Codolà, Z.; Gómez, L.; Kleespies, S. T.; Que Jr, L.; Costas, M.; Lloret-Fillol, J. *Nat. Commun.* **2015**, *6*.
(19) Liao, R.-Z.; Kärkäs, M. D.; Lee, B.-L.; Åkermark, B.; Siegbahn, P. E. M. *Inorg. Chem.* **2014**, *54*, 342.
(20) Parsell, T. H.; Yang, M.-Y.; Borovik, A. S. *J. Am. Chem. Soc.* **2009**, *131*, 2762.
(21) Parsell, T. H.; Behan, R. K.; Green, M. T.; Hendrich, M. P.; Borovik, A. S. *J. Am. Chem. Soc.* **2006**, *128*, 8728.
(22) Borovik, A. *Chem. Soc. Rev.* **2011**, *40*, 1870.
(23) Gupta, R.; Taguchi, T.; Lassalle-Kaiser, B.; Bominaar, E. L.; Yano, J.; Hendrich, M. P.; Borovik, A. S. *Proc. Nat. Acad. Sci. USA*. **2015**, *112*, 5319.
(24) Park, Y. J.; Matson, E. M.; Nilges, M. J.; Fout, A. R. *Chem. Commun.* **2015**, *51*, 5310.
(25) De Ruiter, G.; Thompson, N. B.; Lionetti, D.; Agapie, T. *J. Am. Chem. Soc.* **2015**, *137*, 14094.
(26) Sahu, S.; Widger, L. R.; Quesne, M. G.; de Visser, S. P.; Matsumura, H.; Moënne-Loccoz, P.; Siegler, M. A.; Goldberg, D. P. *J. Am. Chem. Soc.* **2013**, *135*, 10590.
(27) de Ruiter, G.; Thompson, N. B.; Takase, M. K.; Agapie, T. *J. Am. Chem. Soc.* **2016**, *138*, 1486.
(28) Harman, W. H.; Chang, C. J. *J. Am. Chem. Soc.* **2007**, *129*, 15128.
(29) Bigi, J. P.; Harman, W. H.; Lassalle-Kaiser, B.; Robles, D. M.; Stich, T. A.; Yano, J.; Britt, R. D.; Chang, C. J. *J. Am. Chem. Soc.* **2012**, *134*, 1536.

(30) Bigi, J. P.; Harman, W. H.; Lassalle-Kaiser, B.; Robles, D. M.; Stich, T. A.; Yano, J.; Britt, R. D.; Chang, C. J. *J. Am. Chem. Soc.* **2012**, *134*, 1536.
(31) Leeladee, P.; Goldberg, D. P. *Inorg. Chem.* **2010**, *49*, 3083.
(32) Smegal, J. A.; Schardt, B. C.; Hill, C. L. *J. Am. Chem. Soc.* **1983**, *105*, 3510.
(33) Birchall, T.; Smegal, J. A.; Hill, C. L. *Inorg. Chem.* **1984**, *23*, 1910.
(34) Song, W. J.; Seo, M. S.; DeBeer George, S.; Ohta, T.; Song, R.; Kang, M.-J.; Tosha, T.; Kitagawa, T.; Solomon, E. I.; Nam, W. *J. Am. Chem. Soc.* **2007**, *129*, 1268.
(35) Yano, J.; Yachandra, V. *Chem. Rev.* **2014**, *114*, 4175.
(36) Collman, J. P.; Ghosh, S.; Dey, A.; Decréau, R. A.; Yang, Y. *J. Am. Chem. Soc.* **2009**, *131*, 5034.
(37) Rohde, J.-U.; In, J.-H.; Lim, M. H.; Brennessel, W. W.; Bukowski, M. R.; Stubna, A.; Münck, E.; Nam, W.; Que, L. *Science* **2003**, *299*, 1037.
(38) Gütlich, P.; Link, R.; Trautwein, A. *Mössbauer spectroscopy and transition metal chemistry*; Springer Science & Business Media, 2013; Vol. 3.
(39) Gouré, E.; Carboni, M.; Dubourdeaux, P.; Clémancey, M.; Balasubramanian, R.; Lebrun, C.; Bayle, P.-A.; Maldivi, P.; Blondin, G.; Latour, J.-M. *Inorg. Chem.* **2014**, *53*, 10060.
(40) Lalia-Kantouri, M.; Papadopoulos, C. D.; Hatzidimitriou, A. G.; Bakas, T.; Pachini, S. *Anorg. Allg. Chem.* **2010**, *636*, 531.
(41) Singh, A. K.; Jacob, W.; Boudalis, A. K.; Tuchagues, J. P.; Mukherjee, R. *Eur. J. Inorg. Chem.* **2008**, *2008*, 2820.
(42) Chardon-Noblat, S.; Horner, O.; Chabut, B.; Avenier, F.; Debaecker, N.; Jones, P.; Pécaut, J.; Dubois, L.; Jeandey, C.; Oddou, J.-L. *Inorg. Chem.* **2004**, *43*, 1638.
(43) Reynolds, R.; Coucouvanis, D. *Inorg. Chem.* **1998**, *37*, 170.
(44) Macikenas, D.; Skrzypczak-Jankun, E.; Protasiewicz, J. D. *Angew. Chem. Int. Ed.* **2000**, *39*, 2007.
(45) Wang, C.; Kurahashi, T.; Fujii, H. *Angew. Chem. Int. Ed.* **2012**, *51*, 7809.
(46) Wang, C.; Kurahashi, T.; Inomata, K.; Hada, M.; Fujii, H. *Inorg. Chem.* **2013**, *52*, 9557.
(47) Lennartson, A.; McKenzie, C. J. *Angew. Chem. Int. Ed.* **2012**, *51*, 6767.
(48) Turlington, C. R.; Morris, J.; White, P. S.; Brennessel, W. W.; Jones, W. D.; Brookhart, M.; Templeton, J. L. *Organometallics* **2014**, *33*, 4442.
(49) Becke, A. D. *Phys. Rev. A* **1988**, *38*, 3098.
(50) Becke, A. D. *J. Chem. Phys.* **1993**, *98*, 5648.
(51) Lee, C. T. Y., W. T.; Parr, R. G. *Phys. Rev. B* 1988, 37, 785.
(52) Shaik, S.; Hirao, H.; Kumar, D. *Acc. Chem. Rev.* **2007**, *40*, 532.
(53) Pangborn, A. B.; Giardello, M. A.; Grubbs, R. H.; Rosen, R. K.; Timmers, F. J. *Organometallics* **1996**, *15*, 1518.
(54) Saltzman, H.; Sharefkin, J. G. In *Organic Syntheses*; John Wiley & Sons, Inc.: 2003.
(55) Song, F.; Wang, C.; Falkowski, J. M.; Ma, L.; Lin, W. *J. Am. Chem. Soc.* **2010**, *132*, 15390.
(56) Bürger, H.; Wannagat, U. *Monatsh Chem*, *95*, 1099.
(57) Riedel, P. J.; Arulsamy, N.; Mehn, M. P. *Inorg. Chem. Commun.* **2011**, *14*, 734.
(58) Macikenas, D.; Skrzypczak-Jankun, E.; Protasiewicz, J. D. *J. Am. Chem. Soc.* **1999**, *121*, 7164.
(59) Hupp, T.; Nguyen, S. *Chem. Eng. News* **2011**, *89*, 2.
(60) APEX-II *Version 2 User Manual, M86-E01078, Bruker Analytical X-ray Systems,* Madison, WI, June 2006.

(61) Sheldrick, G. M. *"SADABS (version 2008/1): Program for Absorption Correction for Data from Area Detector Frames",* University of Göttingen, 2008.
(62) Sheldrick, G. M. *Acta Crystallogr., Sect. A: Found. Crystallogr.* **2008**, *64*, 112.

## ABOUT THE AUTHOR

Kurtis Mickel Carsch was born in Bellevue, WA, on April 26, 1994. Kurtis is the son of Leslie Mickel and Randy Carsch. Kurtis' enthusiasm for research originated from his two-year, early-college experience, when he was 16 years of age at the University of North Texas. Under mentorship of Professor Thomas Cundari, he explored the transformation of natural gas into commodity chemicals by metal-containing catalysts through a joint synthesis-computational endeavor. Kurtis thereafter attended Caltech and continued his research at the interface of experimental and theoretical chemistry with Professor William A. Goddard and Professor Theodor Agapie. Kurtis' accomplishments include: publications in impactful science journals, numerous awards and recognitions, meeting the president of the United States through the Intel Science Talent Search, and the respect and encouragement he has garnered to formulate and pursue varied research projects. Starting July 2016, Kurtis will pursue a Ph.D. in inorganic chemistry at Harvard University and will begin his first rotation under tutelage of Professor Ted Betley. Kurtis is an NSF Fellow and a Hertz Fellow. Outside of research, Kurtis enjoys hiking mountains, eating extremely spicy foods, exploring Los Angeles, and working out.